NTNU
Norwegian University of
Science and Technology

Estimation of Water Velocity and Tidal Changes Between 4D Seismic Vintages

Ole Martin Teien

Petroleum Geoscience and Engineering
Submission date: June 2017
Supervisor: Martin Landrø, IGP
Co-supervisor: Harald Westerdahl, Statoil ASA

Norwegian University of Science and Technology
Department of Geoscience and Petroleum

Preface

This report is the result of TPG4925 - Petroleum Geosciences, Master's Thesis at NTNU, a part of the study program Petroleum Engineering and Geosciences - Petroleum Geophysics. The Master's Thesis was carried out the spring semester 2017.

The idea of this Master's Thesis was brought up by Statoil as an attempt to reduce the 4D seismic differences caused by water column changes. Statoil has provided with 4D seismic data from the Snorre field, along with synthetic data used in this project. The work presented in this report is performed by the author Ole Martin Teien. It is the author's views and conclusions that are presented in this report, not the views of Statoil or the Snorre License.

Some of the sections in this report are copied or slightly modified from the Specialization Project in Teien (2016), written the autumn semester 2016. The relevant sections are indicated at the beginning of each chapter.

The readers of this report are assumed to have basic knowledge within geophysics.

Trondheim, 2017-06-26

Ole Martin Teien

Ole Martin Teien

Acknowledgments

I would like to thank all the persons that have been to great help and good support for me during my work with this project.

First of all I would like to thank my two supervisor's, Professor Martin Landrø at NTNU and Lead Researcher Geophysics Harald Westerdahl at Statoil. They have both contributed with great academic advice and helpful guidance during this Master's Thesis project.

I would also like to thank Marit Stustad Guttormsen, Manager Geophysics Seismic Processing, together with the rest of the Seismic Imaging and Processing team in Oslo for great help and support, and a warm welcome to the SIP team.

A great thanks also to Principal Geophysicist Nigel Moyle at Statoil for good support and technical discussions, along with the Snorre License for access to the Snorre data.

O.M.T.

Summary

Between the acquisitions of the vintages used in 4D seismic, both the seismic water velocity and the tidal level can change. These changes will create time shifts that reduce the 4D seismic's sensitivity to real changes in the reservoir and need to be corrected for in order to obtain optimal visualization of the production-related reservoir changes. In order to achieve good corrections, it is necessary to have precise estimates of the water column changes. Therefore, the goal of this Master's Thesis was to develop a method to precisely estimate the water velocity and tidal changes between the 4D seismic vintages. This goal has been fulfilled and the method developed is called "Time Shift Curve Inversion" (TSCI). The TSCI method utilizes inversion based on time shift curves showing water column induced time shift variation with offset. The time shift curves are found by a trace-by-trace cross-correlation of two seismic vintages. The forward modelling in the inversion was based on a 1D raytracing model and the output of the TSCI method was the differences in water velocity, tidal level and the start of data delay between the vintages.

The TSCI method was tested on synthetic data and the results gave precise estimates of the water column changes for both realistic seismic and realistic subsurface models. In addition, the TSCI method proved to be robust to errors in the assumed water depth and base velocity in the background model used for forward modelling.

For the use of this project, Statoil provided with seismic data from two 4D vintages from the Snorre field. The TSCI method was applied to the data and resulted in consistent results and good match with other estimates of the water column changes.

To obtain best possible results with the TSCI method, the input seismic data need to be of good quality. The events included in the calculation need to have higher amplitudes than the surrounding signal, and the arrival times of the events need to be predicted precisely. In addition, differences in source positions between the vintages need to be corrected for.

There are parts of the TSCI method that can be developed further. Especially, the way the arrival time prediction is performed. The 1D raytracing model used in this project should be exchanged by a model that accounts for the variations along the sea floor. This is expected to increase the precision of the estimated water column changes.

Sammendrag

Både den seismiske vannhastigheten og tidevannsnivået kan endre seg mellom ulike 4D seismiske årganger. Disse endringene vil skape tidsskift som reduserer 4D seismikkens sensitivitet for faktiske endringer i reservoaret, og må korrigeres for hvis god visualisering av reservoarendringene skal oppnås. For gode korreksjoner er det nødvendig å ha presise estimater av endringene i vannhastighet og tidevannsnivå mellom årgangene. Målet med denne masteroppgaven har derfor vært å utvikle en metode for å estimere vannhastighet og tidevannsendringer mellom 4D seismiske årganger. Dette målet er oppnådd, og metoden som er utviklet er kalt for ”Time Shift Curve Inversion” (TSCI). Metoden benytter seg av inversjon basert på tidsskiftkurver som viser de vannkolonneinduserte tidsskiftenes variasjon med offset. Tidsskiftkurvene er funnet ved å krysskorrelere trase for trase i 2 seismiske årganger. Forovermodelleringen benyttet i inversjonen var basert på en 1D raytracing-modell og resultatene fra TSCI metoden er estimater på endringene i vannhastighet, tidevannsnivå og ”start of data delay” mellom årgangene.

TSCI metoden ble testet på syntetiske data og resultatene ga presise estimater på vannkolonneendrignene for både realistisk seismikk og realistiske undergrunnsmodeller. TSCI metoden viste seg også å være robust for feil i antatt vanndyp og vannhastighet i bakgrunnsmodellen brukt for forovermodellering.

Statoil stilte data fra 2 seismiske 4D-årganger fra Snorre-feltet til disposisjon for denne oppgaven. Både endring i vannhastighet og tidevannsnivå ble estimert presist og konsistent ved å benytte TSCI metoden på Snorre-dataene.

For å oppnå best mulig resultater med TSCI metoden er det en forutsetning å ha god kvalitet på input dataene. Eventene som inkluderes i metoden må ha høyere amplitude enn det omkringliggende signalet og ankomsttidene for de ulike eventene må bli predikert presist. I tillegg må det korrigeres for forskjeller i kildeposisjon mellom årgangene.

Det er deler av TSCI metoden som kan bli utviklet videre. Spesielt gjelder dette måten ankomsttidene er predikert på. Raytracing-modellen (1D) som ble brukt i dette prosjektet bør bli erstattet med en modell som tar hensyn til variasjoner langs havbunnen. Dette forventes å øke presisjonen på estimatene av endringene i vannhastighet og tidevannsnivå.

Contents

Chapter 1

Introduction

This chapter is modified from the Specialization Project in Teien (2016).

The different vintages used in 4D seismic are often acquired at quite different water column properties. Due to currents, tides and seasonal changes, both the water velocity and the water level can change between the 4D vintages Lacombe et al. (2006).

The tidal changes are caused by gravitational forces exerted by the Sun and the Moon. Ebb and flow happen about twice a day. In Norway, the largest contribution is from the Moon, and the period between two ebbs equals half a Moon day (12 hours and 25 minutes) Kartverket (2016). Along the western coast of Norway, the tidal differences are usually below 2 meters Kartverket (2016).

The P-wave water velocity is affected by different factors. The velocity is most sensitive to the changes in temperature MacKay et al. (2003), but the salinity and the water depth do also affect the water velocity. The water velocity increases with increased temperature, increased salinity and increased depth. Throughout a year with different seasons, the upper parts of the water layer will have largest variations in temperature due to variations in the Sun heat and wind. The deeper parts of the water layer have less temperature variations since these parts are less exposed to the seasonal changes Åsli (2002). Because of this, water velocity changes are largest in the upper parts of the water column.

The Problem with Changes in Water Velocity and Tides

The change in water velocity and tidal level between the 4D seismic vintages results in differences in traveltime through the water layer and time shifts between the vintages Wang et al. (2012), MacKay et al. (2003). 4D seismic is used to identify changes in the subsurface over time. One example is when gas is injected into the reservoir and replaces water. This induces a velocity change and a time shift between the vintages before and after the gas injection. However, the time shifts caused by changes in the reservoir are often small and might have lower magnitudes than the time shifts caused by water column changes. As a consequence, the water column induced time shifts will reduce the 4D seismic's sensitivity to real 4D changes in the reservoir.

For a given water depth, the time shifts created by water velocity changes are larger for shallow reservoirs than for deep reservoirs, as the magnitude of these time shifts is proportional to the ray path length in the water column Bertrand and MacBeth (2003). The time shifts created by tidal changes will be largest for deeper reservoirs as the tidal change is a vertical change and most pronounced for ray paths closer to the vertical. Regardless the depth of the reservoir, the water column induced time shifts will affect the time shifts created by the actual reservoir changes in some degree and need to be corrected for in order to obtain optimal visualization of the production-related changes in the reservoir.

Correction for Water Column Induced Time Shifts

There exist several methods for correction of the water column induced time shifts. Today, the variations in the tidal level are often predicted with the use of tide tables. However, the accuracy of these tide tables has been questioned as the tide predictions often are defined far from the acquisition area Lacombe et al. (2006). Henry et al. (2004) presents a methodology using GPS data for measuring tidal level changes, which obtained an accuracy of a few tens of centimeters. If the changes in tidal level are known, the tidal changes can be corrected for by performing simple time shifts to NMO corrected data Lacombe et al. (2006).

Several methods have been proposed to correct for the variations in the water velocity Xu and Pham (2003), Fried and MacKay (2001). Lacombe et al. (2006) presents a method which re-aligns the primaries in the 4D vintages to a common datum. This was done by changing the measured RMS velocities in the 4D vintages to a common reference velocity, described further in Appendix B.1.

The corrections mentioned above will only align the primaries in the different vintages MacKay et al. (2003). The water layer multiples have travelled through the water layer several times and been exposed to the changes in the water layer in varying degree. Hence, the primaries and the water layer multiples can not be time-aligned by the same time shift correction Hatchell et al. (2008). To remove the multiples, other multiple removal methods have to be used, but the multiples are newer completely removed. The influence of the residual multiples remaining in the data results in residual time shifts that increase with traveltime. This increases the non-repeatability issue Wang et al. (2012). Hence, there are improvement areas in the time shift corrections, especially for the corrections of the water layer multiples.

Regardless the correction method used, in order to obtain best possible corrections for the time shifts caused by water column changes, it is important to have precise estimates of the actual changes in water velocity and tidal level between the 4D seismic vintages MacKay et al. (2003). This leads to the goal of this Master's Thesis.

Goal of the Master's Thesis

The goal of this Master's Thesis was to develop a method to precisely estimate the water velocity and tidal changes between 4D seismic vintages, from the seismic data alone.

To obtain this goal, Statoil provided with 4D seismic data from the Snorre field. The Snorre data was used to develop a method based on inversion of water column induced time shifts. In addition, different tests were performed on synthetic seismic data to understand the method's advantages and limitations.

Chapter 2

Background Theory

In this Chapter, Section 2.3 is copied, while Section 2.1 and 2.4 are slightly modified from the Specialization Project in Teien (2016).

2.1 Time Shift Expression

When the water velocity and the tidal level changes, the resulting change in P-wave traveltime can be seen as a compaction effect. Landrø and Stammeijer (2004) shows that the relative time shift caused by changes in thickness and velocity can be expressed by the following approximation for zero-offset:

$$\frac{\Delta t}{t} \approx \frac{\Delta z}{z} - \frac{\Delta v}{v} \tag{2.1}$$

When the time shifts in Equation 2.1 are created by changes in the water layer, t represents the traveltime through the water layer, z is the water layer thickness and v is the water velocity. Δz and Δv represents the changes in the tidal level and water velocity respectively, while Δt is the resulting time shift caused by these changes.

The magnitude of the time shifts varies with offset MacKay et al. (2003). Inspired by Landrø and Stammeijer (2004), an expression for the offset dependent time shifts measured in a sea bottom receiver was derived. The expression is valid for water layer multiples as well as for the direct wave.

Consider a sea bottom receiver located at offset x and depth z. By assuming that the sea bottom is flat, the traveltime from a source fired at $x = 0, z = 0$ to the sea bottom receiver is

$$t_{n,x} = \sqrt{\frac{(2n-1)^2 z^2}{v^2} + \frac{x^2}{v^2}} = \frac{1}{v}\sqrt{(2n-1)^2 z^2 + x^2} \tag{2.2}$$

where $n = 1$ represents the direct wave, $n = 2$ represents the 1^{st} order multiple of the direct wave, $n = 3$ represents the 2^{nd} order multiple, and so on. v is the velocity. The "mirror method" was used to obtain the traveltime expression in Equation 2.2. The method assumes a flat sea bottom and is demonstrated for the 1^{st} order multiple in Figure 2.1, where the rays to the right are "flipped" across the two boundaries to have the same incidence angle as the first ray. The length that the wave has travelled represents the hypotenuse of a triangle with catheti x and $(2n-1)z$. As shown in Figure 2.1, the direct wave has catheti x and $(2 \cdot 1 - 1)z = z$, while the 1^{st} order multiple has catheti x and $(2 \cdot 2 - 1)z = 3z$. In the same way, the 2^{nd} order multiple will have catheti x and $(2 \cdot 3 - 1)z = 5z$, and so on.

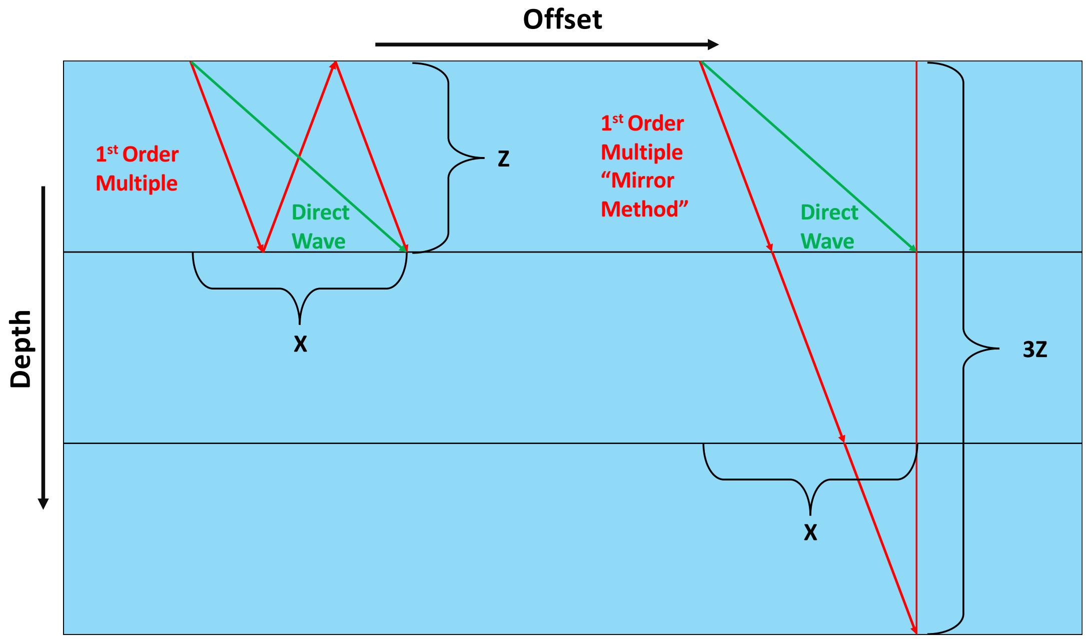

Figure 2.1: Example of the "mirror method" for the 1^{st} order multiple of the direct wave (red). The direct wave (green) is added for comparison. The 1^{st} order multiple has the same traveltime as a wave that has propagated through 3 successive water layers with the same incidence angle. The length the wave has travelled represents the hypotenuse of a triangle with catheti x and $3z$.

The relative changes in thickness and velocity are assumed to be small, i.e. $\frac{\Delta z}{z}, \frac{\Delta v}{v} \ll 1$, and n is assumed to be constant. The differentials of first order of Equation 2.2 then becomes

$$\Delta t_{n,x} \approx \frac{z}{v} \frac{(2n-1)^2}{\sqrt{(2n-1)^2 z^2 + x^2}} \Delta z - \frac{1}{v^2} \sqrt{(2n-1)^2 z^2 + x^2} \Delta v \tag{2.3}$$

By introducing the zero-offset one way traveltime, $T_0 = \frac{z}{v}$ (receivers at sea bottom), Equation 2.3 becomes

$$\Delta t_{n,x} \approx \frac{(2n-1)^2 T_0}{\sqrt{(2n-1)^2 z^2 + x^2}} \Delta z - t_{n,x} \frac{\Delta v}{v} \tag{2.4}$$

By multiply the Δz term in Equation 2.4 with $T_0 \frac{v}{z} = 1$, Equation 2.4 becomes

$$\Delta t_{n,x} \approx \frac{(2n-1)^2 T_0^2}{t_{n,x}} \frac{\Delta z}{z} - t_{n,x} \frac{\Delta v}{v} \tag{2.5}$$

Equation 2.5 can be normalized as

$$\frac{\Delta t_{n,x}}{t_{n,x}} \approx \frac{(2n-1)^2 T_0^2}{t_{n,x}^2} \frac{\Delta z}{z} - \frac{\Delta v}{v} \tag{2.6}$$

where $t_{n,x}$ and $\Delta t_{n,x}$ are the travel time and time shift measured in the sea bottom receiver at offset x for event number n (direct wave/multiple). T_0 is the zero-offset one way travel time and the rest of the parameters are the same as in Equation 2.1. Equation 2.6 is an expression for the offset dependent relative time shift of pre-stack data (with sea bottom receivers). It can be used to calculate the offset dependent relative time shifts for the direct wave ($n = 1$) and its water layer multiples ($n = 2, 3, 4, ...$).

2.2 Overview of Water Column Induced Time Shifts

As the tidal level increases, the water layer gets thicker and the traveltime through the water layer increases. As the water velocity increases, the seismic wave travels faster through the water layer, and the traveltime decreases. The largest time shift between two vintages happens when the tidal level has increased and the water velocity has decreased from one vintage to the other, or the other way around. This can be seen by the opposite sign of Δz and Δv in Equation 2.6, where a positive Δz and a negative Δv will both contribute to increase the magnitude of the time shifts. However, if Δz and Δv are positive/negative simultaneously, the two effects will work against each other to reduce the time shift magnitude.

The time shifts caused by velocity changes varies differently with offset and multiple order than the time shifts caused by tidal changes. This is something that can be inferred by looking at Equation 2.5. For pure tidal changes, ($\Delta z = 0$) and the time shifts in Equation 2.5 reduces to

$$\Delta t_{n,x} \approx -t_{n,x}\frac{\Delta v}{v} \tag{2.7}$$

As seen in Equation 2.7, the time shifts created by pure velocity changes are proportional to the traveltime. Since the traveltime increases for higher multiple orders and increased offset, the magnitude of the time shifts caused by pure velocity changes will also increase with increased multiple order and offset. For time shifts caused by pure tidal changes ($\Delta v = 0$), Equation 2.5 reduces to

$$\Delta t_{n,x} \approx \frac{(2n-1)^2 T_0^2}{t_{n,x}}\frac{\Delta z}{z} \tag{2.8}$$

As seen in Equation 2.8, time shifts created by pure tidal changes are inversely proportional to the traveltime, and the time shift magnitude will hence decrease with increased offset. However, the event number (n) term in Equation 2.8 is squared and will increase more than $t_{n,x}$ as the multiple order increases. Therefore, the time shifts caused by pure tidal changes increases with multiple order.

2.3 Cross-Correlation

Cross-correlation is a mathematical technique that estimates the similarity of two time series. Consider 2 almost identical signals, X and Y that are shifted relative to each other as shown in Figure 2.2. The cross-correlation of the two signals in the continuous domain can be expressed as (Bracewell (2012))

$$cc(t) = \int_{-\infty}^{\infty} X(\tau - t)Y(\tau)d\tau \tag{2.9}$$

and in discrete domain as (Bracewell (2012))

$$cc_i = \sum_{k=-\infty}^{\infty} X_{k-i} Y_k \tag{2.10}$$

When calculating the cross-correlation between two discrete signals, the signals are moved relative to each other at different "lag positions". At each lag position, the cross-correlation is calculated by multiplying the aligning data points of the 2 signals and add all the multiplications together. The output of the cross-correlation is a series of cross-correlation values and their corresponding lag position as visualized in Figure 2.3. Figure 2.3 shows the cross-correlation of the two traces in Figure 2.2. A lag position corresponding to a high positive value of the cross-correlation indicates that the signals are pretty similar and follow more or less the same trend. I.e. X and Y are positive simultaneously and negative simultaneously. A lag position corresponding to a high negative cross-correlation value indicates that the signals follow an opposite trend, i.e. when X is positive, Y is negative and the other way around.

The time shift between two signals can be found by picking the lag position that corresponds to the largest value of the cross-correlation sequence. This is the lag position where the signals are most alike and indicates how much the two signals are shifted relative to each other in time. In Figure 2.3 the maximum amplitude is shown for a time shift around 2.2 ms. This time shift can be confirmed by investigating the distance between the peaks of X and Y in Figure 2.2, which also is around 2.2 ms. If signal Y gets shifted 2.2 ms towards lower traveltimes, it matches signal X almost perfectly.

Assume that the sampling interval of two signals is Δt. Consider a cross-correlation sequence of the two signals and the corresponding lag sequence, L. If the maximum value of the cross-correlation sequence appear at sequence number i, then the time shift, τ, between the signals will be

$$\tau = L_i \Delta t \tag{2.11}$$

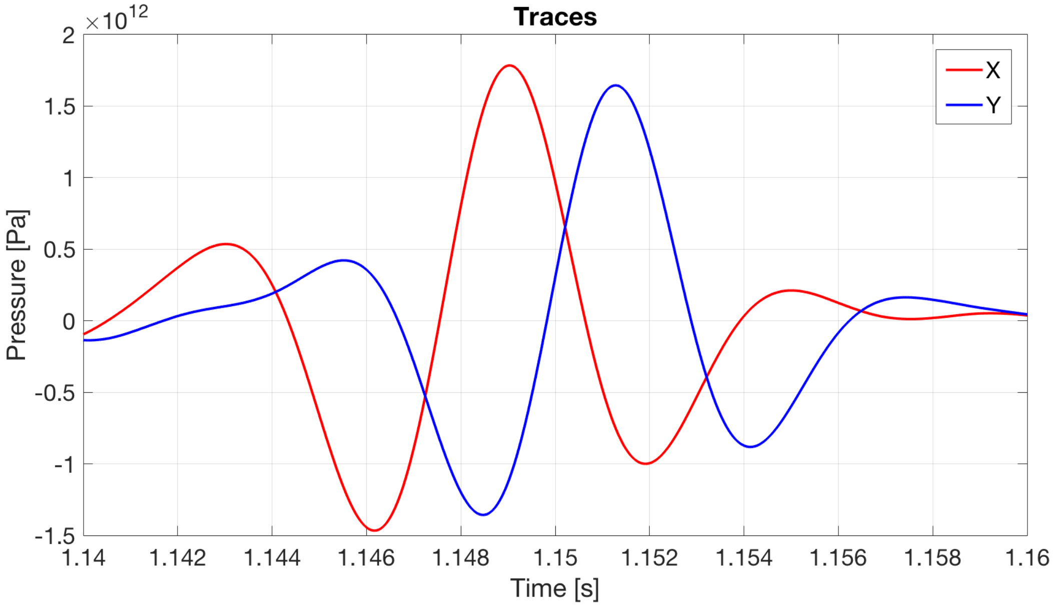

Figure 2.2: Two almost identical traces time-shifted relative to each other. The time shift between the traces is ≈ 2.2 ms.

Figure 2.3: The cross-correlation sequence of the two traces in Figure 2.2. The maximum cross-correlation value corresponds to a time shift of ≈ 2.2 ms.

2.4 Windowed Cross-Correlation

Consider 2 seismic traces representing the same source and receiver positions but different water velocity and tidal level. The time shift between two traces will not be constant, but will vary along the two traces. Each event present on the two traces will have a specific time shift, and a single global cross-correlation will not capture these local time shift variations Hale et al. (2006). Windowed cross-correlation is a cross-correlation technique that measures the time shift of the traces within a specific time interval. A window of a specified length (in time) is defined and only the parts of the 2 traces that fall inside the window boundaries are included in the cross-correlation calculations Hale et al. (2006). Figure 2.4 illustrates the concept of the windowed cross-correlation, where the red rectangle illustrates a window length of ≈ 19 ms. Inside the window, the maximum of the cross-correlation sequence is found, along with its corresponding time shift.

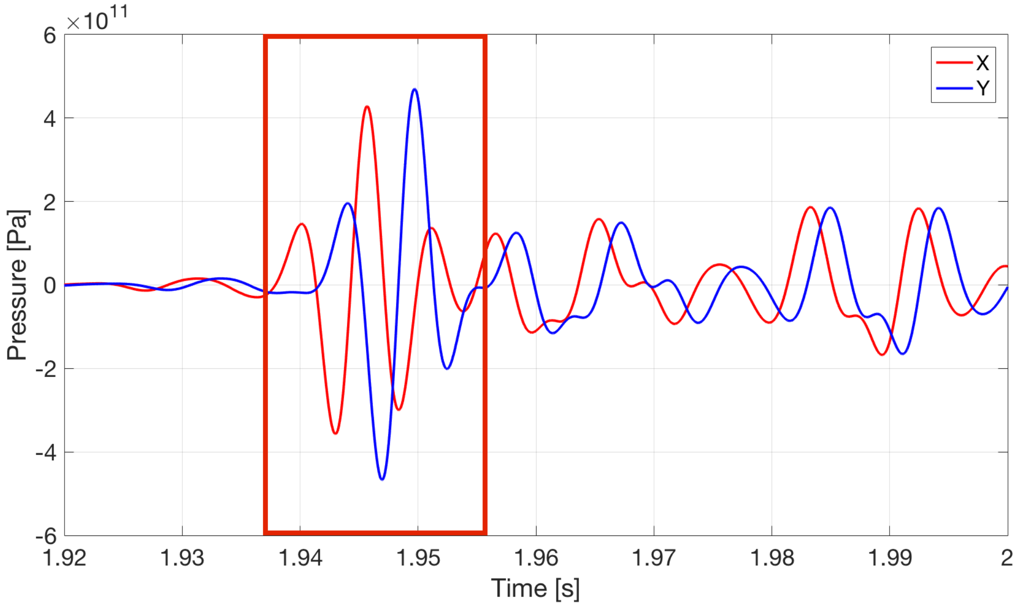

Figure 2.4: Illustration of the windowed cross-correlation. Red rectangle illustrates a window of ≈ 19 ms. The maximum cross-correlation value and its corresponding time shift are calculated for the parts of the 2 traces that fall inside the window boundaries.

The windowed cross-correlation gives the possibility to investigate how the time shifts between two signals vary for different events. Inside one window, the time shift between two traces is assumed to be constant Hadziioannou et al. (2009). Thus, the window length has a large impact on the resulting time shifts. For good time shift calculations, it is important to find the optimal window length for the specific objective of the cross-correlation process. The time shift for a single event will be best estimated with a window that only captures the specific event in the two traces, and excludes everything else. In this way, the time shift estimates will not be affected by the surrounding signal and the correct time shift between the events will be calculated.

2.5 Inversion

Inversion is the process of using actual measurements to find the values of the model parameters of a physical system that give rise to the measurements Tarantola (2005).

Inversion, or the inverse problem, is the opposite of the forward problem. The forward problem takes the model parameters and calculates the response. Let m be the model, consisting of different parameters. Let F be the forward operator, i.e. the mathematical model of the physical system that is investigated. The predicted values of the measured parameters d is given by the forward modelling as

$$d = F(m) \tag{2.12}$$

The different models can be thought as points in a "model space", an abstract space that contains all conceivable models Tarantola (2005). By forward modelling each of these models, they will give a specific response. These responses can be thought as points in the data space, an abstract space which contains the resulting responses after forward modelling of the models. The model space and the data space is illustrated by the blue and the yellow ellipses in Figure 2.5 respectively.

Inversion works in the opposite way of the forward modelling. By starting with some observed data in the data space and proceed backwards to find what model that gives rise to the observations. Hence inversion becomes a problem of finding a model, m, that minimizes the difference between the forward calculated response and the observed data.

The inverse problem is defined by an objective function, which is the function that is minimized during the inversion process. The objective function can be expressed as

$$\phi(m) = \phi_d + \beta\phi_m \tag{2.13}$$

where ϕ_d is the data misfit function, ϕ_m is the model misfit function and β is the regularization parameter. The data misfit function measures the error between the observed and forward modelled data. The model misfit function is added to include prior information about the model, e.g. if a model is assumed to vary smoothly or abruptly. β controls the relative weighting between ϕ_d and ϕ_m Oldenburg and Li (2005).

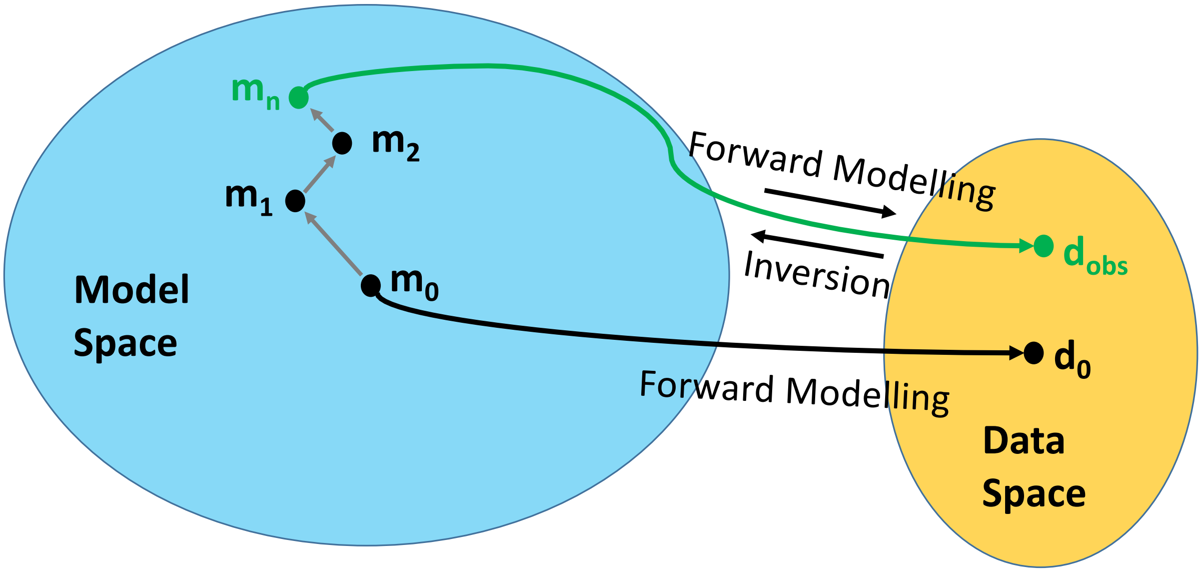

Figure 2.5: Illustration of the inversion process. The blue ellipse illustrates the model space containing all conceivable models. The yellow ellipse illustrates the data space containing the data points after forward modelling of the models in the model space. The inversion process starts with a forward modelling of the start model, m_0, and the corresponding value of the objective function is calculated. The start model is updated and the forward response and objective function is again calculated. m_1 and m_2 represent different models in the model space. The process goes on until the model that best describes the observed data is found. This model is illustrated by the green m_n, which results in a point in the data space close to the observed data, d_{obs}. This is where the objective function, Equation 2.13, reaches a minimum.

The data and model misfit functions can be defined with different norms. For the data misfit function with the L1 norm, the misfit is calculated by taking the absolute value of the error between the observed data, d_{obs}, and forward modelled data, $F(m)$, on the form (Tarantola (2005))

$$\phi_d(m) = ||d_{obs} - F(m)||_1 = |d_{obs} - F(m)| \tag{2.14}$$

The misfit calculated with the L2 norm, calculates the misfit by the least squares method, expressed as (F. Jones (2007))

$$\phi_d(m) = ||d_{obs} - F(m)||_2 = (d_{obs} - F(m))^2 \tag{2.15}$$

As illustrated in Figure 2.5, inversion is an iterative process. To begin, a start model, m_0, must be defined. The forward response d_0 due to this start model is calculated.

$$d_0 = F(m_0) \tag{2.16}$$

The value of the objective function due to the start model is calculated with Equation 2.13. The start model is then updated and the and the forward response and objective function value are again calculated. This process goes on until the objective function converges to a minimum or becomes acceptably small Tarantola (2005).

The forward problem has an unique solution, while the inverse problem often has multiple solutions Tarantola (2005). Several combinations of the model parameters might give rise to a forward model which can explain the observed data. To exclude unrealistic models, constraints/ bounds can be added to the inversion.

Uncertainties and noise in the measured parameters, along with simplifications and approximations in the model and forward operator, makes it hard to make the predicted parameter values, d, identical to the observed data. Hence, in general, there exist some uncertainty connected to the predicted parameter values Tarantola (2005).

2.6 Global Search Algorithm

During the inversion in this project, it was important to find the global minimum and avoid falling into local minimums. For this purpose, the built-in "Global Search Algorithm" in MatLab was used. The Global Search Algorithm uses a Scatter Search Algorithm to generate a set of start points within finite bounds defined by the maximum and minimum values of the parameters that are to be investigated. The Scatter Search Algorithm is constructed to perform an intelligent search on the problem domain Ugray et al. (2007). See Glover (1998) for a detailed described of the Scatter Search Algorithm. From the start points found, the Global Search Algorithm evaluated several basins of attraction. The basin of attraction is the set of start values that lead to the same local minimum Grebogi et al. (1984). Within each basin of attraction, the minimum was found by a local gradient-based non-linear solver. The lowest minimum in all the basins of attraction resulted in the global minimum. See Ugray et al. (2007) for a detailed description of the Global Search Algorithm.

2.7 Raytracing Theory

Seismic ray theory is the high-frequency asymptotic method for studying wave fields, where the seismic waves are assumed to behave like straight rays. The ray theory is approximate, but can give good solutions in a smoothly varying media with smooth interfaces Červený and Pšenčík (2011).

The acoustic wave equation is given as

$$\frac{\partial^2 P}{\partial t^2} = c^2 \nabla^2 P \tag{2.17}$$

where P is the pressure c is the P-wave velocity and t is time Landrø (2011). By applying a temporal Fourier-transformation to the wave equation in Equation 2.17, one gets

$$\nabla^2 P + (\frac{\omega}{c})^2 P = 0 \tag{2.18}$$

where P is pressure, ω is the angular frequency and c is the P-wave velocity. One solution of Equation 2.18 can be expressed as (Landrø (2011))

$$P(\omega, x) = P_0(\omega) A(x) e^{i\omega\tau(x)} \tag{2.19}$$

where $P_0(\omega)$ is the Fourier-transform of the signal transmitted from the source, A(x) is the amplitude at position x and $\tau(x)$ is the traveltime to position x. By inserting Equation 2.19 into Equation 2.18, the following is obtained (Landrø (2011))

$$\nabla^2 A + 2i\omega \nabla A \nabla\tau + i\omega A \nabla^2 \tau - \omega^2 A (\nabla\tau)^2 + (\frac{\omega}{c})^2 A = 0 \tag{2.20}$$

By separating the imaginary and real parts of Equation 2.20, the imaginary Equation 2.21 and real Equation 2.22 are obtained (Landrø (2011))

$$2\nabla A \nabla\tau + A\nabla^2\tau = 0 \tag{2.21}$$

$$\nabla^2 A - \omega^2 A (\nabla\tau)^2 + (\frac{\omega}{c})^2 A = 0 \tag{2.22}$$

By taking the high frequency limit ($\omega \rightarrow \infty$) of the real part in Equation 2.22, the Eikonal equation is obtained (Landrø (2011))

$$(\nabla \tau)^2 = \frac{1}{c^2} \tag{2.23}$$

Equation 2.23 acts as the basis for kinematic raytracing, where the traveltimes, τ, are calculated along ray paths.

As a seismic wave hits the interface between 2 layers, it will be transmitted and reflected. For high frequencies ($\omega \rightarrow \infty$) Snell's law relates the incidence angle of the wave to the transmitted and reflected angle by (Landrø (2011))

$$\frac{sin(\theta_I)}{c_I} = \frac{sin(\theta_R)}{c_R} = \frac{sin(\theta_T)}{c_T} \tag{2.24}$$

In Equation 2.24 c is the P-wave velocity and θ is the angle for the incidence (I), reflected (R) and transmitted (T) rays.

In a medium consisting of constant velocity, homogeneous layers, the ray paths calculated by Equation 2.23 become straight lines. By using Snell's law for computation of the ray bending across the interfaces, it is possible to trace the ray paths through the layered medium Landrø (2011). This is the principle behind kinematic raytrace modelling.

2.8 Synthetic Seismograms With Kenneth-Bouchon

Synthetic seismograms computed with the Kennett-Bouchon approach, abbreviated SKB, is a numerical seismic wave propagation program. The Kennett-Bouchon approach creates seismograms in the time-distance domain by combining Kennett's generalized reflection and transmission matrix method for propagation of plane waves in a stratified medium Kennett (1974), with Bouchon's discrete wave number integration technique Bouchon (1981).

The computation used in SKB consists of several steps. First the plane-wave reflectively is obtained with Kennett's method. Then the response of the medium is obtained by discrete wave number integration of plane wave reflectivity with Bouchon's method Dietrich (1988).

The propagation medium used by the SKB program is 1D and consists of elastic and isotropic plane layers. The base layer is a homogeneous elastic half-space, while the top of the uppermost layer is a stress-free surface. The source is a point source, emitting a zero phase Ricker wavelet, and the simulation program includes both homogeneous and inhomogeneous P-waves, SH-waves and SV-waves. Effects like mode conversions, multiple reflections, surface waves, interface waves and near field effects are included. The SKB output is 4 seismograms, one for pressure, and one for each displacement in the x, y and z directions.

Chapter 3

The Snorre Field and Data

Snorre is an oil and gas field located in the Tampen area of the Norwegian North Sea, in Block 34/4 and 34/7. The location of Snorre is shown in Figure 3.1. The field was discovered in 1979 and the production started in 1992 Oljedirektoratet (2017).

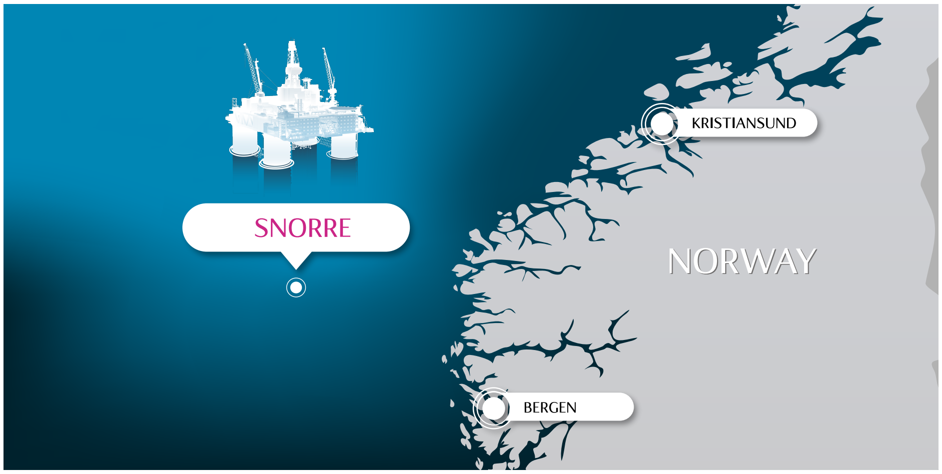

Figure 3.1: The location of the Snorre field offshore Norway. The image is taken from Statoil (2017).

3.1 Permanent Reservoir Monitoring Data

At Snorre, there are permanently installed ocean bottom seismic cable systems and several permanent reservoir monitoring (PRM) surveys have been performed. For the use of this Master's Thesis project, Statoil provided with one shot and one receiver line from 2 of the

Snorre PRM datasets. PRM 4, acquired October 10th 2015 and PRM 5 acquired June 9th 2016. The pressure data from these two vintages was used in this project.

The receiver line used in this project, line 27, is located approximately in the middle of the Snorre field, going from west to east. Figure 3.2 shows the distribution of the ocean bottom receivers at Snorre. The red line illustrates the location of the shot line used in this project. Receiver line 27 is located approximately below this shot line.

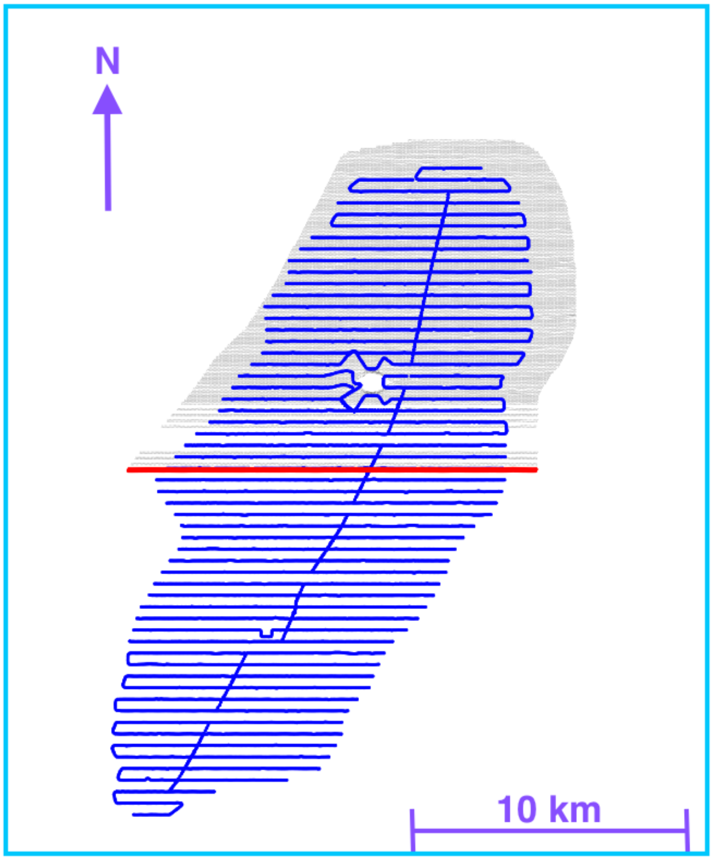

Figure 3.2: Blue horizontal lines illustrate the distribution of the ocean bottom seismic cable systems at Snorre. The red line illustrates the location of the shot line used in this project. The receiver line used in this project, line 27, is located approximately below the red line. The blue line going through the ocean bottom receivers in south west - north east direction is infrastructure at the sea bottom.

Figure 3.3 shows the source and receiver positions for the shot and receiver lines used in this project. The axes are given in distance from the "first receiver". In this report, the "first receiver" is defined as the receiver to the far west at receiver line 27, corresponding to the receiver to the far left in Figure 3.3.

Receiver line 27 consists of 233 receivers, spaced 50 meters apart and buried $0.5-1$ meter down into the sea floor. As seen in Figure 3.3 the receivers do not form a perfectly straight line and there are some variations in the crossline direction. This is especially prominent for the receivers between 6000 - 8000 meters. These deviations are most likely due to infrastructure and obstacles at the sea floor, forcing the receivers to be located at other positions.

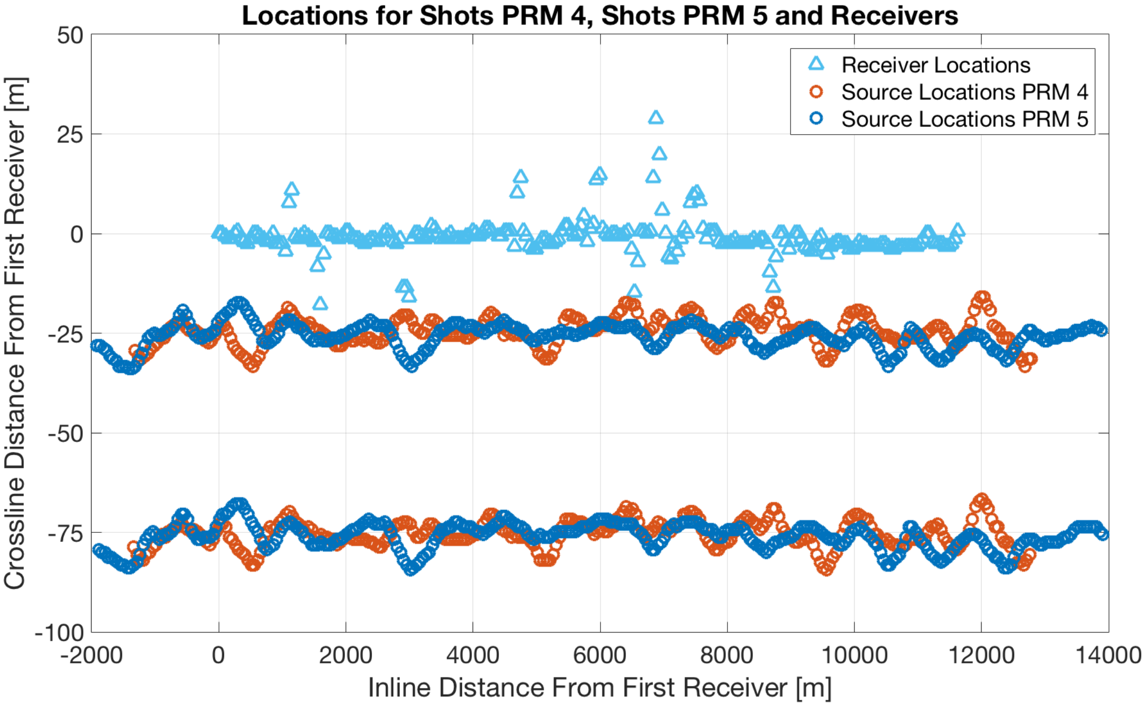

Figure 3.3: Source locations for PRM 4 (red circles), PRM 5 (dark blue circles) and receiver locations (light blue triangles). The shot position makes up 2 "lines", representing 2 source arrays, separated by about 50 meters. The acquisition was performed flip-flop, with a flip-flop shot spacing of 25 meters. The vessel was sailing from left (west) to right (east) in this figure, a line direction of 90 degrees. Note the difference in source position between the two vintages. Also, note the scale difference between the axes.

During the acquisition of the shot lines in PRM 4 and 5, the vessel was sailing from west to east, corresponding to left to right in Figure 3.3. The vessel was towing 2 source arrays separated by 50 meters. The acquisition was performed flip-flop, with a flip-flop shot spacing of 25 meters. The number of shots in PRM 4 was 566, while PRM 5 contained 634 shots. 23 of the excess shots in PRM 5 were located to the west of the first shot in PRM 4. 45 of the excess shots in PRM 5 were located east of the last shot in PRM 4. The excess shots are shown by the blue circles to the far left and far right in Figure 3.3. The rest 566 shots were located at approximately the same inline positions for both vintages. However, as seen in Figure 3.3, there were some differences between PRM 4 and 5 in the source crossline positions.

Seismic Interference

During the acquisition of Snorre PRM 4, a neighbouring seismic vessel was also shooting seismic, resulting in seismic interference. Figure 3.4 shows a shot gather from PRM 4 where the events from the neighbouring vessel (dipping to the right) are highlighted by the red arrows. The events from the neighbouring vessel had relatively high amplitudes, and at large offsets highlighted by the red ellipse, the amplitude of the events from the neighbouring seismic vessel was approximately equal to the amplitudes of the events from the PRM 4 source. The seismic interference was present throughout in the whole PRM 4 dataset.

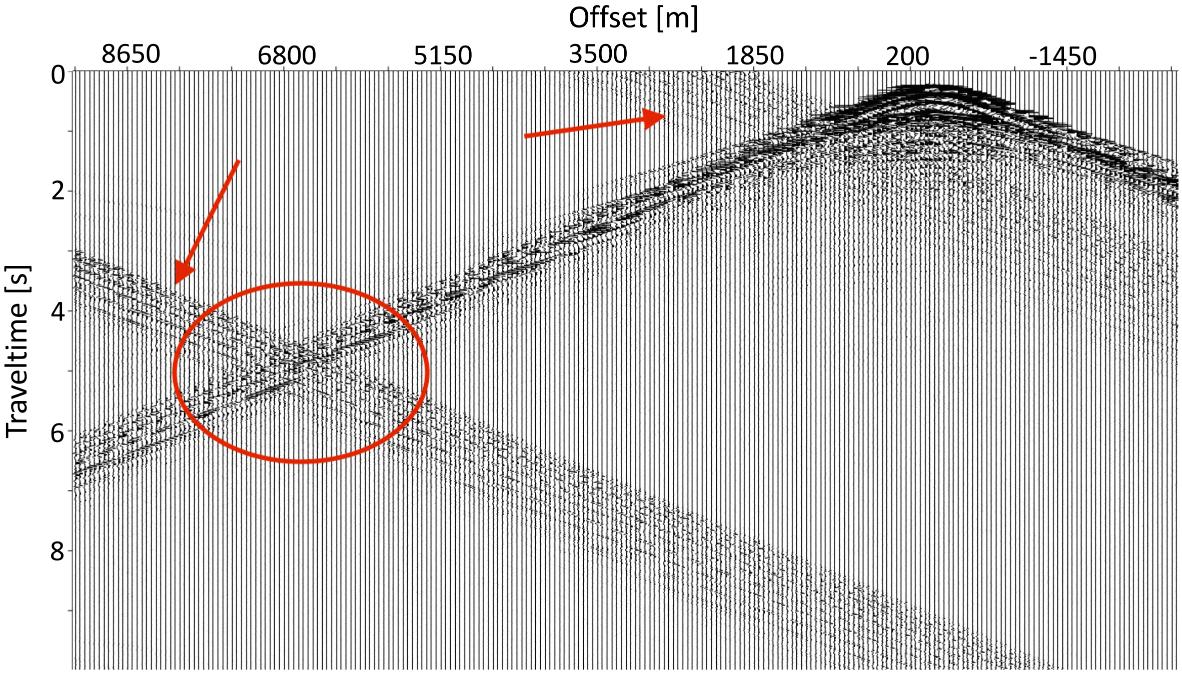

Figure 3.4: Shot gather from PRM 4, showing seismic interference of shots from another seismic vessel. The seismic interference is highlighted by the red arrows and is dipping to the right. The events dipping towards left (at positive offsets) are the actual PRM 4 events. The red ellipse highlights a zone where the shot from the other vessel interferes with the PRM 4 events.

3.2 Sea Bottom at Snorre

The sea bottom at Snorre is not totally flat, but varies slightly along line 27. The sea bottom is shown in Figure 3.5, representing the water depth measured at the sea bottom receivers. In general, the water depth increases from the first to the last receiver along line 27, from 318.7 to 354.6 meters. This corresponds to a total water depth variation of ≈ 36 meters. As receiver line 27 is 11631 meters long, the 36 meters water depth difference does not give rise to a very steep dip at the sea floor. Therefore, locally the sea floor can be assumed to be relatively flat.

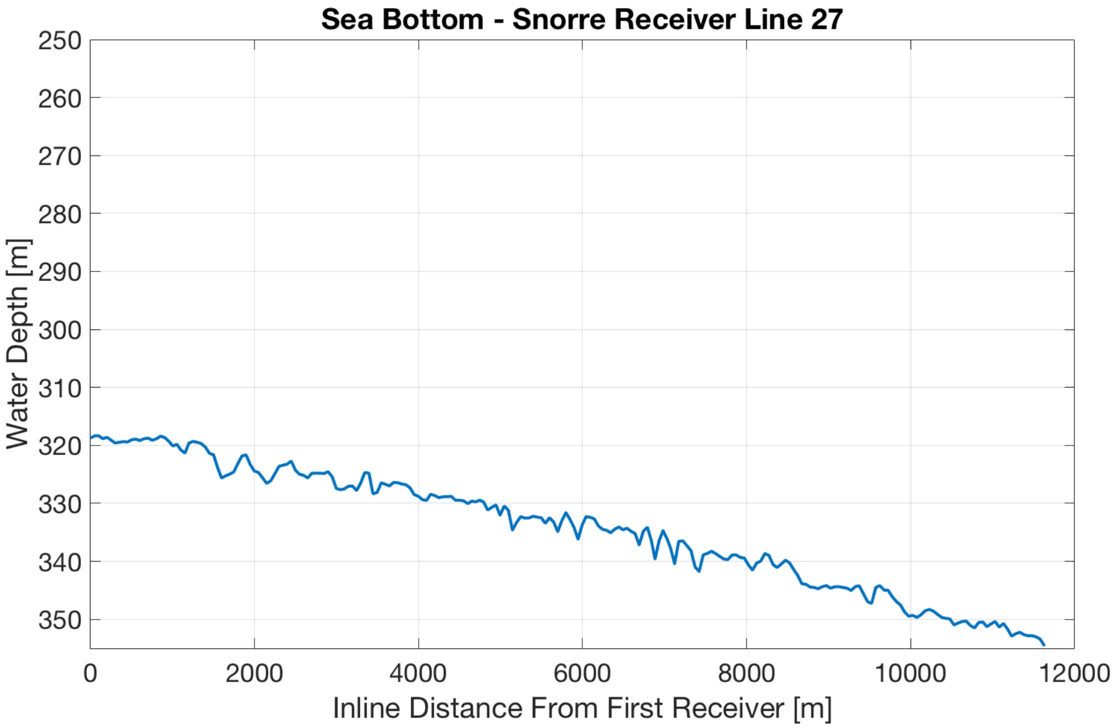

Figure 3.5: Water depth for the receivers along receiver line 27, measured with multi-beam echo sounders. The x-axis is given in "Inline Distance From First Receiver". The first receiver is located to the far west at receiver line 27.

3.3 Reference Measurements of Water Velocity and Tides

There are several measurements of the water velocity and tidal level at Snorre that were used as reference measurements in this project.

PIES is an abbreviation for "Pressure Inverted Echo Sounder". As indicated by the name, the PIES contains a pressure sensor along with an Inverted Echo Sounder. The PIES is deployed on the sea floor and calculates the water depth and tidal variations from the pressure measurements. The water velocity is calculated with the Inverted Echo Sounder Wang et al. (2012). See Appendix B.2 for more information about the PIES.

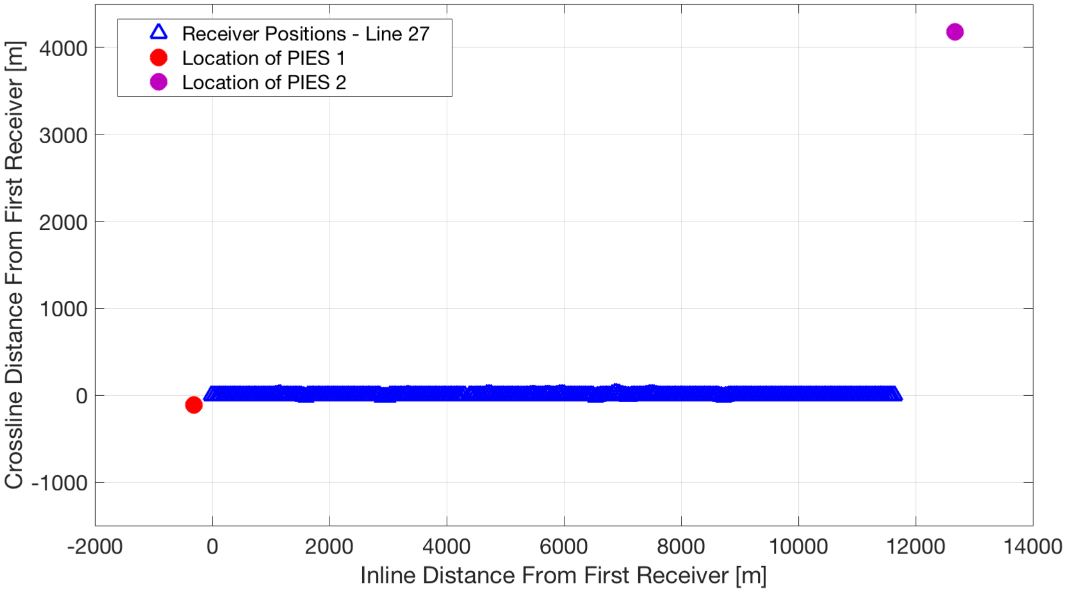

Figure 3.6: Figure shows the location of PIES 1 and 2 relative to receiver line 27. The red dot shows the position of PIES 1, located only 332 meters from the first receiver. The purple dot shows the location of PIES 2, located 4308 meters from the last receiver. "First receiver" is the receiver to the far left (west) in the figure, while "last receiver" is the receiver to the far right (east) in the figure. The scales of the x and y-axis are not equal.

Two PIES were located at the Snorre field and acquired information about the water depth and the water velocity every 10th minute. The position of the two PIES relative to receiver line 27 is shown in Figure 3.6. PIES 1 was located very close to receiver line 27, only 332 meters in horizontal distance from the first receiver. PIES 2 were located further away, 4308 meters in horizontal distance from the last receiver at line 27. There were reports of some instability in the measurements of PIES 1 around the time PRM 4 was acquired. So, even though PIES 1 was located closest to receiver line 27, the average of the tidal level measured in PIES 1 and PIES 2 was used as the reference for the tidal estimates in this project. PIES 2 was located in an area of larger water depths than PIES 1. Due to lower temperatures at larger water depths, PIES 1 was expected to measure higher velocities than PIES 2. However, since the water depth varies along receiver line 27, the average of the velocity measurements in PIES 1 and PIES 2 was used as the reference for the water velocity in this project.

Tidal Level Measurements

As the tidal level changes continuously, the tidal level varied throughout the acquisition of both PRM 4 and 5. For the shot lines used in this project, the time from first to last shot was 95 minutes for PRM 4 and 109 minutes for PRM 5. The reason for the larger acquisition time for PRM 5 was due to the 68 excess shots, described in Section 3.1. To compare the PIES measurements of the tidal levels in the two vintages, the measured tidal levels for PRM 5 was scaled to fit the number of shots in PRM 4.

The PIES measurements of the tidal level for PRM 4 and 5 are plotted against time from the first shot in Figure 3.7. In addition, the tidal level difference between PRM 4 and 5 is shown, calculated by subtracting the tidal level of PRM 4 from the tidal level of PRM 5. The tidal level decreases from first to last shot in PRM 4, while it increases from first to last shot in PRM 5. The tidal level difference is approximately a linear line increasing from ≈ -0.1 meters at the time of the first shot to ≈ 0.8 meters at the time of the last shot. Even though the tidal variations within each survey are below 0.5 meters, the tidal level difference varies with almost 1 meter since the tidal level in the two vintages moves in opposite directions with time from the first shot.

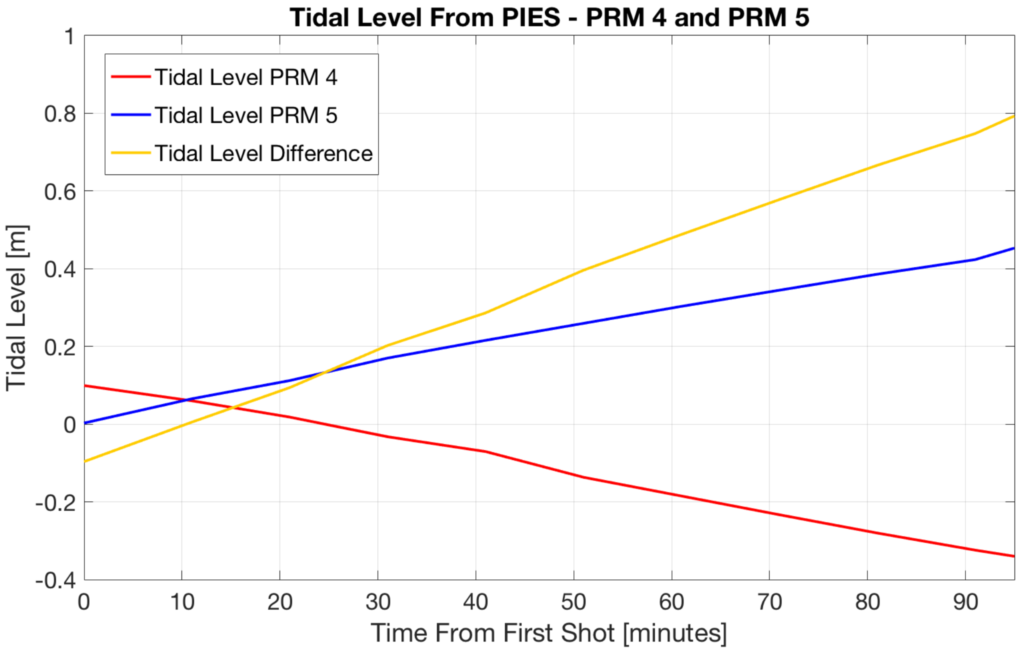

Figure 3.7: PIES measurements of the tidal level variations with time from the first shot. The red curve shows tidal variations for PRM 4, while blue curve shows tidal variations for PRM 5. Both tidal level curves represent the average of the tides measured in PIES 1 and 2. The measurements for PRM 5 were scaled to fit the same amount of shots as in PRM 4. Time = 0 represents the time of the first shot in PRM 4 and the time of the corresponding shot in PRM 5. The yellow line shows the tidal difference between the two surveys, calculated by subtracting the tidal level of PRM 4 from the tidal level of PRM 5.

To quality check the PIES measurements of the tidal level, pressure corrected tidal predictions was investigated. The pressure corrected tidal predictions are predicted using a tidal model, corrected for air pressures by air pressure measurements from a nearby weather station. The pressure corrected tidal predictions are shown in Figure 3.8, for the same time window as the given shot lines in PRM 4 and PRM 5 were acquired. The pressure corrected tidal predictions are only sampled once an hour and is interpolated in Figure 3.8, but the main trends are the same as for the PIES measurements in Figure 3.7. The tidal level in the two surveys moves in opposite directions, and the tidal difference increases with time from first shot. The variation in tidal level is a little less and the difference curve is pushed slightly towards lower values for the pressure corrected tidal predictions in Figure 3.8 compared to the PIES measurements in Figure 3.7. However, the pressure corrected tidal predictions seem to be relatively consistent with the tidal levels from the PIES measurements.

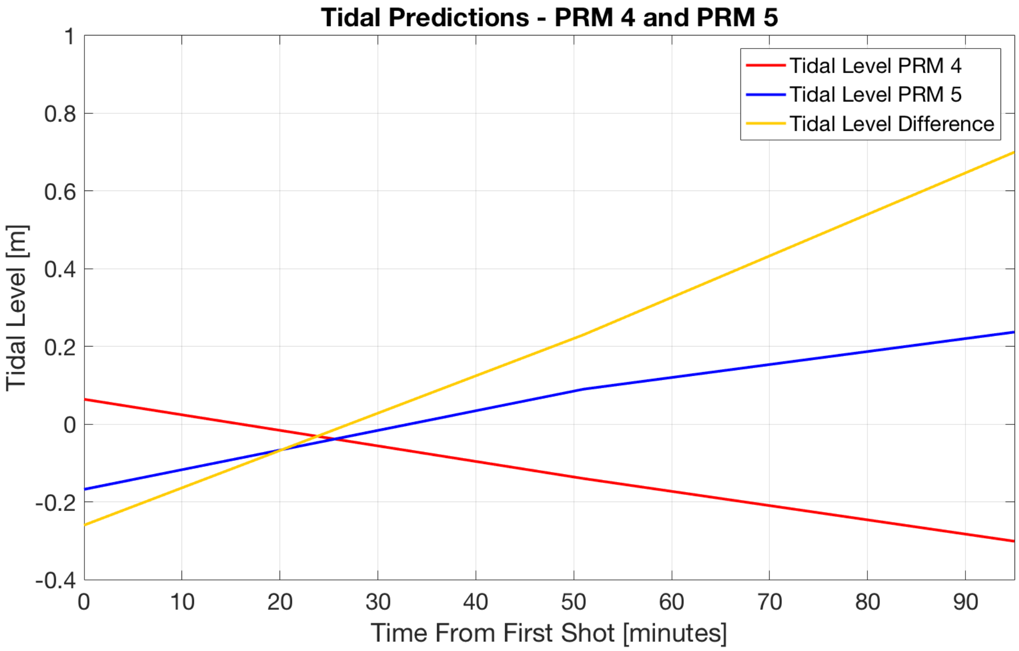

Figure 3.8: Pressure corrected tidal predictions for PRM 4 (red) and PRM 5 (blue), for the time window of acquisition of the given shot lines in the two vintages. The yellow line shows the tidal level difference between the two vintages, calculated by subtracting the tidal level for PRM 4 from the tidal level for PRM 5. The tidal levels are predicted using a tidal model, corrected for air pressures by air pressure measurements from a nearby weather station.

Water Velocity Measurements

The PIES measurements of the water velocity over the time period the shot lines in PRM 4 and 5 were acquired, are shown in Figure 3.9 (a) and (b) respectively. As expected, the velocities measured in PIES 2 are lower than the velocities measured in PIES 1. Since PIES 2 is located in deeper water, the waves emitted from PIES 2 have a greater proportion of their travel path in the colder water with lower velocity, which reduces the measured average velocity compared to the measurements in PIES 1. The average velocity is highlighted by the green line in each plot. The average velocity for PRM 4 is 1490.67 m/s, while it is 1487.40 m/s for PRM 5, a difference of 3.27 m/s. The standard deviation of the velocity estimates is 1.738 m/s for PRM 4 and 0.686 m/s for PRM 5. Since the Sun heats up the water during the summer, the water temperatures are larger for PRM 4 acquired during early autumn, than for PRM 5 acquired during early summer.

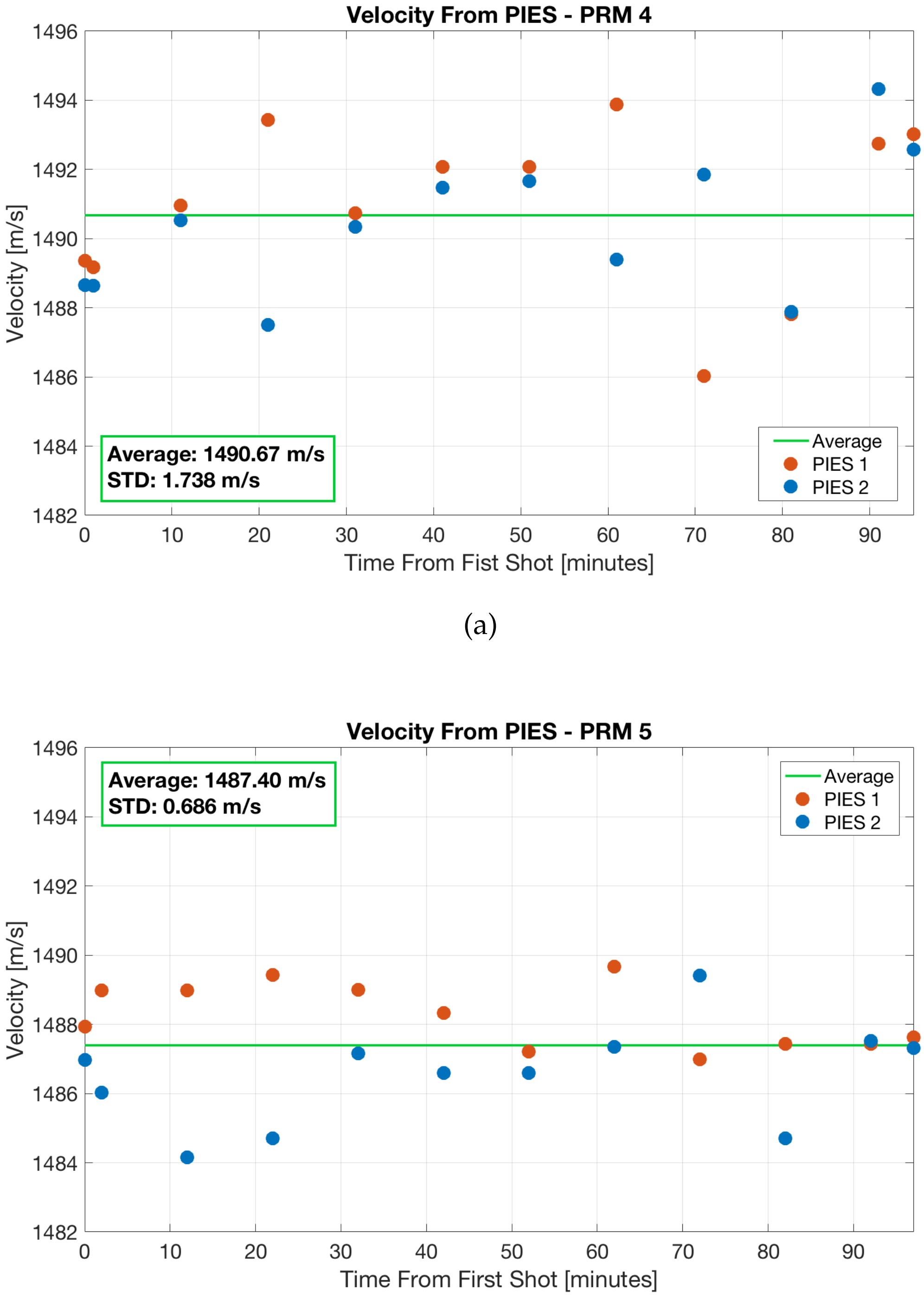

(a)

(b)

Figure 3.9: Measured water velocities from the PIES for PRM 4 (a) and PRM 5 (b). The PRM 5 measurements were scaled to fit the same amount of shots as in PRM 4. The plots show how the water velocity changes with time from the first common shot. The red dots correspond to PIES 1 and the blue dots corresponds to PIES 2. The green line shows the average velocity, which also is given in the green boxes together with the standard deviations of the velocity measurements.

To quality check the velocity measurements from the PIES, TS Dip velocities from the Snorre field were investigated. TS Dip is an acronym for Temperature Salinity Dip. Originally the TS Dip was a device that measured the temperature, salinity and depth and from this calculated the velocity. However, the TS Dip device used at the Snorre field measured the velocity in the water directly by measuring the traveltime of an acoustic wave over a short fixed distance in the water. By performing TS Dip measurements at different, discrete depths, velocity profiles were obtained.

TS Dip data is not acquired very often, so the closest TS Dip acquisition to the actual acquisition date for the given shot line in PRM 4 and 5 were used, and are shown in Figure 3.10. The red curve shows TS Dip data acquired 2 days before the acquisition of the given shot line in PRM 4, while the blue curve shows TS Dip data acquired 5 days later than the given shot line in PRM 5. As seen in Figure 3.10, the velocity for PRM 4 is much larger than PRM 5. In addition, both vintages have velocity variations with depth. Since the sun heats up the uppermost parts of the water layer the most, the top parts have high velocities. As the temperature decreases with depth, the velocity follows the same trend, which is especially evident for the velocity profile for PRM 4.

The deepest sample point for PRM 5 is around 316 meters, while the deepest sampling point for PRM 4 is 386 meters. By only considering measurements down to 316 meters, the average velocity is 1491.09 m/s for PRM 4, while the average velocity for PRM 5 is 1489.27 m/s. The velocity difference between the two is 1.82 m/s, which is a much lower difference than the one measured from the PIES data. The reason for this difference can be that the PIES and the TS Dip measurements were acquired at different locations and that the TS Dip velocities were acquired 2 days before and 5 days later than the PIES measurements for PRM 4 and 5 respectively.

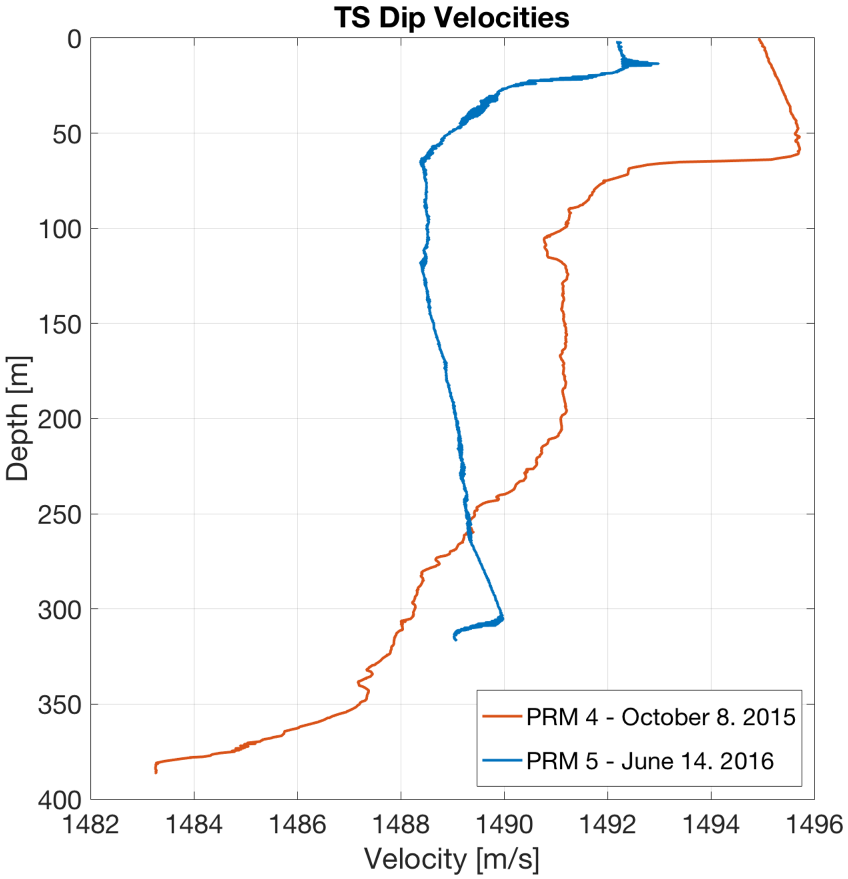

Figure 3.10: TS Dip water velocity profiles. The red curve represents velocities measured 2 days before the acquisition of the given shot line in PRM 4. The blue curve represents velocities measured 5 days after the acquisition of the given shot line in PRM 5. Note the large velocity for the uppermost 60 meters for the red curve and the uppermost 15 meters for the blue curve. The bottom of the water column is expected to be the coldest part. However, the blue curve has a strange up-dip at the lower part of the velocity profile. This can be due to wrong measurements or due to other factors that affect the velocity, like the salinity content in the water or pressure.

Chapter 4

Method for Estimating Water Column Changes

The first part of this chapter, Section 4.1, describes the TSCI (Time Shift Curve Inversion) method developed during this project for estimating the water velocity and tidal changes between the 4D vintages. A central part of the TSCI method, the symmetry correction described in Section 4.1.3, was based on the observations and implications of a test. This test therefore is shown together with the description of the symmetry correction in Section 4.1.3. The last part of this chapter, Section 4.2 and 4.3, describes different tests performed on synthetic data in order to investigate the advantages and limitations of the TSCI method.

4.1 Time Shift Curve Inversion

For estimating the water velocity and tidal changes between the 4D seismic vintages, a method named "Time Shift Curve Inversion", abbreviated "TSCI", was developed with the use of the MatLab software and the 4D seismic data from the Snorre field. The method utilizes inversion based on the water column induced time shifts and consists of 2 main steps:

- Time shift curves are found by a trace-by-trace cross-correlation of the water column events in two 4D seismic vintages.

- Inversion is performed based on the time shift curves, using a 1D raytracing model for calculating the forward response. The result is the estimates of the changes in water velocity, tidal level and start of data delay between the vintages. (See Section 4.1.5 or Appendix A.2 for explanation of "start of data delay").

In addition, source position corrections and outlier removal are performed to increase the quality of the time shift curves. The TSCI method is further described in the following sections.

4.1.1 Calculation of Time Shifts Caused by Water Column Changes

In this section, it is described how the water column induced time shift curves were calculated, which were the basis for the inversion described later.

Consider 2 seismic vintages acquired over the same ocean bottom receivers. To calculate the water column induced time shifts between the vintages, a trace-by-trace cross-correlation method was used. The vintages were sorted into common shot gathers. The 2 shot gathers representing approximately the same shot point in the 2 vintages, were sorted into "common shot gather pairs". The receiver positions are fixed at the sea bottom for both vintages. Hence, each trace in one of the shot gathers in the common shot gather pair, has a corresponding trace in the other shot gather with approximately the same offset. These two traces make up a "trace pair". This is illustrated in Figure 4.1. The uppermost part represents a common shot gather pair of approximately the same shot position in two seismic vintages, Vintage 1 and Vintage 2. The lowermost part of Figure 4.1 illustrates two traces representing the same receiver position in the two shot gathers.

In this Master's Thesis "the water column events" are defined as the direct wave and the water layer multiples of the direct wave. For each "trace pair", the arrival times for the water column events, were predicted by a simple 1D raytracing model. The raytracing model was based on an approximate absolute water velocity found with the "Near Offset Method" described in Appendix B.3, along with approximate water depths and the receiver offsets given in the header of the seismic data. The raytracing model is further described in Section 4.1.5.

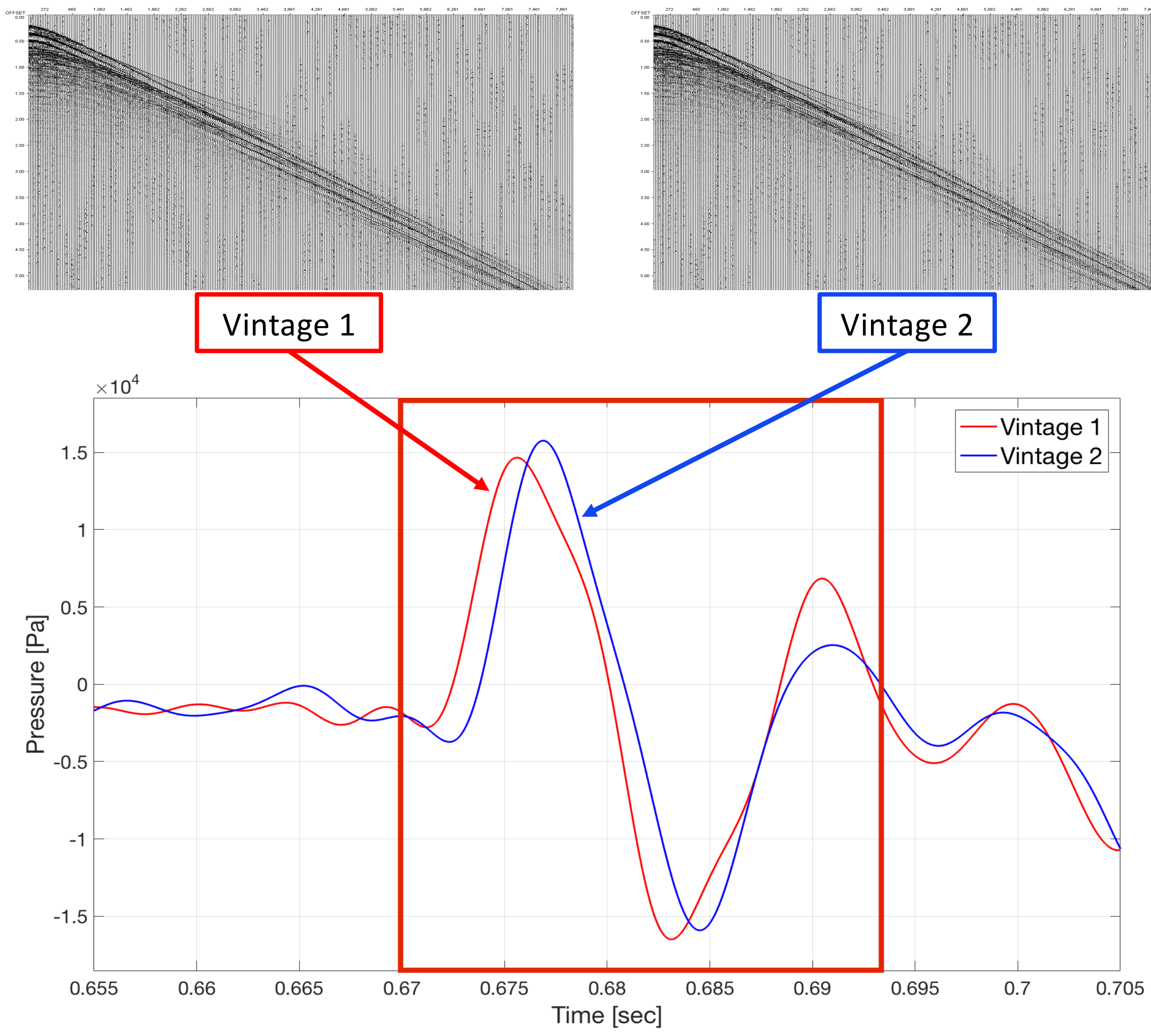

Figure 4.1: Illustration of the process of extracting the traces used for cross-correlation. At the top, two shot gathers (a shot gather pair) are illustrated. These represent the same shot, but different vintages, vintage 1 to the left and vintage 2 to the right. The traces representing the same receiver in the two shot gathers are extracted, illustrated in the lowermost part of the figure, where the red trace corresponds to vintage 1 and the blue trace corresponds to vintage 2. Note the clear time shift between the two traces. The red rectangle illustrates a window of ≈ 23 ms, designed to capture the first order multiple of the direct wave in both traces (the window used for the Snorre data was 40 ms long). The time shift between the traces for the first order multiple was found by cross-correlating the part of the signals that fell inside of the window boundaries.

For each water column event, a time window of a specific length was made around the predicted arrival time for both traces in the trace pair. Since the arrival time predicted by the 1D raytracing model was based on approximate water velocity and water depths, a window length of 40 ms was used to make sure the events were "captured". Such a window is illustrated by the 23 ms wide red square in Figure 4.1, which captures the first order multiple of the direct wave for both traces. Note the clear shift in time between the two traces inside the red square. The time shift between the traces was found by cross-correlating the part of the traces that fell inside of the window. The theory behind the cross-correlation is described in Section 2.3 and 2.4.

The windowed cross-correlation process was performed for all trace pairs in the common shot gather pair. Since each trace pair represents a different offset, the calculated time shifts could be plotted against offset. An example is shown in Figure 4.2, which illustrates how the time shift for the direct wave varies with offset for the trace pairs in a common shot gather pair.

Figure 4.2 represents the time shift curve for only one event in only one shot gather pair. However, Snorre PRM 4 and 5 consisted of 566 shot gather pairs and the process described above was performed for all 566 of them. In addition, for each shot gather pair, the time shift curve for several water column events was made.

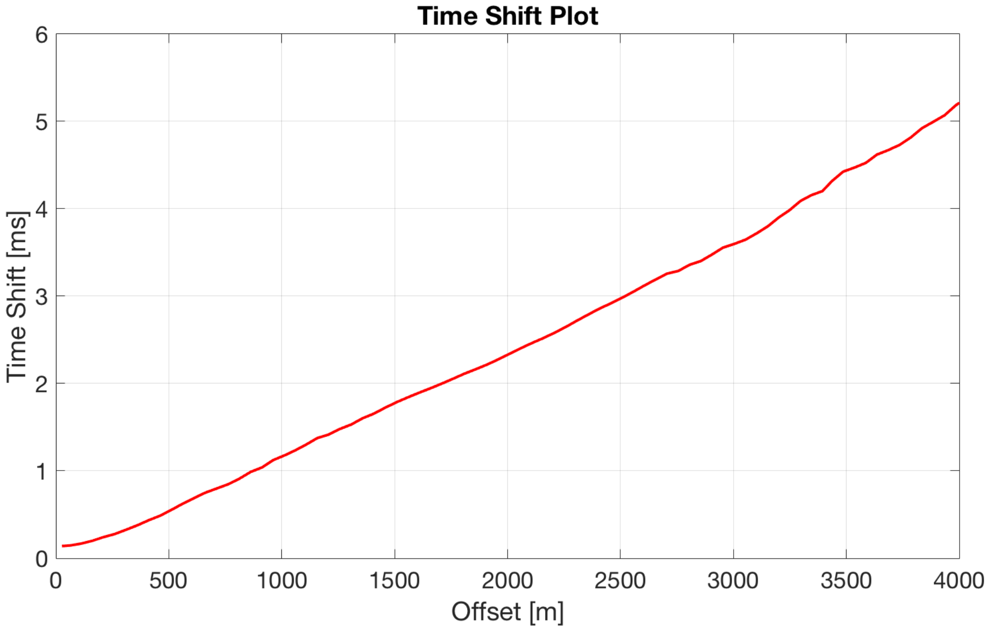

Figure 4.2: Time shift curve showing the direct wave time shift variation with offset for the traces in a common shot gather pair. The curve was made by cross-correlating the direct wave event for all trace pairs in a common shot gather pair, and plot the time shift against offset. The shape of the time shift curve was used as the basis for the inversion to find the water velocity and tidal changes.

As described in Section 2.2, the velocity change and tidal change have a different impact on the time shift magnitude with offset. The velocity changes result in time shifts which increase in magnitude with offset, while the tidal changes result in time shifts which decrease in magnitude with offset. The idea behind the TSCI method is that it should be possible to estimate and separate the water velocity and tidal level changes based on the time shift curves like the one in Figure 4.2.

4.1.2 Source Position Correction

Although the two shot gathers that make up a shot gather pair represent approximately the same source positions, the source inline, crossline and depth positions vary slightly between the PRM 4 and 5 at Snorre. This was seen in Figure 3.3, where the shot positions for Snorre PRM 4 and 5 clearly differed in the crossline direction. The y-axis in Figure 3.3 was very exaggerated in relation to the x-axis. To better visualize the source position differences, Figure 4.3 shows a zoom-in at the shot positions for the common shot gather pair to the far west in PRM 4 and PRM 5, where the axis are equal. As seen in Figure 4.3, there are some differences in the inline direction, but the largest difference is in the crossline direction.

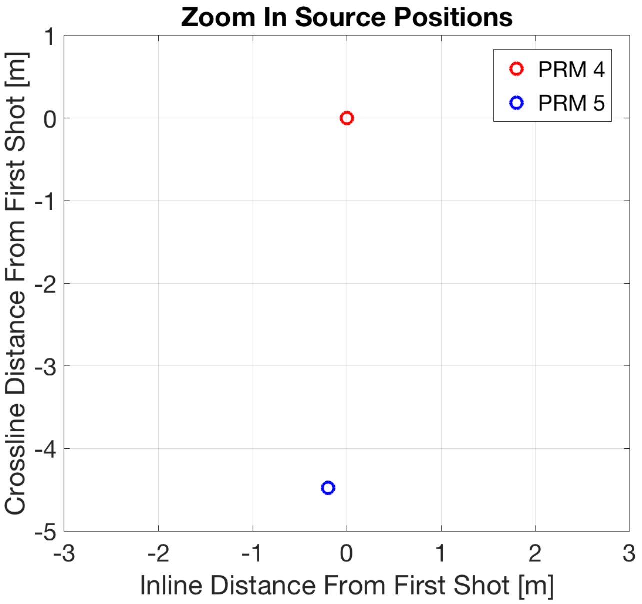

Figure 4.3: Zoom-in at the shot positions of the common shot gather pair located to the far west in PRM 4 and PRM 5. The length of the axes is equal and the figure shows a larger difference in the source crossline position than in the source inline position.

The source position differences cause the magnitude of the time shift between the vintages to increase/ decrease. However, it is the water column induced time shifts that are of importance in this project. Therefore, the time shifts caused by source position differences needed to be corrected for. For this purpose, a time shift correction was performed to the traces before cross-correlation. Since the higher order multiples have propagated with an angle closer to the vertical than the low order multiples for a given offset, the additional time shifts caused by source position differences vary for the different water column events. As a consequence, an individual correction had to be made for each event in each trace pair.

The correction was found by calculating differences in range, i.e. the differences in travelled distance between the source and the receiver. The range was calculated with Equation 4.1 for both vintages. The correction was found by dividing the range difference by an approximate absolute velocity, like the one found by the "Near Offset Method" described in Appendix B.3. Equation 4.2 shows the correction.

$$R = \sqrt{(x_r - x_s)^2 + (y_r - y_s)^2 + ((2n-1)z_r - z_s)^2} \tag{4.1}$$

$$\Delta t_{Cor} = \frac{R_{PRM5} - R_{PRM4}}{v} \tag{4.2}$$

x_s and y_s are the source x and y coordinates, while x_r and y_r are the receiver x and y coordinates. z_s and z_r are the water depth at the source and the receiver respectively. R is the range, R_{PRM5} and R_{PRM4} is the range for PRM 5 and PRM 4 respectively. v is the velocity and Δt_{Cor} is the time shift correction performed to event number n. $n = 1$ is the direct wave, $n = 2$ is the first multiple, and so on.

For each event, the correction was applied to the trace in PRM 5 on the form

$$t_f = t_i - \Delta t_{Cor} \tag{4.3}$$

where t_i represents the traveltime for the event before the correction and t_f represents the traveltime of the event after the correction. The correction in Equation 4.3 shifted the traveltime for the events in PRM 5 to the same traveltime they would have had if the source in PRM 5 was located at the same position as the source in PRM 4.

4.1.3 Symmetry Correction

Even though differences in the given source positions were corrected for as described in Section 4.1.2, there were still some rest differences between the source positions in the two vintages.

The source position is measured by a GPS antenna sitting on buoys floating at the sea surface. The sources, however, are hanging in chains around 6 meters below the buoys. But the chains are not always hanging straight down. Due to drag forces, ocean streams and wave action, the source can be lifted up and pushed backwards and to the sides. When this happens, the measured GPS position will not give the correct position of the source. The issue is illustrated in Figure 4.4 where the GPS measures the correct position for the source to the left, but not for the source to the right, which is pushed out of position.

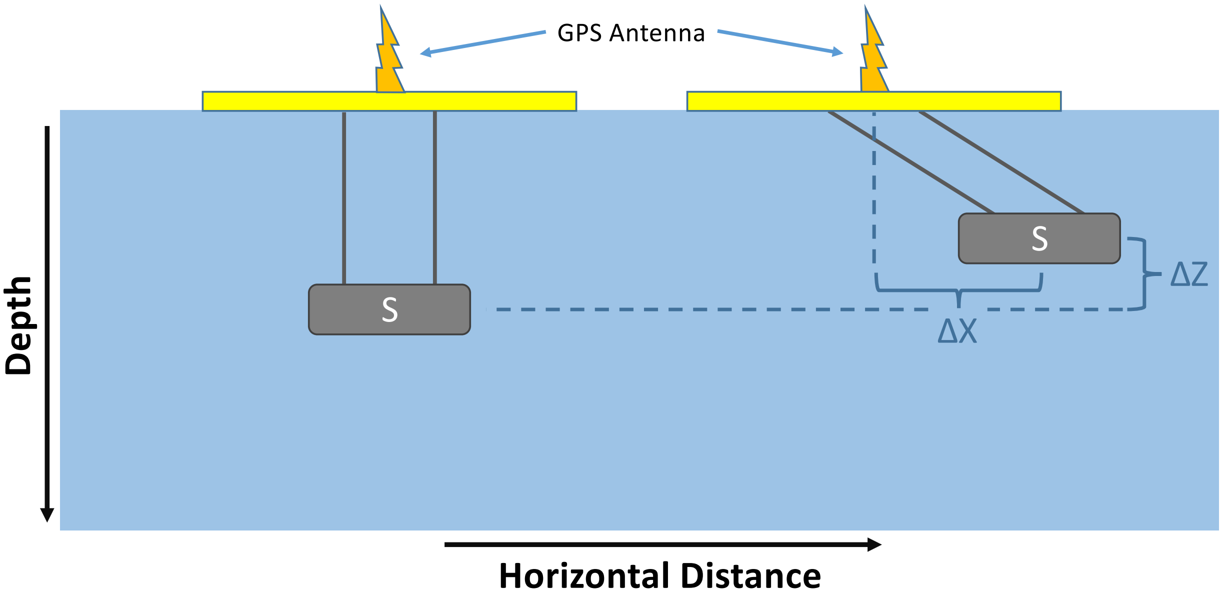

Figure 4.4: Illustration of the GPS source position error. The gray cylinders, "S", illustrates the source, while the yellow rectangles illustrate the buoys floating at the water surface. The orange peaks at the top of the bouys are the GPS antennas. The source to the left is in correct position, but the source to the right is shifted with Δx in the horizontal direction and Δz in depth direction.

The uncertainty in the GPS source position exists for both vintages included in the TSCI method. The problem caused by the source differences is illustrated in Figure 4.5, which shows a water layer with different source positions for two vintages, Vintage 1 and 2. The green source illustrates the source position for Vintage 1, while the red sources represent different scenarios of source positions for Vintage 2, located at different inline distances from the green source. According to the GPS measurements, the sources are located at the same position for all scenarios. Since there is no measure of the source position difference, the difference can't be corrected for by the source position correction described in Section 4.1.2.

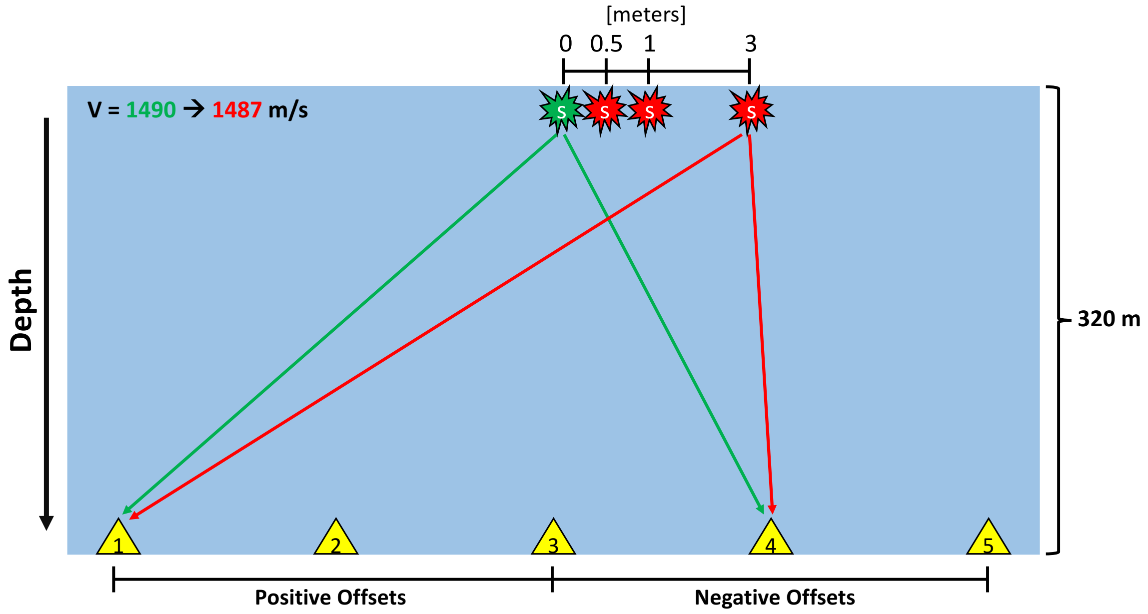

Figure 4.5: Figure illustrates the problem with source inline position differences. The green source represents Vintage 1, while the red sources represent different scenarios for Vintage 2. The green rays illustrate the waves emitted from the green source, while the red rays illustrate waves emitted from the red source. The yellow triangles illustrate the sea bottom receivers. The receivers to the left of the green source (receiver 1 and 2) are located at positive offsets, while the receivers to the right of the green source (receiver 4 and 5) are located at negative offsets. For positive offsets, the travelled distance for the red rays increases compared to the green rays as the source position difference increases. For negative offsets, the travelled distance reduces for the red rays compared to the green rays. The model was used for a test where the velocity decreased from 1490 m/s in Vintage 1 to 1487 m/s in Vintage 2. The water depth was 320 meters. Offsets up to 2000 meters were included for positive and negative offsets, with a receiver spacing of 100 meters.

To investigate what effect the differences in the source position have on the resulting time shift curves, a test was performed. The test was based on the model and source differences in Figure 4.5. The only thing that varied between the two vintages except for the source positions, was the water velocity. Vintage 1 had a water velocity of 1490 m/s, while Vintage 2 had a water velocity of 1487 m/s. The time shifts between the two vintages were calculated with the help of a 1D raytracing model (described later in Section 4.1.5). This was done 4 times, with a gradual increase in source inline position difference from 0 to 3 meters, as illustrated in Figure 4.5. The resulting direct wave time shifts for positive and negative offsets are shown in Figure 4.6.

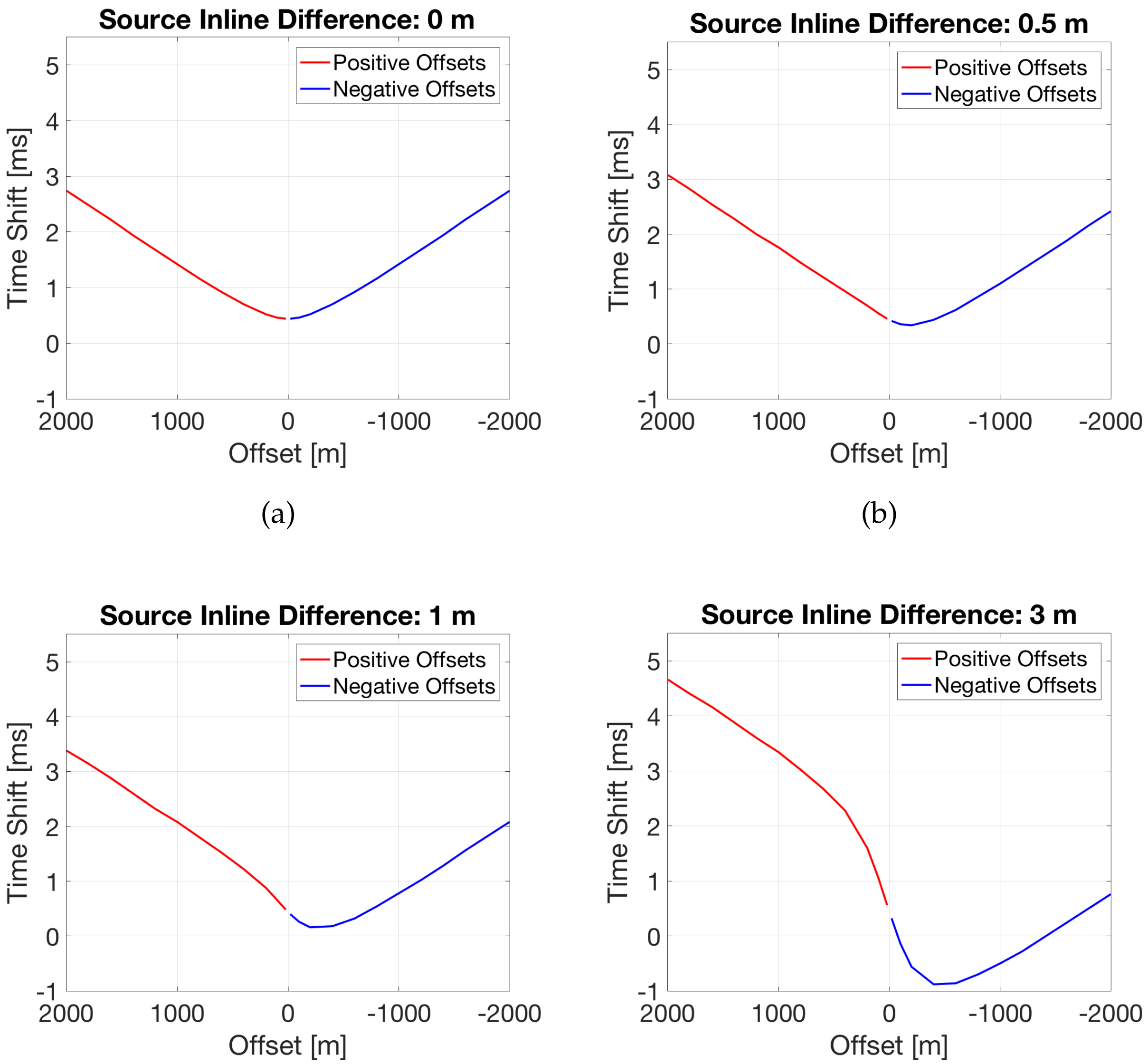

(a) (b)

(c) (d)

Figure 4.6: Results of the test of source inline position differences. The test is illustrated in Figure 4.5. The plots show direct wave time shift curves for positive (blue) and negative (red) offsets for source inline position differences of (a) 0 m, (b) 0.5 m, (c) 1 m and (d) 3 m. Note the change in the shape and unsymmetrical behavior of the time shift curves as the source inline difference increases.

Figure 4.6 (a) shows the time shifts as the sources in both vintages are located at the same position. The time shifts for positive and negative offsets are symmetrical around 0-offset. As the source inline difference increases from (b) to (d), the time shifts for positive offsets increases compared to the time shifts for negative offsets, which decreases. The minimum of the time shift curves is also pushed towards negative offsets, and the time shift curves for positive and negative offsets becomes more and more unsymmetrical around 0-offset. The additional time shifts created by the source inline differences are largest for large offsets where the waves have travelled more in the inline direction and the difference between the source positions is most pronounced.

The unsymmetrical time shift curves in Figure 4.6 are caused by the differences in travelled distance which occurs as the sources are located at different positions. This is illustrated in Figure 4.5. The green rays travel with a velocity of 1490 m/s, while the red rays travel with a velocity of 1487 m/s. Hence, for a given travel distance the traveltimes for the red rays are larger than the traveltimes for the green rays. As the red source moves towards negative offsets, the distance to receiver 1, 2 and 3, increases in comparison to the green source. This increases the traveltime for the red ray so the traveltime difference between the vintages increases for positive offsets. However, the distance from the red source to receiver 4 and 5 reduces in comparison to the green source. Hence, the traveltime difference reduces for negative offsets, as the slow red ray travels a shorter way than the fast green ray.

The same test as described for the source inline differences were done for source differences in the crossline direction and depth direction as well. Figure 4.7 illustrates the test for the source depth differences, where the source in Vintage 2 has moved upwards relative to the source in Vintage 1. No figure was added to illustrate the test of the source position difference in the crossline direction. The results of the test of source position differences in the crossline and depth directions are shown in Figure 4.8, where (c) and (d) shows the time shift curves for the test shown in Figure 4.7.

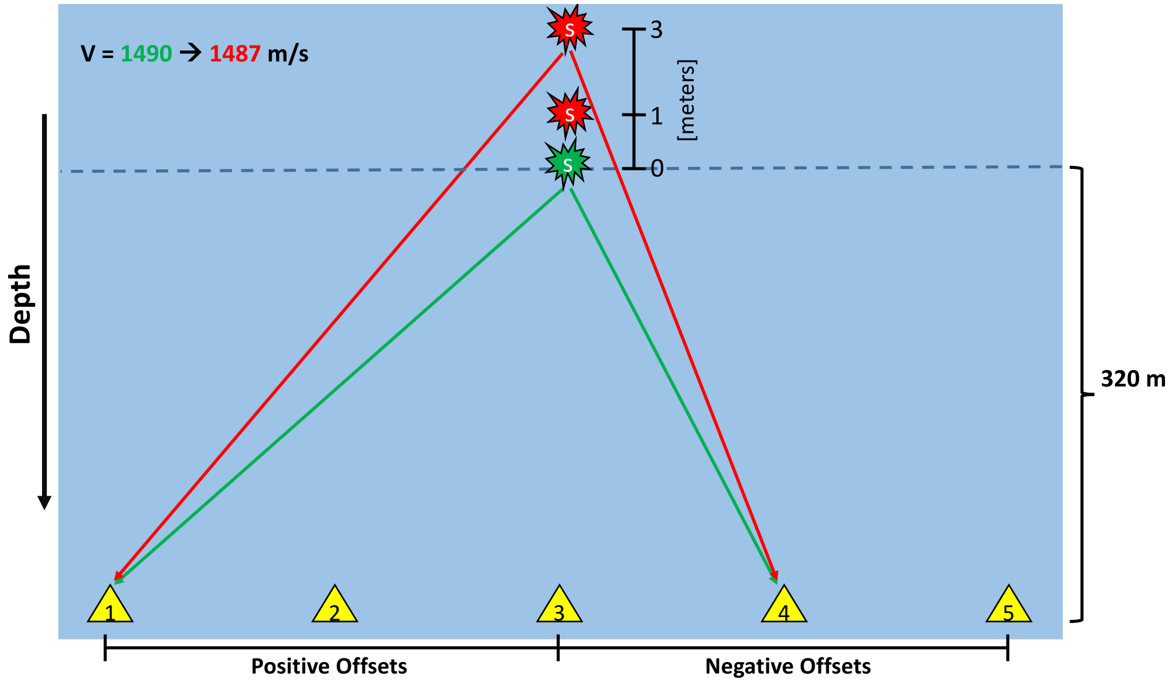

Figure 4.7: Figure illustrates the test of the source depth differences. The green source represents Vintage 1, while the red sources represent different scenarios for Vintage 2, where the source has moved upwards 1 and 3 meters compared to Vintage 1. The water depth at the source in Vintage 1 was 320 meters. The green and red rays correspond to ray paths for the waves in Vintage 1 and Vintage 2 respectively. The velocity decreases from 1490 m/s in Vintage 1 to 1487 m/s in Vintage 2. The yellow triangles illustrate the sea bottom receivers. The receivers to the left of the green source (receiver 1 and 2) are located at positive offsets, while the receivers to the right of the green source (receiver 4 and 5) are located at negative offsets. Offsets up to 2000 meters were included for positive and negative offsets, with a receiver spacing of 100 meters. Note that the difference in the travelled distance between the green and red rays is largest for short offsets and reduces for larger offsets.

No difference can be seen between Figure 4.8 (a) and (b). Hence, the effect of a 3 meter source crossline difference seems to be negligible. The effect of source depth differences in Figure 4.8 (c) and (d) are larger. It is clear that the source depth difference creates additional time shifts that are symmetrical around 0-offset and largest at short offsets. Since the source depth difference is a vertical change, it is most pronounced at short offsets where the vertical proportion of the waves' travel path is largest. As the offsets increases, the waves travel with angles closer to the horizontal and the relative difference in travelled distance created by source position difference reduces. This is illustrated in Figure 4.7, where the difference between the red and the green ray is larger for the rays that hit receiver 4 than the rays that hit receiver 1. This is the reason why the magnitude of the time shifts created by the source depth differences reduces with offset. If the source in Vintage 2 had moved down instead of up, the source difference would have resulted in reduced instead on increased time shifts at short offsets.

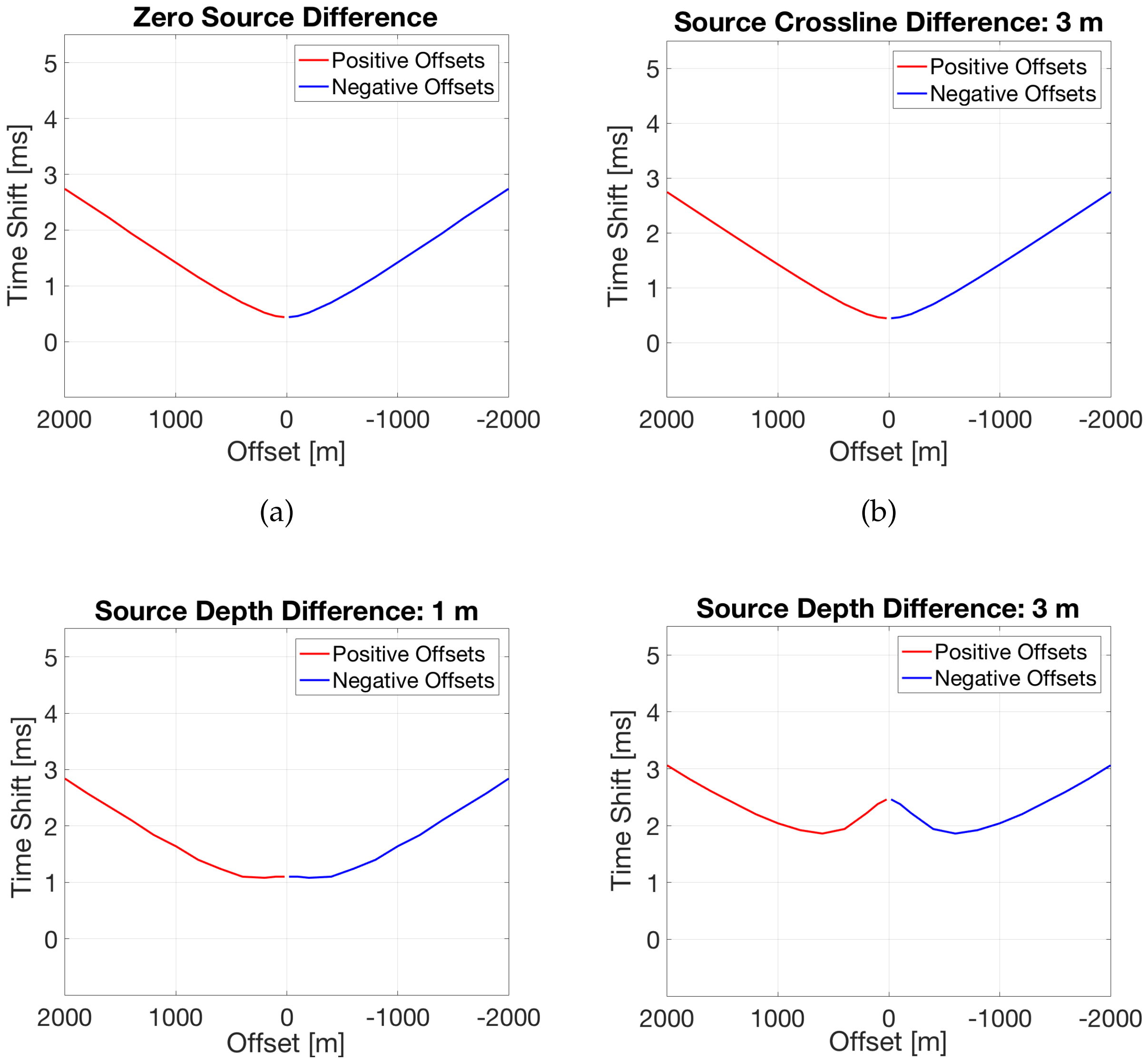

(a) (b) (c) (d)

Figure 4.8: Results of the test of source position differences in the crossline and depth directions. (a) shows the time shift curves for sources located at the same position, the same as Figure 4.6 (a). (b) shows the time shift curves as the source in the Vintage 2 has moved 3 meters in crossline direction relative to the source in the Vintage 1. (c) and (d) shows the time shift curves as the source in Vintage 2 has moved upwards by 1 and 3 meters respectively, as illustrated in Figure 4.7.

Performing the Symmetry Correction

To summarize the observations from the test results in Figure 4.6 and Figure 4.8, the source inline differences create largest time shifts for large offsets and results in unsymmetrical time shift curves. The source depth differences produce symmetrical time shifts up/down, which are largest for short offsets. Since the time shift curves are the basis for the inversion process of finding the water velocity and tidal changes, the additional time shifts created by the source position differences will affect the velocity and tidal change estimates negatively and need to be corrected for.

For the velocity and tidal changes estimated at positive and negative offsets to be consistent, the time shift curves need to be symmetrical around zero offset. Because of this, the source position correction was focused on correcting for the source inline differences, and to make the time shift curves symmetrical. The correction was given the name "Symmetry Correction". The source depth differences were assumed to be small, so no correction was made for the source depth differences, even though potential depth differences create significant time shift artifacts as shown in Figure 4.8.

Since the currents, drag forces and waves vary throughout the acquisition of both vintages included in the TSCI method, the symmetry correction had to be made for each shot separately. It is not known exactly how much the sources in the two vintages had moved relative to each other, so the symmetry correction was performed to only one of the vintages. For each shot, the source position for PRM 5 was corrected to the same source position as in PRM 4. The source position for PRM 4 might be more incorrect than the one for PRM 5. However, the correction makes sure the two get shifted to the same point.

The magnitude and direction of the source inline correction, Δx, was found by optimization. In this report, "positive offsets" are defined as the offsets corresponding to the receivers to the west of the source position. "Negative offsets" are defined as the offsets corresponding the receivers to the east of the source position. For each common shot gather pair, the time shift curves for positive and negative offsets were forced to be symmetrical around zero range by adjusting the source inline coordinate for PRM 5. The Δx which minimized the difference between positive and negative offsets was chosen. The objective function was defined as the difference between the time shifts for positive and negative offsets and the L1 norm was used. The objective function that was minimized can be expressed as

$$\phi(\Delta x) = \sum_{r=0}^{R_m} W_r |P_r(\Delta x) - N_r(\Delta x)| \tag{4.4}$$

where r is the range, R_m is the maximum range and P_r and N_r are the time shifts for positive and negative offsets respectively at range r. W_r is the weight at range r, which was adjusted to optimize the symmetry correction by giving the high quality parts of the time shift curves higher weights. R_m was sat to 3000 meters. If the maximum range for positive/ negative offsets was lower than 3000 meters, the R_m was sat to the lowest maximum range of the two. To find the global minimum of the objective function in Equation 4.4, the built-in "Global Search Algorithm" in MatLab was used, described in Section 2.6.

The assumption behind this symmetry correction was that the velocity not changes laterally, only vertically, so that the waves for positive and negative offsets with the same absolute value, propagates with exactly the same velocity.

Figure 4.9 shows the direct wave time shift curves for positive and negative offsets for a shot gather from the Snorre data before and after the symmetry correction. Large improvement in symmetry can be seen after the correction. The difference between the time shifts for positive and negative offsets clearly reduces and the "up-dip" at small positive offsets gets straightened out after the symmetry correction.

In this report the shot numbers are defined from 1 to 566, representing the common shot gather pairs in the Snorre data. Shot number 1 is the common shot gather pair located to the far west, while shot number 566 is the common shot gather pair located to the far east. To perform the symmetry correction, it was necessary to have enough traces at both sides of the shot point, both at positive and negative offsets. By inspection of how the quality of the symmetry correction varied with the number of traces included, a minimum limit was sat to 33 receivers. All shots needed to have at least 33 receivers (1650 meters offset) at each side, in order to get a good quality symmetry correction. The shot numbers that satisfied this requirement was shot number 120 to 454. The common shot gather pairs located at the flanks of the shot line, with less than 33 receivers at positive or negative offsets, did not result in sufficient symmetry correction. Therefore, shot number 0-120 and 455-566 were removed from the dataset before the calculations of the water column changes.

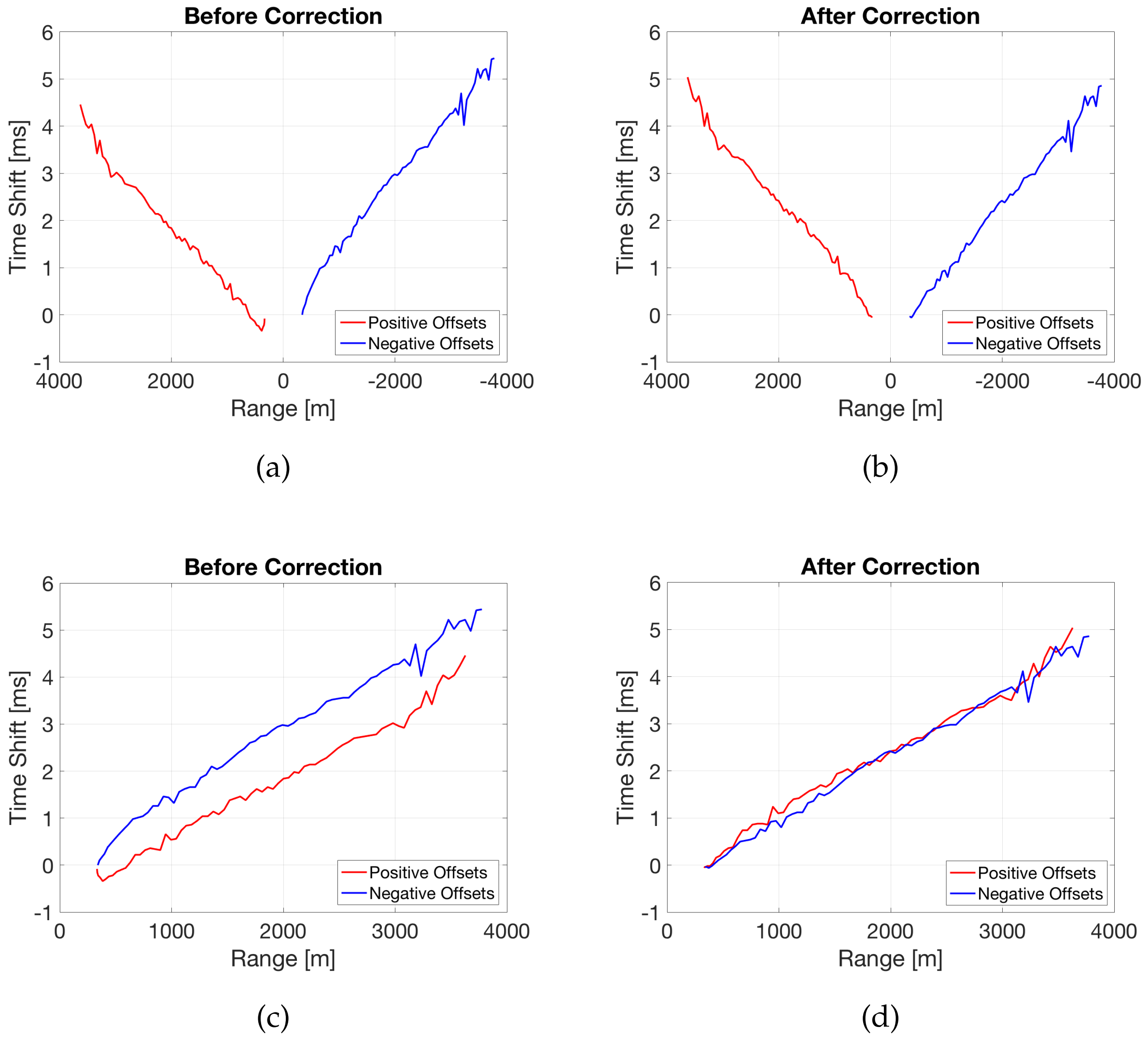

(a) (b)

(c) (d)

Figure 4.9: Time shift curves for positive (red) and negative (blue) offsets before symmetry correction in (a) and (c), and after symmetry correction in (b) and (d). (a) and (b) shows the time shifts plotted for positive and negative range and illustrates the symmetry of the curves. (c) and (d) shows the time shift curves plotted for the absolute value of the range to enhance the visibility of the differences between the two. Note the improvement in symmetry and similarity of the time shift curves at positive and negative offsets after the symmetry correction.

4.1.4 Removal of Outliers

Due to noise and interference with surrounding signal did not all the calculated time shifts correspond to actual water column induced time shifts between the vintages. The time shift curves contained spikes and outliers, i.e. unrealistic high/ low time shifts, which needed to be removed. The outlier removal and smoothing method used in this project is described in Appendix B.4.

4.1.5 Forward Modelling with 1D Raytracing Model

After the source position corrections and outlier removal of the time shift curves, inversion was used to find the water velocity and tidal changes between the vintages. The background model used to calculate the forward response during the inversion, was a 1D raytracing model consisting of a single water layer with a flat sea bottom. The way the raytracing model works is described in the following.

For each shot number (common shot gather pair), the source and receiver positions for Snorre PRM 4 were inserted into the raytracing model. For each receiver, r, 2 different arrival times were calculated with Equation 4.5 and 4.6.

$$t_{1,n,r_i} = \sqrt{\frac{(x_{r_i} - x_s)^2 + (y_{r_i} - y_s)^2 + ((2n-1)z_{r_i} - z_s)^2}{v^2}} \tag{4.5}$$

$$t_{2,n,r_i} = \sqrt{\frac{(x_{r_i} - x_s)^2 + (y_{r_i} - y_s)^2 + ((2n-1)(z_{r_i} + \Delta z) - z_s)^2}{(v + \Delta v)^2}} + \Delta SOD \tag{4.6}$$

t_{1,n,r_i} and t_{2,n,r_i} are the two arrival times at receiver r_i, for event number n. $n = 1$ represents the direct wave, $n = 2$ represents the 1^{st} order multiple, and so on. v is an approximate absolute water velocity for PRM 4, like the one estimated with the "Near Offset Method" described in Appendix B.3. x_s and y_s are the source x and y coordinates, while x_{r_i} and y_{r_i} are the x and y coordinates for receiver r_i. z_s is the source water depth, while z_{r_i} is the average water depth of all the receivers between the shot position and receiver r_i. The average water depth was used because the multiples have been reflected several times between the source and the receiver. Therefore, an average receiver water depth gave a more correct water depth for the multiples. However, the water depth for the direct wave became slightly wrong, but, as discussed later in Section 6.2, this should not have any large affect on the final results. All the source and receiver position inputs corresponded to the source and receiver positions in Snorre PRM 4. The two calculated arrival times in Equation 4.5 and 4.6 were only differing in velocity by Δv, tidal level by Δz and start of data delay by ΔSOD. Start of data delay (SOD) is caused by a lag in time between the measured firing time and the actual firing time in the source. The SOD is unknown and varies for the different vintages.

Since the sea bottom in the 1D raytracing model was totally flat, there was no need for calculating the sea floor reflection angles, as they stayed the same as the incidence angle.

The arrival times in Equation 4.5 and 4.6 were calculated for all the receiver positions, resulting in two sets of arrival times for each event number n, for each shot number. The two sets of arrival times are given as $t_{1,n}$ and $t_{2,n}$ below

$$t_{1,n} = t_{1,n,r_1}, t_{1,n,r_2}, t_{1,n,r_3}, ..., t_{1,n,r_N} \tag{4.7}$$

$$t_{2,n} = t_{2,n,r_1}, t_{2,n,r_2}, t_{2,n,r_3}, ..., t_{2,n,r_N} \tag{4.8}$$

where $r_1, r_2, r_3, ..., r_N$ represent the different receivers. For each water column event, synthetic time shifts were made by subtracting the two sets of arrival times in Equation 4.7 and 4.8, as shown in Equation 4.9. The result was a synthetic time shift series for each water column event, S_n, representing the synthetic time shifts at the different offsets/ receiver positions.

$$S_n = t_{2,n} - t_{1,n} \tag{4.9}$$

The way the raytrace model was used to estimate the two sets of arrival times is illustrated in Figure 4.10. (a) and (b) only differs in water depth, water velocity, and SOD. For each receiver, highlighted by the yellow triangles numbered from 1 to n, the corresponding arrival time was calculated for the different water column events with Equation 4.5 in (a) and Equation 4.6 in (b). The time shifts for the different water column events were then found by Equation 4.9. An example of a synthetic time shift curve made with the 1D raytracing model is shown in Figure 4.11.

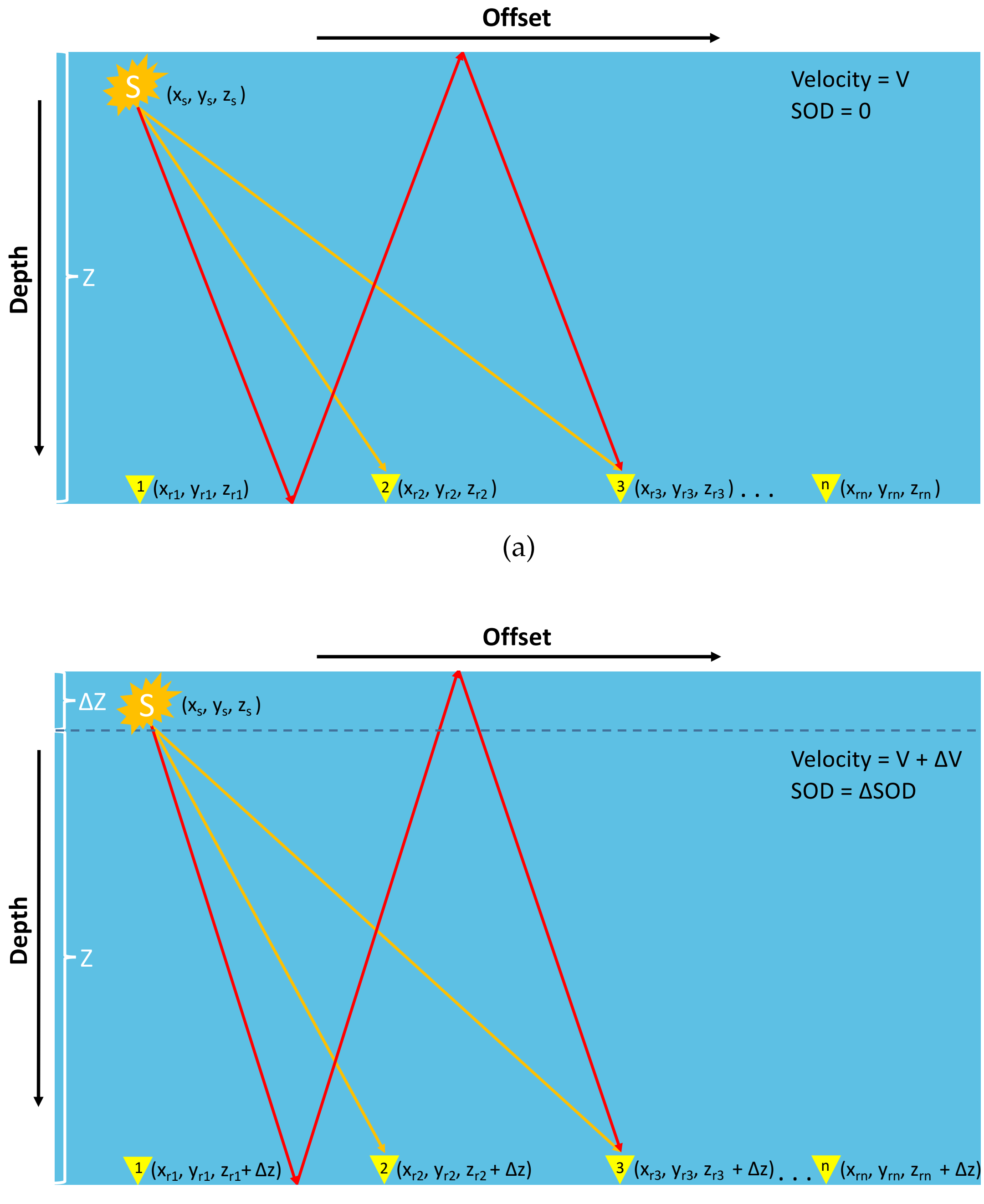

(a)

(b)

Figure 4.10: Illustration of raytracing model used to calculate the synthetic time shifts. (a) and (b) are differing in velocity by Δv, tidal level by Δz and start of data delay by ΔSOD. The "S" highlights the source position and the yellow triangles highlight the receivers. The parenthesis represent the source and receiver coordinates. The receiver depth used was the average of the actual receiver water depths between the source position and the receiver position, and varied hence for each receiver. For the Snorre data, (a) represents PRM 4, while (b) represents PRM 5. The arrival times in (a) are calculated with Equation 4.5, while the arrival times in (b) are calculated by Equation 4.6. The time shifts between the models are calculated with Equation 4.9. The orange rays illustrates direct waves, while the red rays illustrates a 1st order multiple.

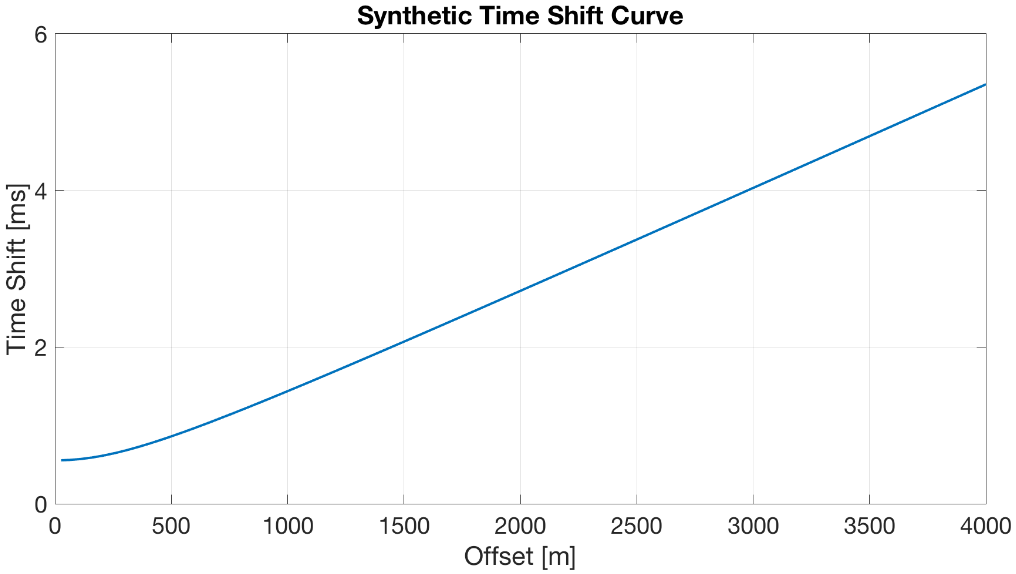

Figure 4.11: Example of a synthetic time shift curve for the direct wave made with the 1D raytracing model. The time shifts correspond to the changes: Δv = -2.75 m/s, Δz = 0.196 meters and ΔSOD = 0.00018 s

Arrival Time Prediction

As mentioned in Section 4.1.1, the 1D raytracing model was used for predicting the arrival times for the water column events in the Snorre data before the cross-correlation. For this purpose, Equation 4.5 was used with the same input parameters as listed above.

4.1.6 Inversion Based on Time Shift Curves

A synthetic time shift curve is shown together with a measured time shift curve in Figure 4.12 as the blue and the red curves respectively. The green arrows illustrate the goal of the inversion process, which is to find the change in velocity, tides, and SOD that minimizes the difference between the synthetic and measured time shift curves.

Figure 4.12 shows the time shifts for only one event. However, the time shifts for several water column events were included in the inversion. For each shot number, the minimum found by the inversion corresponded to the change in velocity, tides and SOD resulting in the synthetic time shift curves with the best overall match with the measured time shift curves of the included events. For illustration, the measured time shifts together with the final synthetic time shifts are shown in Figure 4.13 for the direct wave (a), first multiple (b) and second multiple (c). Note that individually the synthetic blue curves do not match the measured curves perfectly. However, the synthetic curves represent the velocity change, the tidal change and the SOD change with the best overall fit to all the 3 measured time shift curves.

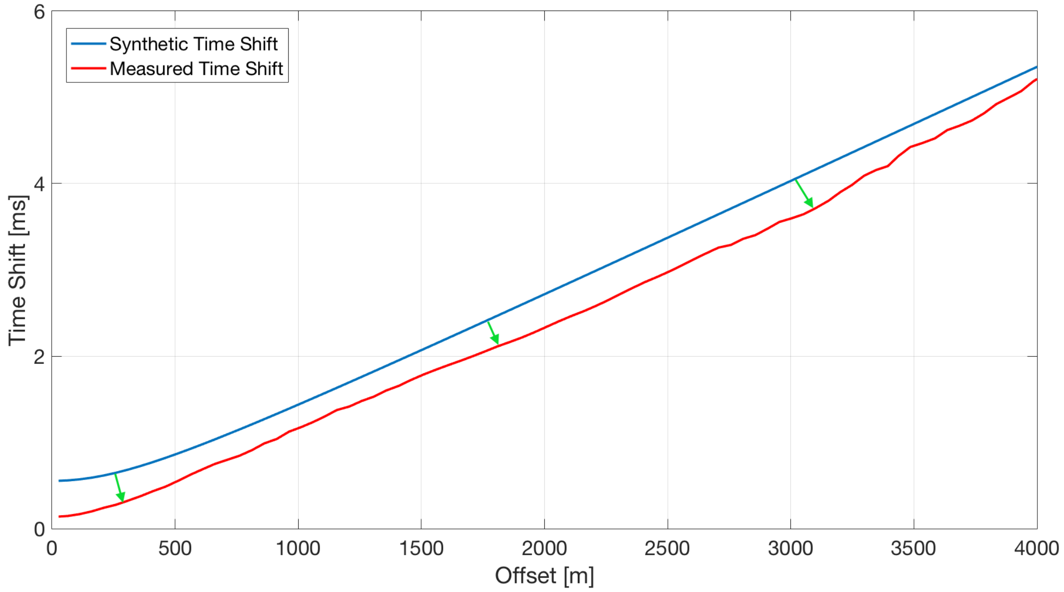

Figure 4.12: The red curve represents the measured time shifts of the direct wave, while the blue curve is the synthetic time shifts of the direct wave, corresponding to a specific Δv, Δz and ΔSOD. The green arrows indicate the goal of the inversion process, which is to find the Δv, Δz and ΔSOD that minimizes the difference between the measured and synthetic time shifts.

Measured time shift curves of high quality increase/ decrease smoothly and gentle with offset. However, as seen in Figure 4.13, the quality of the measured time shifts varies with offset for the different events. The quality of the direct wave in (a) is good for short offsets, but reduces for large offsets. The second multiple in (c) has better quality for large than for short offsets. To get best possible estimates of the water column changes, only the offset intervals with high quality of the time shift curves were included in the objective function. The different events and different offset segments were also delegated different weightings in the objective function. The offset intervals where the measured time shift curves had the best quality was weighted more heavily than the more noisy offset intervals.

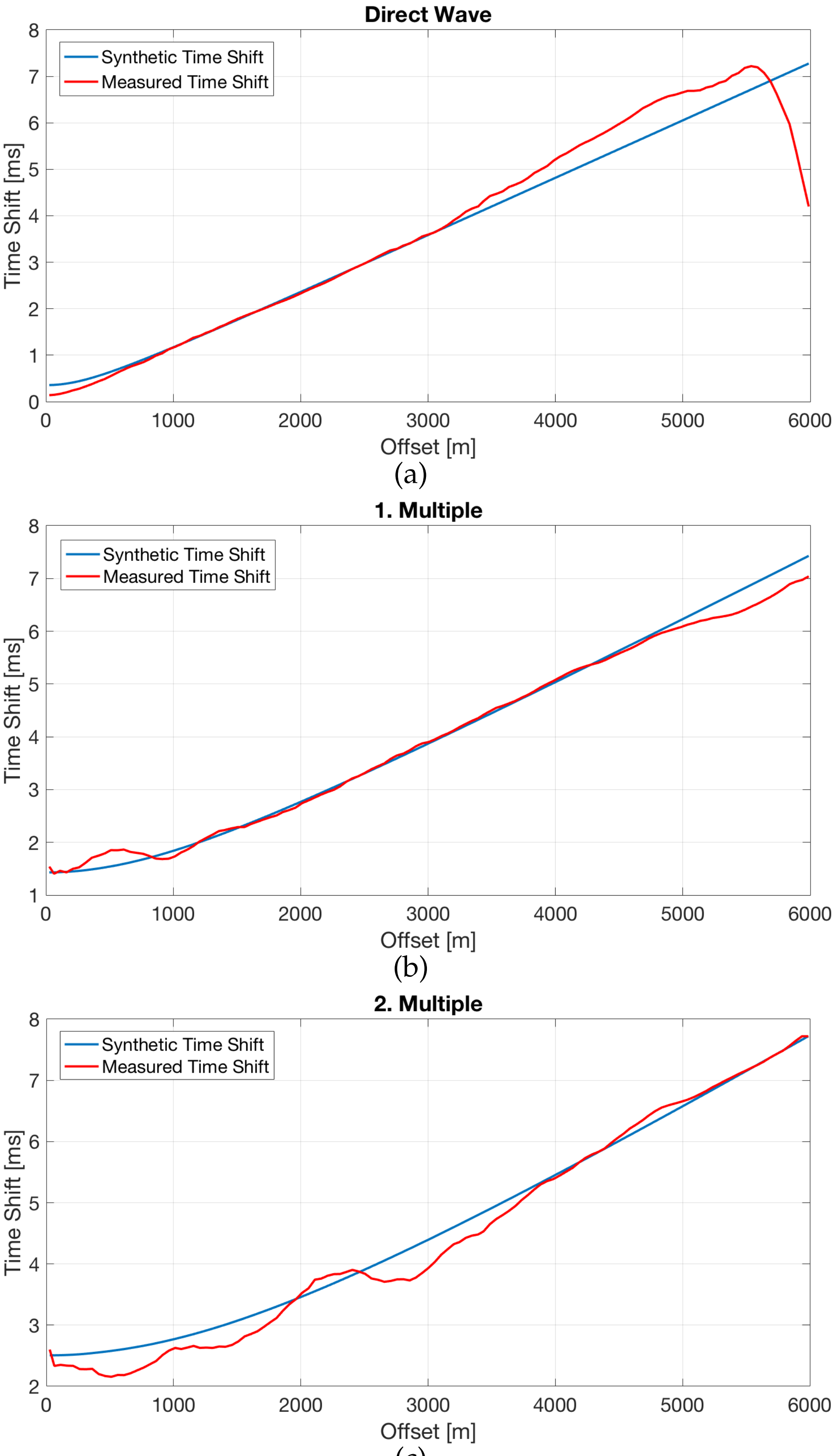

(a)

(b)

(c)

Figure 4.13: Figures shows resulting synthetic time shifts after inversion (blue), together with the measured time shifts (red) for the direct wave (a), 1st multiple (b) and 2nd multiple (c). Note that the synthetic blue curves individually not match the measured time shift curves perfectly. However, the synthetic curves represent the velocity change, the tidal change and the SOD change that together gives the best fit with all the 3 measured time shift curves. Note the variation in quality of the time shift curves for the different events.

The norm used for the objective function was the L1 norm. By letting $M_{n,x}$ be the measured time shifts from the common shot gather pair (described in Section 4.1.1) and $S_{n,x}$ be the forward modelled time shifts made by the raytracing model (described in Section 4.1.5) at offset, x, and event number, n. The objective function, ϕ, that was minimized during the inversion can be expressed as

$$\phi(\Delta z, \Delta v, \Delta SOD) = \sum_{n=1}^{N} \sum_{x=L_n}^{H_n} W_{n,x} |M_{n,x} - S_{n,x}(\Delta z, \Delta v, \Delta SOD)| \tag{4.10}$$

$n = 1$ represents the direct wave, $n = 2$ represents the 1^{st} multiple and so on. N is the highest multiple order included in the calculations. L_n and H_n is the minimum and maximum offset included respectively for event number n. $W_{n,x}$ is the weight given to event number n at offset x. Δz, Δv and ΔSOD are the changes in tidal level, water velocity and start of data delay respectively. The model misfit, ϕ_m in Equation 2.13, was sat to 0 so the objective function became equal to the data misfit function. The built-in Global Search Algorithm in MatLab, described in Section 2.6, was used to find the global minimum of Equation 4.10.

A flow chart for the inversion process is shown in Figure 4.14, where the direct wave, first and second multiple are included. The biggest loop represents the shot number. For each shot, the inner loop runs the inversion to find the change in velocity, tides and SOD. The synthetic time shifts are calculated for the direct wave, first and second order multiple and the value of the objective function is calculated. The process goes on until the global minimum is found. Since this process is done for each shot, each shot results in one estimate for the velocity change, tidal change and SOD change.

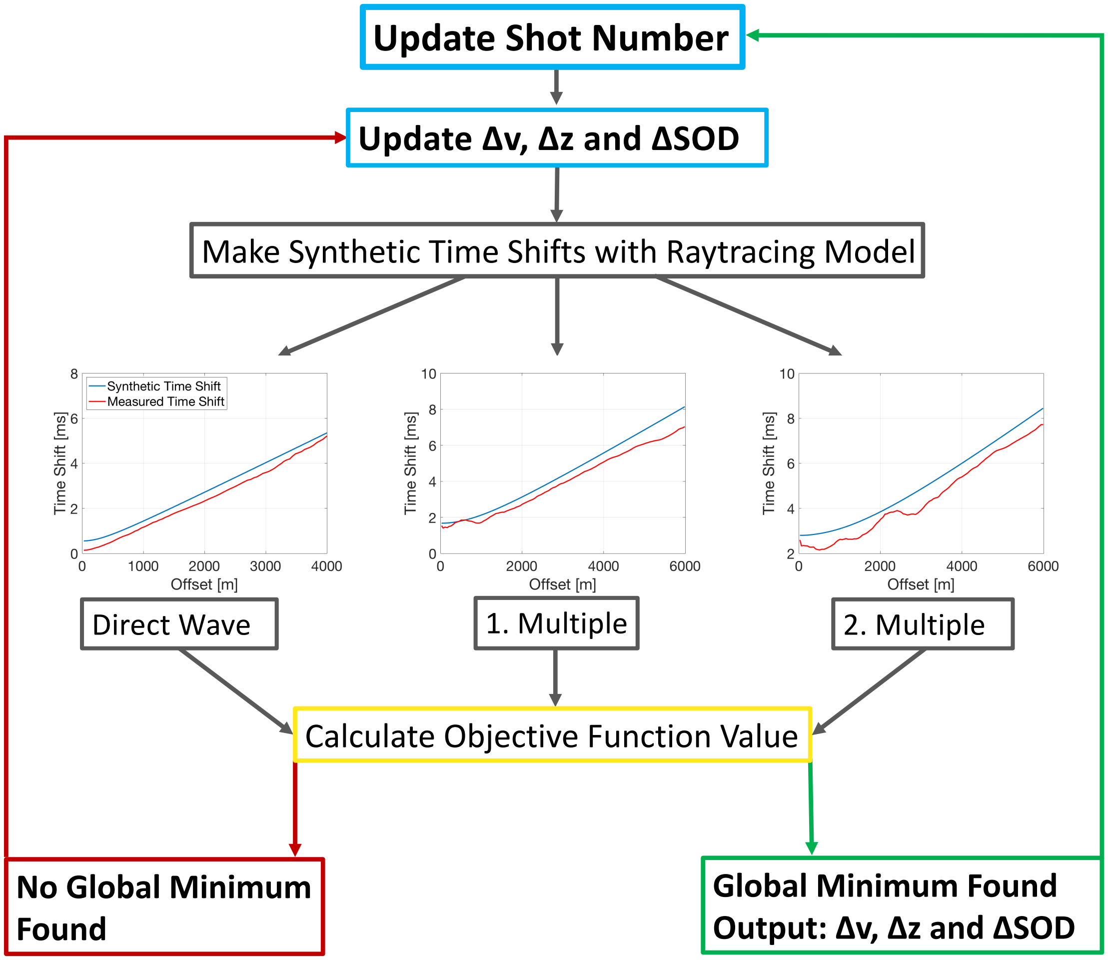

Figure 4.14: Simplified chart for the inversion process. For each shot number synthetic time shifts corresponding to a Δv, Δz and ΔSOD is made and the value of the objective function is calculated. Δv, Δz and ΔSOD is updated and the inversion process goes on until the global minimum is found. The process is repeated for each shot number included in the calculations. This chart only represents the main idea with the inversion, not how Global Search Algorithm finds the global minimum.

4.1.7 Offset Intervals of the Time Shift Curves

The estimates of the velocity change and the tidal change is decided by the shape of the time shift curve. However, the water velocity and tidal change dominate the time shift curve at different offset intervals. This is illustrated in Figure 4.15, where time shift curves corresponding to 3 different velocity changes are shown in (a). The curves are pretty similar and are difficult to separate at short offsets, and one can be mistaken with another as the data gets noisy. At large offsets, the curves separate much better, and even if noise is present, it should be possible to separate the time shift curves. Hence, to obtain precise estimates of the water velocity changes, it is important to include large offsets in the objective function in Equation 4.10.

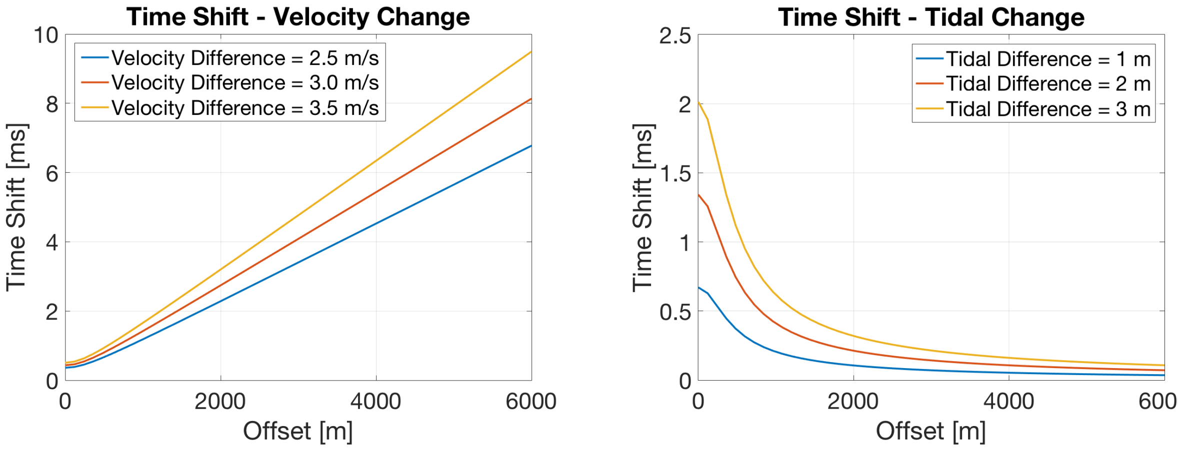

(a) (b)

Figure 4.15: Figure shows synthetic time shift curves caused by 3 different velocity changes in (a) and 3 different tidal changes in (b). Time shifts caused by velocity changes increases with offset, while time shifts caused by tidal changes decreases with offset. The time shift curves were made with the raytracing model described in Section 4.1.5.

Figure 4.15 (b) shows time shift curves corresponding to 3 different tidal changes. The magnitude of the time shifts reduces quickly with offset. This is because the tidal change is a vertical change and will be most pronounced for waves traveling vertically. Because of this, it is important to include short offsets in the objective function in Equation 4.10 to get precise estimates of the tidal changes.

The water layer multiples have propagated several times in the water layer and been largely exposed to the changes in the water column. Multiples are especially important for estimation of tidal change, but will also improve the estimates of the water velocity changes.

4.1.8 Strength Factors of the Water Column Events

As observed in Figure 4.13, the quality of the time shift curves varies with offset. This is due to variation in the strength of the signal. Due to the source ghost, reflection coefficient variations with offset, and interference with surrounding signal, the strength of the events varies with offset. This can be seen by investigating the shot gather in Figure 4.16. The direct wave is strong and clear at short offsets, but as the offset increases, the direct wave gradually gets weaker. This is due to the source ghost. As the offset increases, the relative difference in travelled distance between the direct event and the source ghost reduces. The direct wave and the source ghost have opposite polarities and will interfere destructively, resulting in a gradual attenuation of the direct wave event. As seen in Figure 4.16, it is not possible to observe the direct wave for offsets larger than 4000 meters.

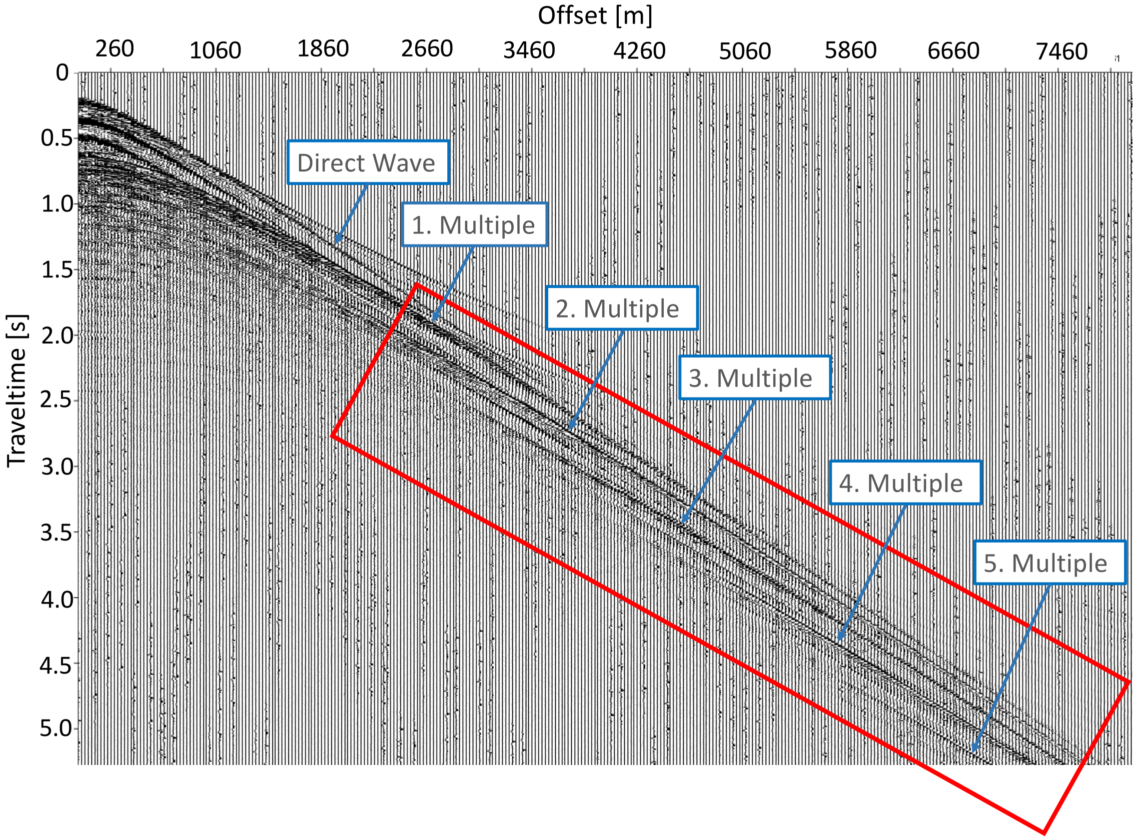

Figure 4.16: Shot gather from Snorre PRM 5. The direct wave amplitude reduces for large offsets due to destructive interference with the source ghost. Each water column event has a specific offset interval of high amplitudes, shown inside the red rectangle. The higher order multiples get their "high amplitude zone" for larger offsets. Note the presence of some refracted waves which will disturb the time shift curves.

Each multiple in Figure 4.16 have a specific offset interval of high amplitudes. This is highlighted by the red rectangle, where the 1st-5th multiple are present. The water layer events measured in the receiver are combinations of the down-going incidence wave and the up-going reflection. Since the data used in this project was the pressure data, the up-going and down-going wave had the same polarity and interfered constructively to a larger amplitude. For pre-critical offsets, the reflection coefficient and the amount of up-going energy will be low. As a consequence, the multiples will loose energy for each reflection at the sea bottom. As the offset increases, the multiples reaches critical angle and the reflection coefficient becomes close to 1. Most of the energy will be reflected at the sea bottom, and less energy gets transmitted to deeper layers. Hence, the water column events preserve more of their energy and get large amplitudes compared to the surrounding signal. As the offset continue to increase, the relative difference between the multiples and the source ghost reduces and the amplitude of the event weakens due to destructive interference. For a given offset, the high order multiples have incidence angles closer to vertical than the low order multiples. Hence, the high order multiples reach critical angle for larger offsets than the low order multiples. Because of this, each multiple is strong in a separate offset interval, between critical offset for that multiple and the offset where the source ghost and the multiple starts to interfere destructively.

To put a number on the strength of the events a "strength factor" was introduced. The strength factor was defined as the amplitude of the water column event divided by the maximum amplitude of the surrounding signal within a window of 100 ms around the event. If the amplitude of the event is the strongest inside the window, the strength factor became 1. This is a way to quantify the strength of the event compared to the surrounding signal.

Strength factors for the direct wave along with the 1st, 2nd and 3rd multiple are plotted in Figure 4.17. The direct wave in (a) is strong up to an offset of 3000-4000 meters, where the strength factor reduces significantly. This is the same observation as made for the direct wave in Figure 4.16. The 1st multiple in Figure 4.17 (b) remain stronger for a longer offset window than the direct wave due to later attenuation by the source ghost. The reason for the little dip in strength factor for offsets between 900 and 1900 meters is probably caused by energy loss during sea bottom reflections before the 1st multiple reaches critical angle at ≈ 1900 meters. The 2nd multiple in (c) reaches critical angle for even larger offsets and the strength factor becomes 1 as the offset exceeds 3200 meters. The strength factor for the 3rd multiple in (d) reaches large values for offsets above 6000 meters.

For the cross-correlation to work optimally and extract the correct time shifts, the amplitude of the event that is to be cross-correlated need to be larger than the surrounding signal. Hence, the zones with strength factor equal 1 are good zones for performing the cross-correlation. Figure 4.18 shows the time shift curves for the direct wave and the 3 first multiples. By comparing these time shift curves with the corresponding strength factor plots in Figure 4.17, it is clear that the high-quality parts of the time shift curves correspond well with the offset intervals of high strength factors. During the inversion described in Section 4.1.6, the strength factor plots were used as a guide to decide which offset intervals to include for the different events and to decide the weighting factor for the different events at the different offsets. I.e. the L_n, H_n and $W_{n,x}$ in the objective function shown in Equation 4.10.

The raytracing model used to predict the arrival times of the events was a 1D model. As the actual seabed at Snorre is dipping, the arrival times for the events at large offsets and for high multiple orders became wrong. Because of this, a maximum offset limit for the time shifts to include in the inversion was sat to 6000 meters. By taking a look at the strength factor plots in Figure 4.17 it is clear that the high amplitude zone of the events moves towards larger offsets for higher multiple orders. For offset below 6000 meters, only the direct wave, 1st and 2nd multiple have their high amplitude zone. The high amplitude zones of the 3rd multiple starts at 6000 meters, and for higher order multiples the high amplitude zones will be at even larger offsets. Based on this, only the direct wave, 1st and 2nd multiple was included in the inversion and in the objective function in Equation 4.10. The offset intervals included was 0-4000 meters for the direct wave, 0-6000 meters for the 1st multiple and 1500-6000 meters 2nd multiple. Even though the high amplitude zone of the 2nd multiple was for offsets above 3200 meters, the 2nd multiple was included for offsets down to 1500 meters. This was in order to capture the tidal level change, which is most prominent at the time shift curves for the short offsets.

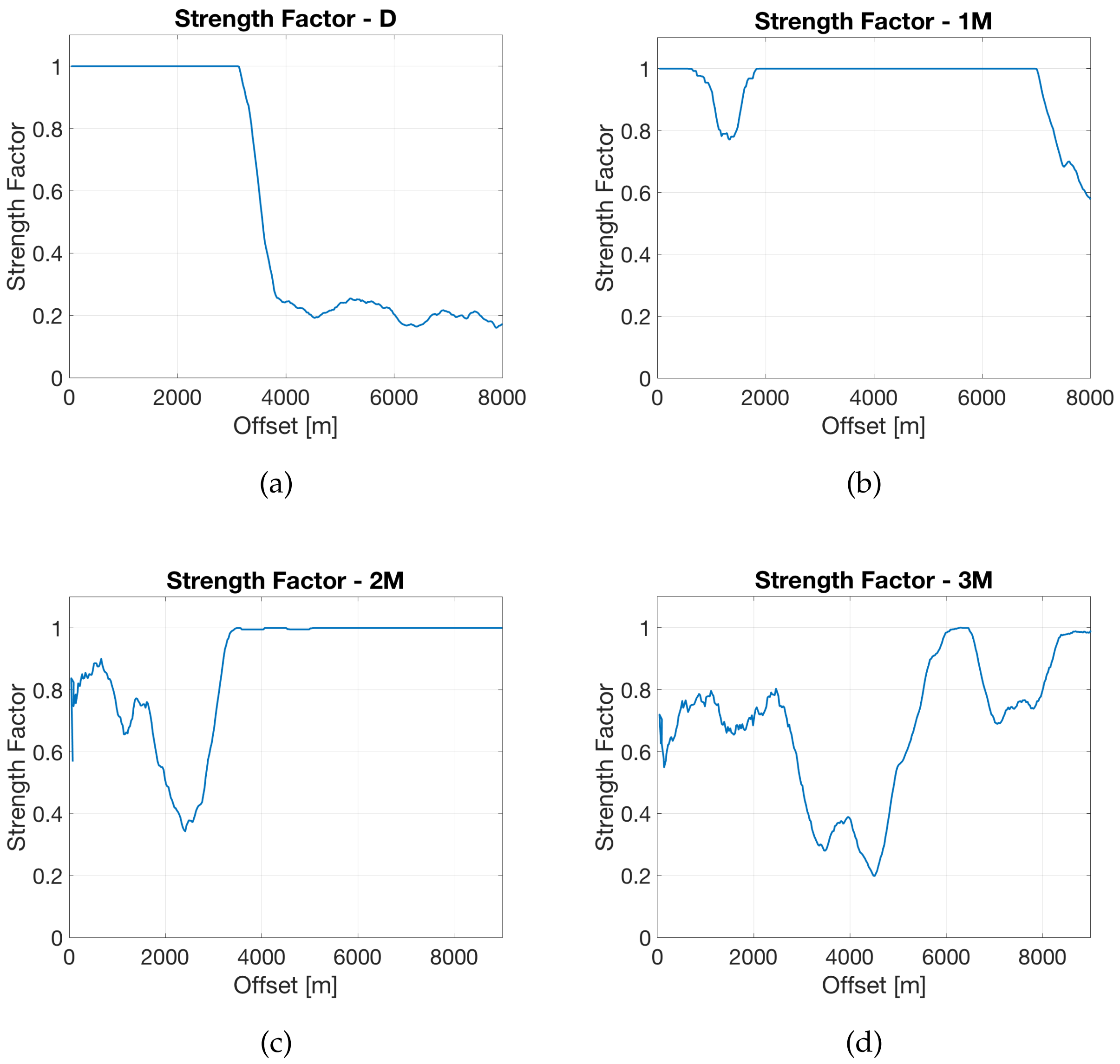

(a) (b)

(c) (d)

Figure 4.17: Figures show the strength factor for the direct wave (a), 1st multiple (b), 2nd multiple (c) and 3rd multiple (d). The strength factor is the amplitude of the event divided by the largest amplitude in a window of 100 ms around the event. A strength factor of 1 indicates that the event has larger amplitude than the surrounding signal and that the cross-correlation should work well. Note how the zones with strength factor of 1 ("high amplitude zones") move towards higher offsets for higher order multiples. This is the same trend as seen in Figure 4.16.

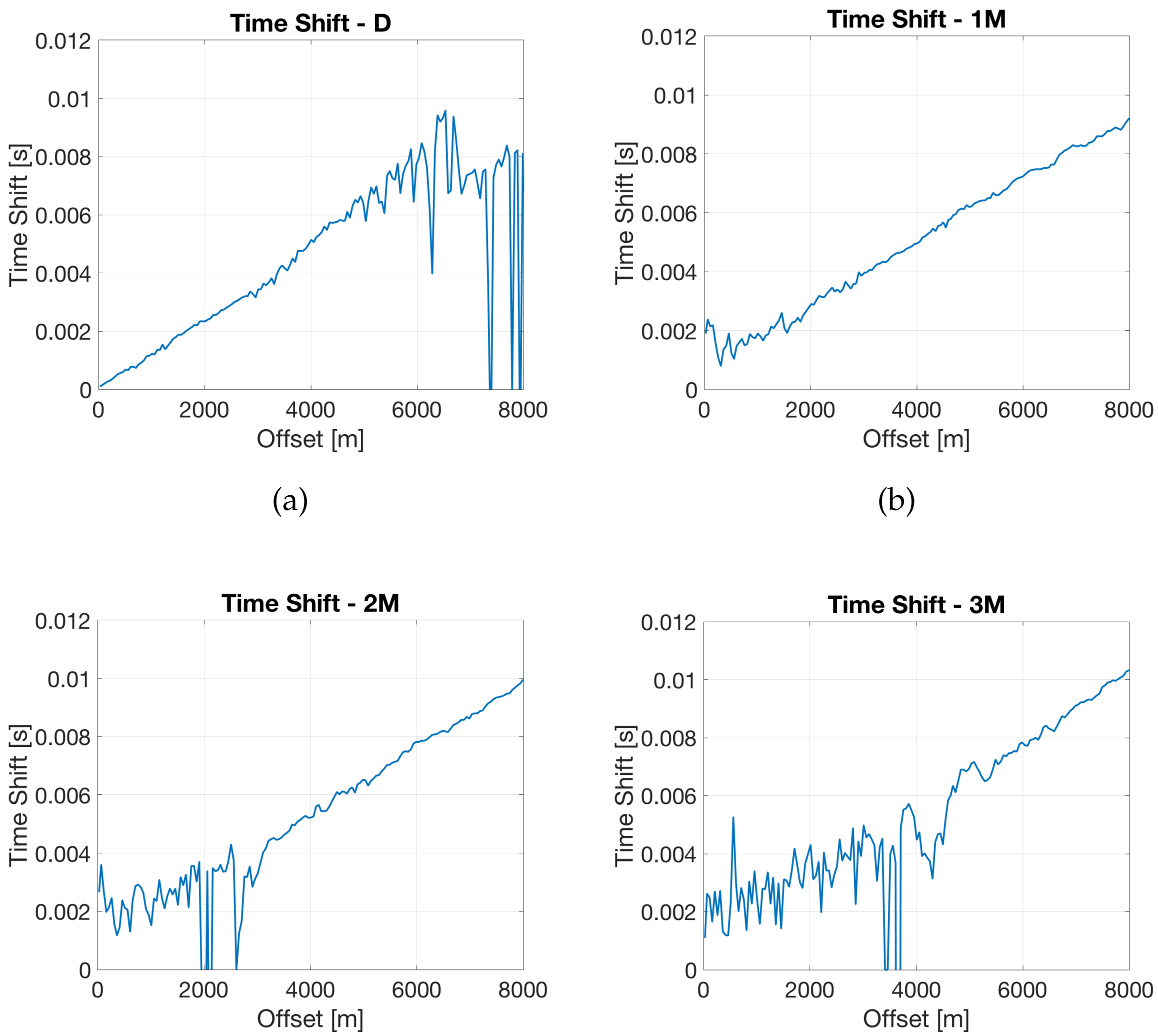

(a) (b)

(c) (d)

Figure 4.18: Figure shows time shift curves for the direct wave (a), 1st multiple (b), 2nd multiple (c) and 3rd multiple (d). No smoothing or outlier removal is performed. Note how the good quality zone of the time shift curve changes with offset for the different events. The good quality zones of the time shift curves matches approximately the same offset intervals as the intervals with high strength factors in Figure 4.17.

Refracted Waves

Several refracted waves were present in the Snorre data, which can be seen from Figure 4.16. The refracted and diving waves will be time shifted differently than the water column events, and in the zones where they interfere with the water column events, errors in the time shift curves may occur. The refracted waves seen in Figure 4.16 are not very strong, but will disturb the time shift estimations in some extent.

Results and Other Datasets

The TSCI method described in this section was based on the Snorre data, and the results of applying the TSCI method to the Snorre data is shown in Section 5.3. However, the TSCI method should work well for other 4D seismic datasets, as long as the offset intervals and multiple orders included in the inversion is adjusted to each specific dataset. For this purpose, strength factor plots will be very useful.

4.2 Test on Realistic Seismic and Subsurface Models

To investigate the strengths and limitations of the TSCI method, several tests were performed with synthetic data. The physical properties of the shallow subsurface have a large impact on the measured seismic signals. In order to make the synthetic data as realistic as possible, a detailed subsurface model of the shallowest subsurface at Snorre was made. The subsurface model was made based on shallow VSP (Vertical Seismic Profiles) data, along with a method based on following of first breaks in shot gathers. The way the subsurface model was obtained is further described in Appendix B.5. The resulting assumed P-wave velocity profile for the shallow subsurface at Snorre is shown in Figure 4.19.

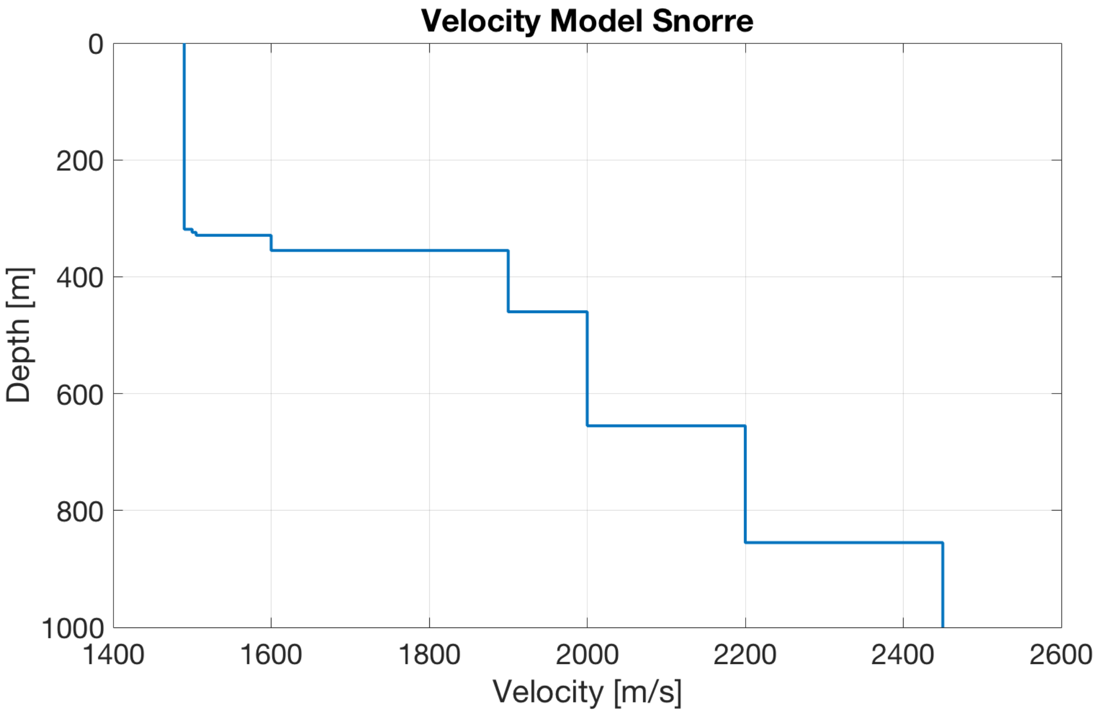

Figure 4.19: Assumed P-wave velocity model for the shallow subsurface at Snorre, based on VSP data and a method based on following first-breaks described in Appendix B.5. The y-axis is given in depth below the sea surface.

The raytracing model used to calculate the forward response during the inversion (described in section 4.1.5), is very simple. It only calculates the arrival times for the water layer events with a 1-layered model of the water column. Hence, there are several wave effects occurring in real seismic that not is accounted for. One such effect is the phase rotation for post critical angles. For pre-critical angles, the phase is constant and the reflection coefficient stays real. However, as the angle of incidence increases to post critical angles, the reflection coefficient becomes complex, and the phase starts to rotate. This phenomenon is usually called "the post-critical effect" Zhang et al. (2012). The magnitude of the phase rotation depends on the properties of the media above and below the interface. Figure 4.20 shows the phase rotation that happens for post-critical angles for the assumed velocity model at Snorre in Figure 4.19. The phase is 0 until the incidence angle exceeds 79 degrees, and the phase starts to rotate. This phase change causes the wave pulse to change shape, which may affect the time shift measurements by creating additional time shift "artifacts".

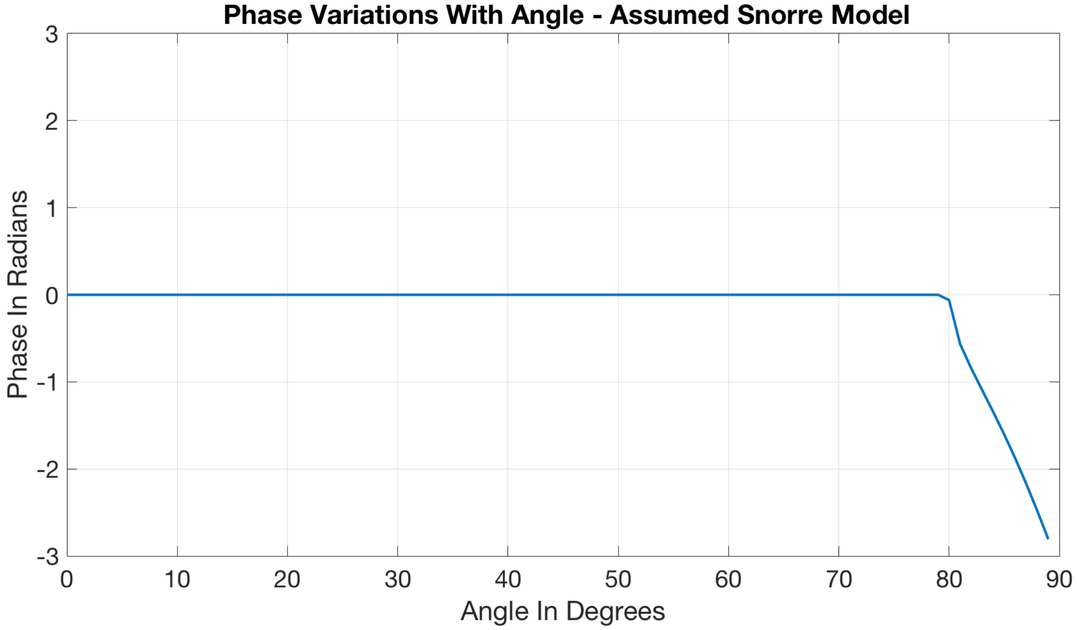

Figure 4.20: Phase variation with angle, calculated with the Zoeppritz Equation, for the assumed subsurface model at Snorre shown in Figure 4.19. The density of water layer and the sea bottom was assumed to be 1.0 g/cm^3 and 1.7 g/cm^3 respectively. Note the phase rotation occurring as the incidence angle exceeds 79 degrees.

In addition to the phase rotation, effects like reflections from deeper boundaries, refractions, mode conversions, normal modes and reflection coefficient variation with angle are not taken into account by the simple raytracing model. Hence, the raytracing model is a large simplification of the reality. To investigate if the simple raytracing model could be used as a base model to calculate the forward response during the inversion, even though it did not take these effects into account, the TSCI method was tested on an advanced and realistic synthetic model. The assumed subsurface velocity model for Snorre in Figure 4.19 was inserted into the SKB modelling software (described in Section 2.8) to produce realistic synthetic shot gathers based on the full subsurface model. Figure 4.21 illustrates the model used for the test, and the model parameters are given in Table 4.1. Each layer, highlighted by the numbers to the left in Figure 4.21 corresponds to a row in Table 4.1. Offsets from 0 to 6000 meters were included, with 51 sea bottom receivers located 120 meters apart. The base water depth was sat to be equal the water depth for the receiver to the far west at line 27 at Snorre, 318.7 meters.

With the SKB modelling, 2 pairs of synthetic shot gathers were made, consisting of 2 vintages each. Pair 1 corresponded to a pure velocity change of 3 m/s, and Pair 2 corresponded to a pure tidal change of 0.5 meters. The water velocity and water depth for the 2 shot gather pairs are given below:

- **Pair 1:** Pure Velocity Change of 3 m/s
    - **Vintage 1:** Water Velocity: 1490 m/s, Water Depth: 318.7 meters
    - **Vintage 2:** Water Velocity: 1487 m/s, Water Depth: 318.7 meters
- **Pair 2:** Pure Tidal Change of 0.5 meters
    - **Vintage 1:** Water Velocity: 1487 m/s, Water Depth: 318.7 meters
    - **Vintage 2:** Water Velocity: 1487 m/s, Water Depth: 319.2 meters

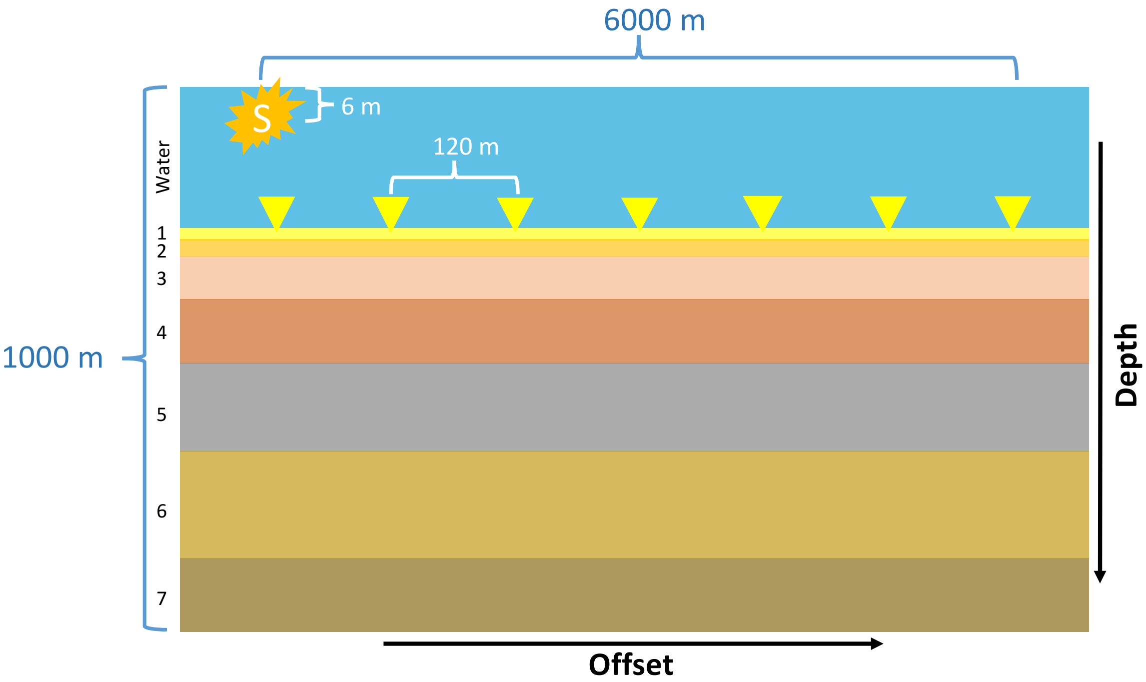

Figure 4.21: Illustration of the model used for the SKB modelling. The numbers to the left (1-7) are the layer number below the water layer. The total height of the model is 1000 meters, and the maximum offset is 6000 meters. 51 receivers were included, with a receiver spacing of 120 meters. The source, highlighted by the "S", was located 6 meters below the water surface. Table 4.1 lists the layer properties for each layer. The relative layer thicknesses in this figure are not correct.

Model Parameters				
Layer	Thickness $[m]$	P Velocity $[m/s]$	S Velocity $[m/s]$	Density $[g/cm^3]$
Water Layer	318.7 / 319.2	1487 / 1490	0	1
Layer 1	5.3	1500	100	1.7
Layer 2	5	1505	300	1.8
Layer 3	26	1600	500	1.9
Layer 4	105	1900	550	1.9
Layer 5	195	2000	600	1.9
Layer 6	200	2200	1000	1.9
Layer 7	145	2450	1000	1.9

Table 4.1: Model parameters for the models used for the SKB modelling. The models consisted of 8 layers, with a total thickness of 1000 meters. Figure 4.21 illustrates the model used. The numbers to the left in figure 4.21 (1-7) correspond to the layer numbers in the leftmost column in this table, so each row lists the parameters for a separate layer.

The TSCI method described in Section 4.1 was used to estimate the known velocity and tidal changes from the two pairs of synthetic shot gathers separately. The offset intervals included in the inversion was 0 to 6000 meters and equal for all the water column events. In addition, the weighting term was sat to 1 for all water column events. The objective function in Equation 4.10 that was minimized during the inversion in the TSCI method, then reduced to

$$\phi(\Delta v) = \sum_{n=1}^{N} \sum_{x=0}^{6000} |M1_{n,x} - S_{n,x}(\Delta v)| \tag{4.11}$$

for the estimation of the velocity change, and

$$\phi(\Delta z) = \sum_{n=1}^{N} \sum_{x=0}^{6000} |M2_{n,x} - S_{n,x}(\Delta z)| \tag{4.12}$$

for the estimation of the tidal change. For event number n and offset x, $M1_{n,x}$ represents the time shifts calculated from the synthetic shot gathers in Pair 1, $M2_{n,x}$ represents the time shifts calculated from the synthetic shot gathers in Pair 2, while $S_{n,x}$ represents the forward modelled time shifts. See Equation 4.10 for more symbols and explanations. To investigate how the accuracy of the estimates varied with the number of multiples included in the calculations, 6 separate inversions were performed with increasing number of included multiples. N in Equation 4.11 and 4.12 increased from 1 (inclusion of only the direct wave) to 6 (inclusion of all the multiples up to 5$^{\text{th}}$ order). The results are shown in Section 5.1.

4.3 Robustness to Error in Inversion Background Model

The background model used for calculating the forward response in the TSCI method, consist of an assumed water depth and an assumed absolute water velocity. However, the exact values of these parameters were not known exactly for the Snorre field. To investigate the robustness of the TSCI method to errors in background model, 2 tests were performed. One test for investigating the robustness to errors in the water depth, and one test for investigating the robustness to errors in the absolute water velocity.

For the tests, 2 synthetic time shift curves were made with the raytracing model described in Section 4.1.5, consisting of a water depth of 320 meters, a base velocity of 1490 m/s and offsets from 0 to 6000 meters:

1. **Time Shift Curve 1:** corresponding to a pure velocity change of 3 m/s
2. **Time Shift Curve 2:** corresponding to a pure tidal change of 1 meter

These time shift curves were used as the "observed time shifts" in the tests.

4.3.1 Error in Background Model - Water Depth

To investigate the effect of assuming wrong water depth, 4 different background models were made with 4 different assumed water depths of 321, 330, 350 and 370 meters. I.e. water depths 1, 10, 30 and 50 meters too deep. 30 and 50 meters are unrealistic large water depth errors, but were added for illustration of the trends. The TSCI method was used to estimate the known water velocity and tidal change for Time Shift Curve 1 and 2 separately, with the use of the 4 different background models for forward response calculations. The test is illustrated in Figure 4.22. The green rays represent the rays for the correct water depth where the "observed time shifts", Δt, is calculated. The red rays represent the rays for a background model with too large water depth, used for calculating the forward response.

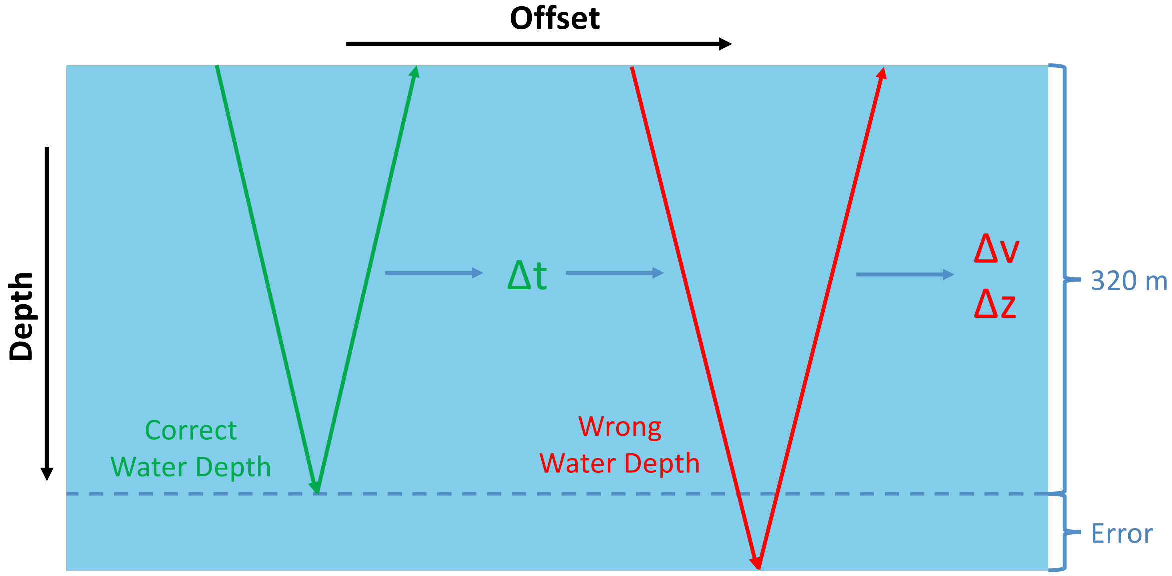

Figure 4.22: Figure illustrates the test of the TSCI method's robustness to errors in the background model water depth. Green rays correspond to the correct water depth where the "observed time shifts", Δt, is calculated. The red rays represent the rays in the 1D raytrace background model, with wrong water depth, which was used to calculate the forward response.

The objective functions used in the inversion and estimation of the water velocity and tidal change were the same as in Equation 4.11 and 4.12 respectively, where $M1_{n,x}$ represented Time Shift Curve 1, and $M2_{n,x}$ represented Time Shift Curve 2. To investigate how the accuracy of the estimates varied with the number of multiples included in the calculations, 10 separate inversions were performed with increasing number of included multiples. N in Equation 4.11 and 4.12 increased from 1 (inclusion of only the direct wave) to 10 (inclusion of all the multiples up to 9th order). The rest of the parameters were the same as described for Equation 4.11 and 4.12. The results of the test is shown in Section 5.2.1

4.3.2 Error in Background Model - Base Water Velocity

To test the TSCI method's robustness to base velocity errors in the background model, Time Shift Curve 1 corresponding to the velocity change of 3 m/s, was used.

Different background models were made, with correct water depth but wrong water velocity ranging from 1460 m/s to 1520 m/s, in steps of 5 m/s. For each background model, the TSCI method described in Section 4.1 was used to estimate the known velocity change. The objective function used was the same as Equation 4.11, where $M1_{n,x}$ represented Time Shift Curve 1. Only the direct wave event was included in the calculations in this test, so N in Equation 4.11 was sat to 1. The rest of the parameters were the same as described for Equation 4.11. The results can be seen in Section 5.2.2.

Chapter 5

Results of the Time Shift Curve Inversion Method

This chapter shows the results obtained from the methods described in Chapter 4. The chapter is divided into 3 main parts

- Test of the TSCI method on realistic seismic and realistic subsurface models
- Test of the TSCI method's robustness to errors in the background model
- Estimates of the water velocity and tidal level changes at Snorre with the use of the TSCI method

In the following, the results for each of these parts are shown, explained and discussed briefly. A more detailed discussion of the results is included in Chapter 6.

5.1 Test of Robustness to Realistic Subsurface and Seismic

The test described in Section 4.2 was used to investigate if the TSCI method based on the 1D raytracing model worked for realistic seismic and for a realistic shallow subsurface model of the Snorre field. The resulting estimates of the water velocity and tidal changes are shown in Figure 5.1 and 5.4 respectively. In both Figures, the x-axis defines the highest multiple order included in the calculations.

Velocity Change Estimates

The velocity change estimates, shown in Figure 5.1, has good precision up to the inclusion of the 2nd order multiple, with a maximum error below 0.07 m/s. However, as higher multiple orders were included, the error increased significantly. For inclusion of all the multiples up to 5th order, the error became 0.27 m/s. All the velocity change estimates in Figure 5.1 are underestimated.

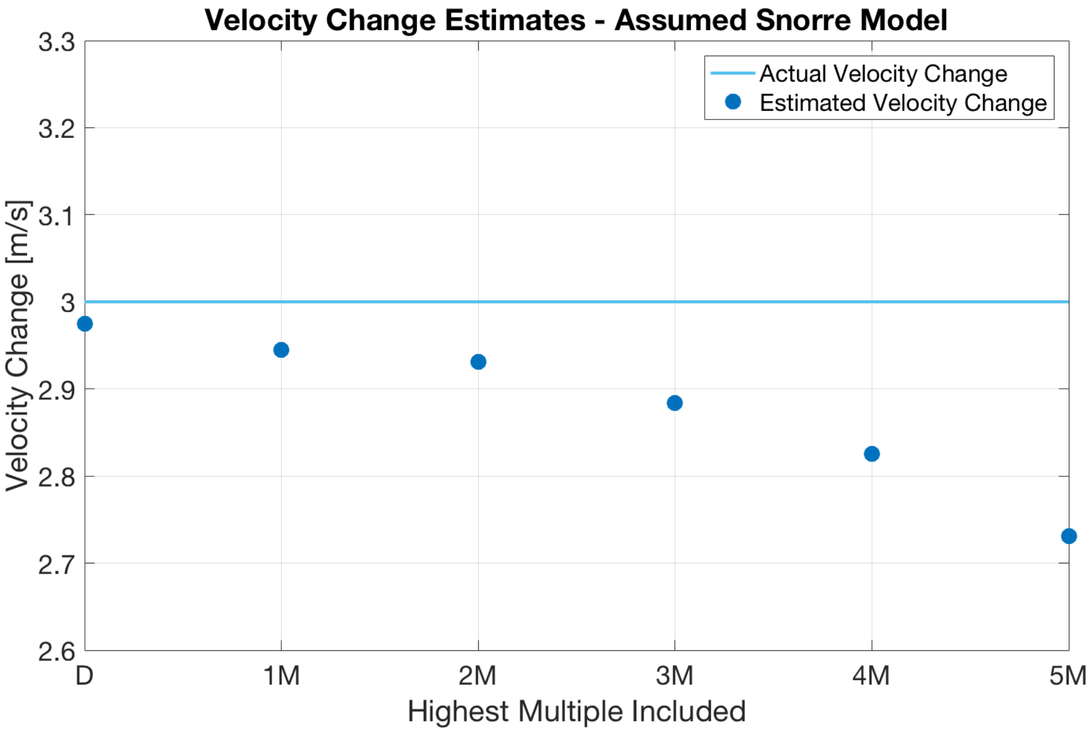

Figure 5.1: Velocity change estimates. The TSCI method was tested on realistic synthetic seismic and a realistic shallow subsurface model of the Snorre field. The known velocity change was 3 m/s, highlighted by the light blue line. The dark blue dots are the velocity changes estimated with the TSCI method. The x-axis defines the highest multiple order included in the calculation. "D" indicates that only the direct wave was included, "1M" indicates that both the direct wave and the 1st multiple were included, and so on. Note that all the estimates are underestimated and that the error increases for the inclusion of the high order multiples.

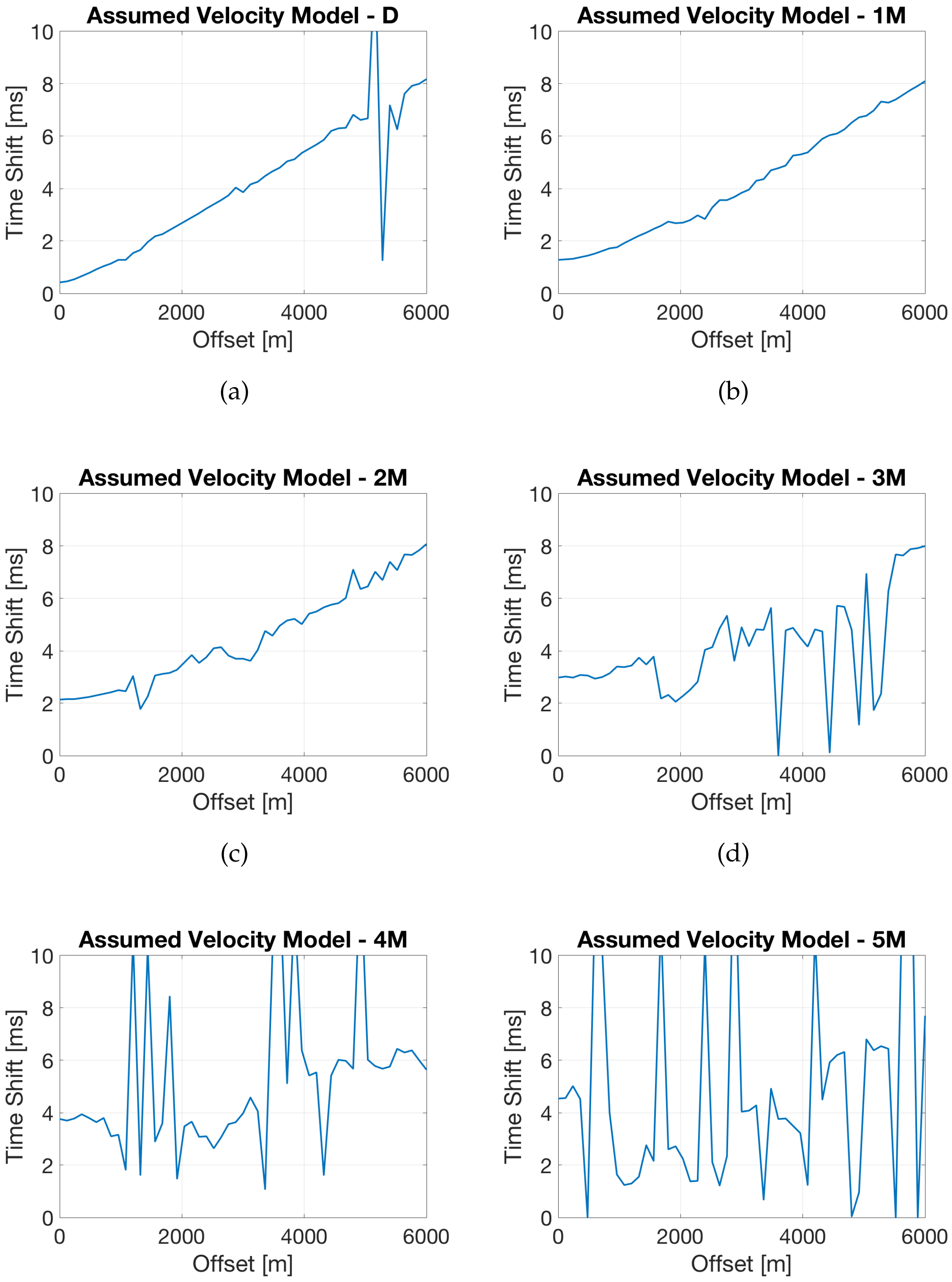

(a) (b) (c) (d) (e) (f)

Figure 5.2: Raw time shift curves corresponding to the shot gather pair with a velocity change of 3 m/s, for the direct wave (a), 1st (b), 2nd (c), 3rd (d), 4th (e) and 5th (f) multiple. The velocity change estimates in Figure 5.1 were based on these time shift curves. Note the correlation between the quality of the time shift curves and the precision of the estimates in Figure 5.1.

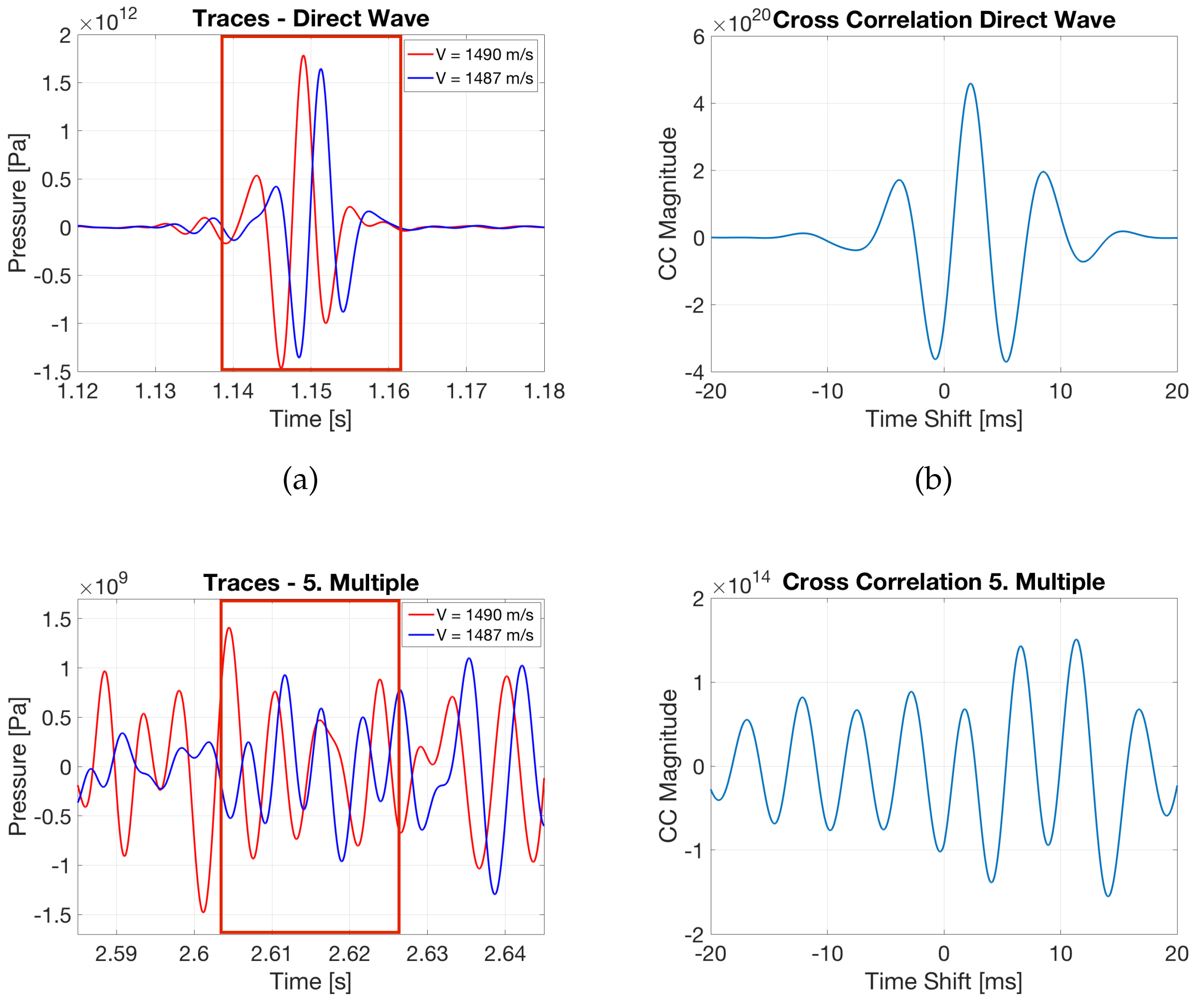

(a) (b)

(c) (d)

Figure 5.3: Traces from the receiver at 1680 meters offset for the synthetic shot gather pair with a velocity change of 3 m/s, for the direct wave (a) and the 5th order multiple (c) along with the corresponding cross correlations in (b) and (d) respectively. The red squares in (a) and (c) represent the 24 ms long time window used for cross-correlation in the test. Only the part of the traces inside the window was cross-correlated. The high amplitude events in (a) result in a simple cross-correlation series in (b) with a large peak. The chaotic traces in (c) results in a messy cross-correlation series in (d).

The raw time shift curves for the synthetic shot gathers, which the estimated velocity changes in Figure 5.1 were based on, are shown in Figure 5.2. The time shift curves for the direct wave, 1st and 2nd multiple are relatively smooth and the trend of time shift increase with offset is clear. However, the time shift curves for the 3rd, 4th and 5th multiple are very spiky and it is difficult to infer a smooth time shift trend. The spikes and outliers in the time shift curves can be due to interference between the water layer events and the refracted waves, diving waves or reflections from deeper boundaries. By comparing Figure 5.1 and 5.2, it is easy to see the connection between the precision of the velocity change estimates and the quality of the time shift curves. Smooth and high quality time shift curves result in precise estimates. Poor quality and spiky time shift curves result in reduced precision.

The phase change for post critical angles discussed in Section 4.2 changes the shape of the wave pulse at large offsets. This may result in time shift artifacts, which affects the time shift curves for the direct wave and low order multiples at large offsets. However, in general, the time shift curves in Figure 5.2 seem to increase relatively constant and smoothly for the direct wave, 1st and 2nd multiple. In addition, the velocity change was estimated quite precisely for the low order multiples. Based on these observations, the phase changes for post critical angels seem to have low effect on the resulting time shift curves and the estimated water column changes.

To better understand the variation in time shift curve quality in Figure 5.2, the traces and the corresponding cross-correlations for the direct wave and the 5th multiple, for the receiver located at 1680 meters offset, are shown in Figure 5.3. As the amplitude of the direct wave event in (a) is large compared to the surrounding signal, the cross-correlation of the signals inside the red correlation window results in a large peak for the correct time shift in (b). This gives rise to the high quality time shift curve in Figure 5.2 (a). For the 5th multiple there are lots of interfering signal and no distinct events can be seen inside the red correlation window in Figure 5.3 (c). This results in a messy cross-correlation series with many equal sized peaks in (d). The wrong time shifts get estimated, resulting in the poor quality time shift curve as seen in Figure 5.2 (f). From these observations it was inferred that the precision of the velocity change estimates in Figure 5.1 is good for the direct wave, 1st and 2nd multiple because the amplitude of the events is larger than the surrounding signal. This results in correct cross-correlation and high quality time shift curves. The precision of the estimates reduces as the 3rd, 4th and 5th multiple are included because the amplitude of these events is lower than the surrounding signal. This results in incorrect cross-correlation and wrong time shift curves.

Tidal Change Estiamtes

The estimated tidal changes from the test in Section 4.2 are shown in Figure 5.4. The tidal changes were estimated with very good precision up to the inclusion of the 3rd order multiple. The best estimate was obtained by including the direct wave and the 1st multiple, with an error of only 2 mm. The error increased as the higher order multiples were included. Figure 5.5 shows the raw time shift curves for the synthetic shot gather pair the estimates in Figure 5.4 were based on. Figure 5.5 shows the same trend as seen in Figure 5.2, reduced quality of the time shift curves for the high multiple orders. This explains the increase in error for the estimated tidal change for the inclusion of the 4th and 5th multiple in Figure 5.4.

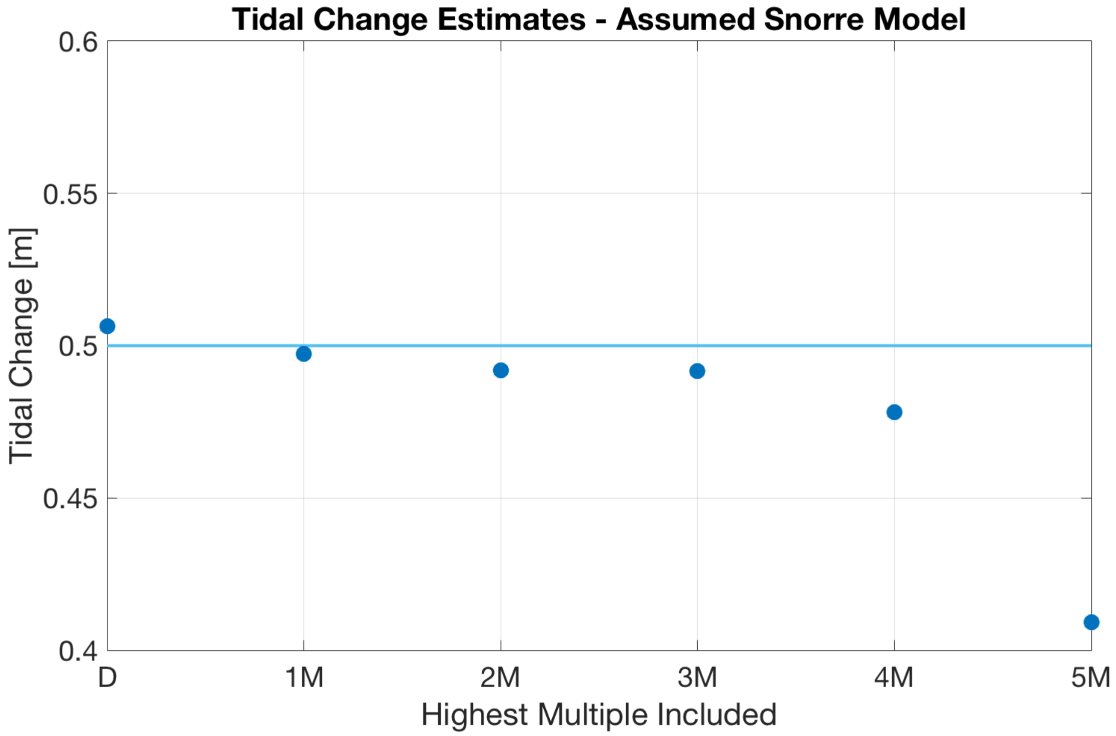

Figure 5.4: Tidal change estimates. The TSCI method was tested on realistic synthetic seismic and a realistic shallow subsurface model of the Snorre field. The known tidal change was 0.5 meters, highlighted by the light blue line. The dark blue dots are the tidal change estimates. The x-axis defines the highest multiple order included in the calculation. "D" indicates that only the direct wave was included, "1M" indicates that both the direct wave and the first multiple were included, and so on.

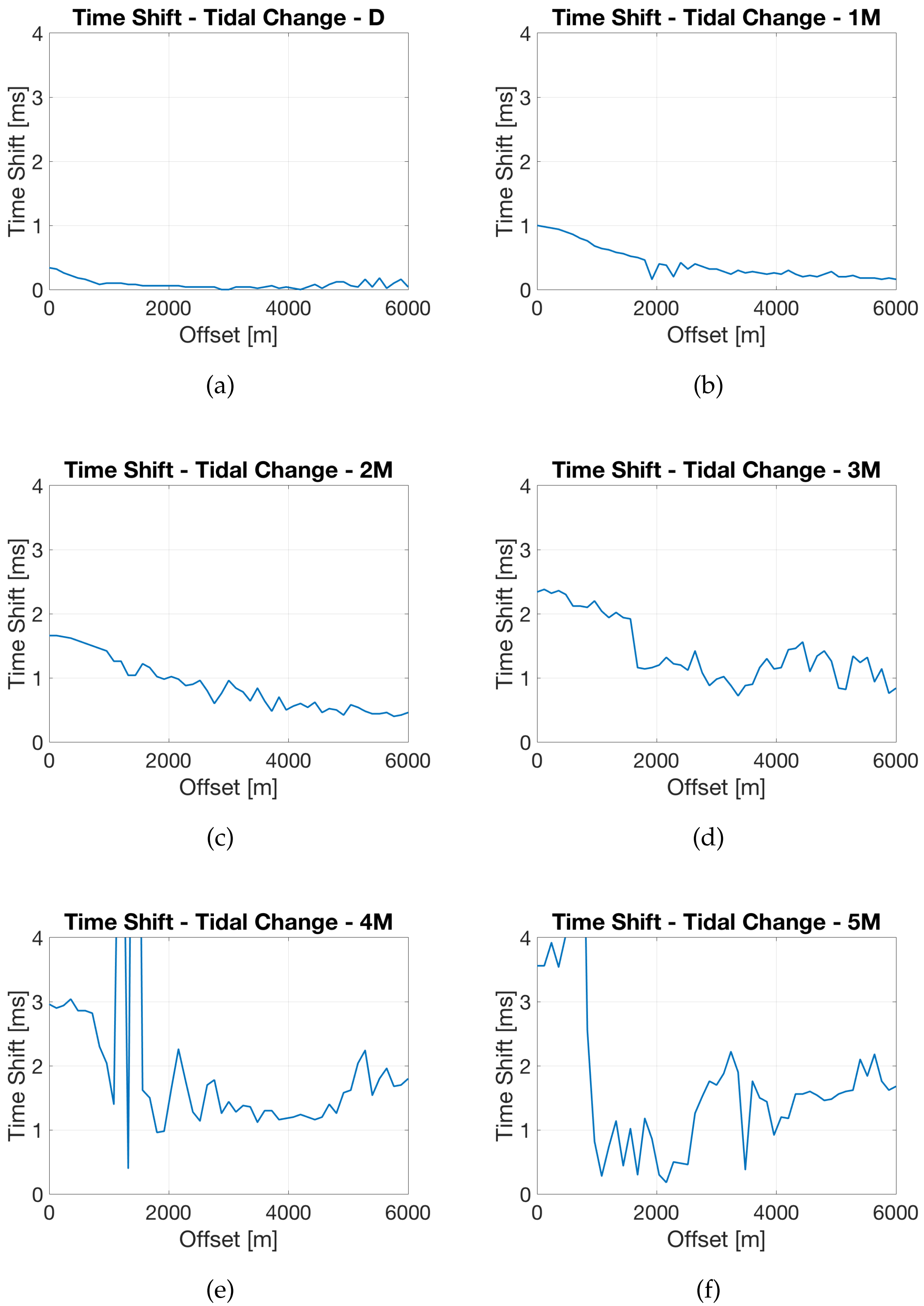

Figure 5.5: Raw time shift curves corresponding to the shot gather pair with a tidal change of 0.5 meters, for the direct wave (a), 1st (b), 2nd (c), 3rd (d), 4th (e) and 5th (f) multiple. The tidal change estimates in Figure 5.4 were based on these time shift curves. Note the correlation between the quality of the time shift curves and the precision of the estimates in Figure 5.4.

To summarize, the estimates in Figure 5.1 and 5.4 show that the TSCI method gives precise results for realistic seismic and realistic subsurface models as long as the time shift curves the estimates are based on have high quality. Since the quality of the time shift curve for the high order multiples reduces, the inclusion of these multiples results in reduced precision of the estimated water column changes.

Robustness to Subsurface Velocity and Layer Thickness Variations

The subsurface is in general not a simple layered model. It can be complex and changes occur both laterally and vertically. Appendix B.6 shows the methods and the results of 2 tests used to investigate the TSCI method's robustness to variations in subsurface velocities and subsurface layer thicknesses. The main result from the tests is that the TSCI method is relatively robust to changes in both subsurface velocities and to subsurface layer thicknesses. However, the number of high order multiples and the offset intervals included for each water column event need to be adjusted to the specific model as the model decides how the reflection coefficient varies with angle and the amplitude of the water column events.

5.2 Robustness to Errors in the Inversion Background Model

5.2.1 Test of Wrong Water Depth

Section 4.3.1 describes the tests used to investigate the TSCI method's robustness to errors in the assumed water depth in the background model used for forward modelling during the inversion. The results of the tests are shown in Figure 5.6 for the velocity change estimates and in Figure 5.7 for the tidal change estimates.

Figure 5.6 shows the estimated velocity changes plotted against the highest multiple order included in the calculations. For all background models, the error increases with multiple order. The velocity changes estimated with the background model of 1 meter too large water depth, are very precise. This is also the case for the estimates with the background model of 10 meters too large water depth, with a maximum error of 0.05 m/s for the inclusion of the 9th multiple. As the water depth in the background model is 30 and 50 meters to deep, the error in the estimated velocity changes increases, but not by much. The maximum error for the background model with 50 meters too large water depth is 0.25 m/s.

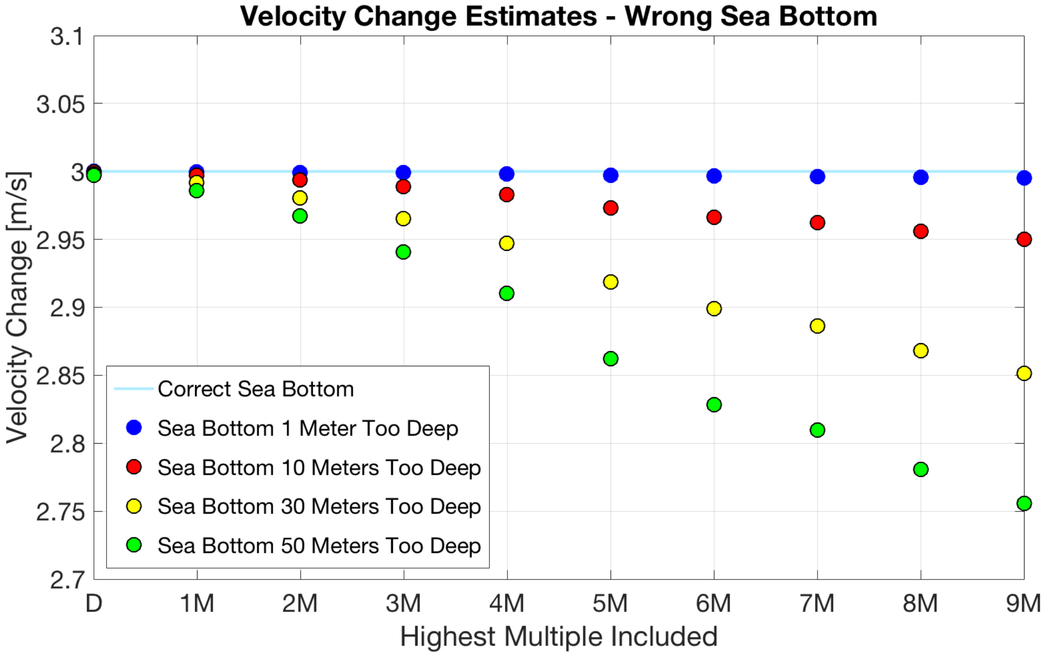

Figure 5.6: Estimated velocity changes for the test of the TSCI method's robustness to errors in the background model water depths. x-axis indicate highest multiple order included in the calculations. "D" indicates that only the direct wave was included, "1M" indicates that both the direct wave and the first multiple were included, and so on. The light blue line represents the actual velocity change of 3 m/s. The blue, red, yellow and green dots correspond to velocity change estimates with the background models of 1, 10, 30 and 50 meters too large water depth respectively. Note that the error in estimated velocity change increases with multiple order.

Figure 5.7 shows the estimated tidal changes plotted against the highest order multiple included in the calculations. For the tidal change estimates, the error actually reduces with increased multiple order, which is the opposite of the velocity change estimates in Figure 5.6. The largest error occurs as only the direct wave is included, while the most precise estimates are obtained as the all the multiples up to 9th order are included. Overall, the estimated tidal changes are precise. As the error in the background model's water depth is below 10 meters, the errors in the estimated tidal changes are below 2.5 cm. The maximum error that occurs as the water depth in the background model is 50 meters wrong, is only 12 cm.

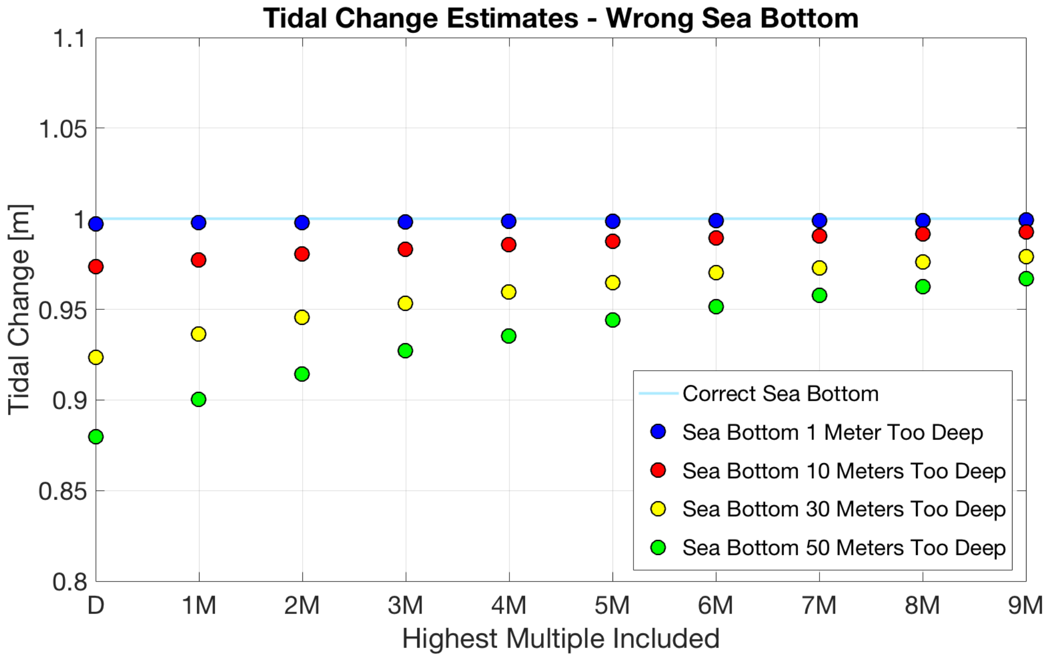

Figure 5.7: Estimated tidal changes for the test of the TSCI method's robustness to errors in the water depth of the background model. The x-axis indicates highest multiple order included in the calculations. "D" indicates that only the direct wave was included, "1M" indicates that both the direct wave and the first multiple were included, and so on. The blue, red, yellow and green dots correspond to tidal change estimates with background models of 1, 10, 30 and 50 meters too large water depths respectively. Note that the error in estimated tidal change decreases with increased multiple order.

An error in the water depth of 50 meters is quite unrealistic. The small error in the estimated water velocity and tidal change for such a large error in the background model water depth, indicate that the TSCI method is quite robust to errors in the water depth of the background model. However, all the estimates in Figure 5.6 and 5.7 became underestimated.

5.2.2 Test of Wrong Base Velocity

Section 4.3.2 describes the test for investigating the TSCI method's robustness to errors in the background model base velocity. The results are presented in Figure 5.8, which shows the estimated velocity changes for background models with different base velocities. The correct velocity change is highlighted by the light blue line, for the correct base velocity of 1490 m/s. For base velocities lower than 1490 m/s, the water velocity changes get slightly underestimated. The opposite happens for base velocities higher than 1490 m/s, where the velocity changes get slightly overestimated.

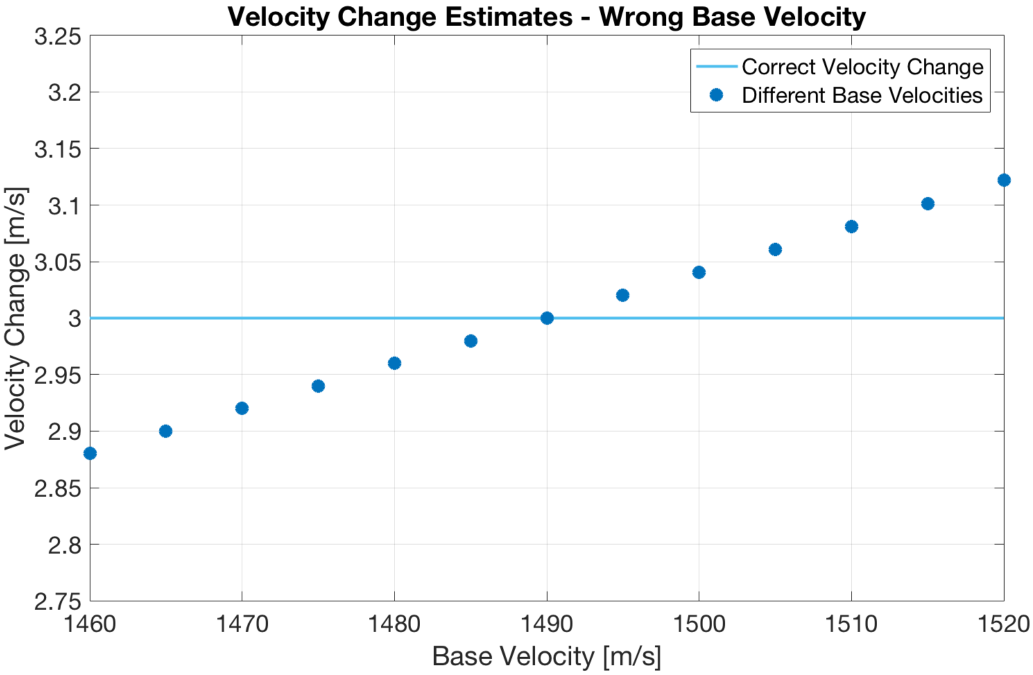

Figure 5.8: Velocity change estimates for the test of the TSCI method's robustness to errors in the background model base velocity. The correct water velocity change is highlighted by the light blue line at 3 m/s. The dark blue dots represent the estimated velocity change for different base velocities used in the forward calculations, indicated by the x-axis. Note the overall low errors.

Overall, the errors in the estimated velocity changes are relatively low. If the base velocity is wrong by 30 m/s, this only leads to an error in the estimated velocity change of ± 0.12 m/s. It is quite unlikely to miss the actual water velocity by 30 m/s. For a more likely error in the base velocity of 10 m/s, the resulting error in the estimated velocity change is only ± 0.04 m/s. This indicates that the TSCI method is relatively robust to errors in the background model's base velocity.

5.3 Water Velocity and Tidal Changes Between Snorre PRM 4 and 5

The results of applying the TSCI method, described in Section 4.1, to the Snorre data is shown in the following subsections. The estimates for both the velocity change, the tidal change and the SOD change between the Snorre PRM 4 and 5 are shown. For all the following figures, the "change" between PRM 4 and 5 is calculated by: Value PRM 5 - Value PRM 4.

Tidal Level Change Estimates

Figure 5.9 shows the estimated tidal changes between Snorre PRM 4 and PRM 5 for shot number 120 to 453. The red curve is the tidal changes estimated for positive offsets, while the light blue curve is the tidal changes estimated for negative offsets. The green line is the measured tidal change from the PIES, described in Section 3.3.

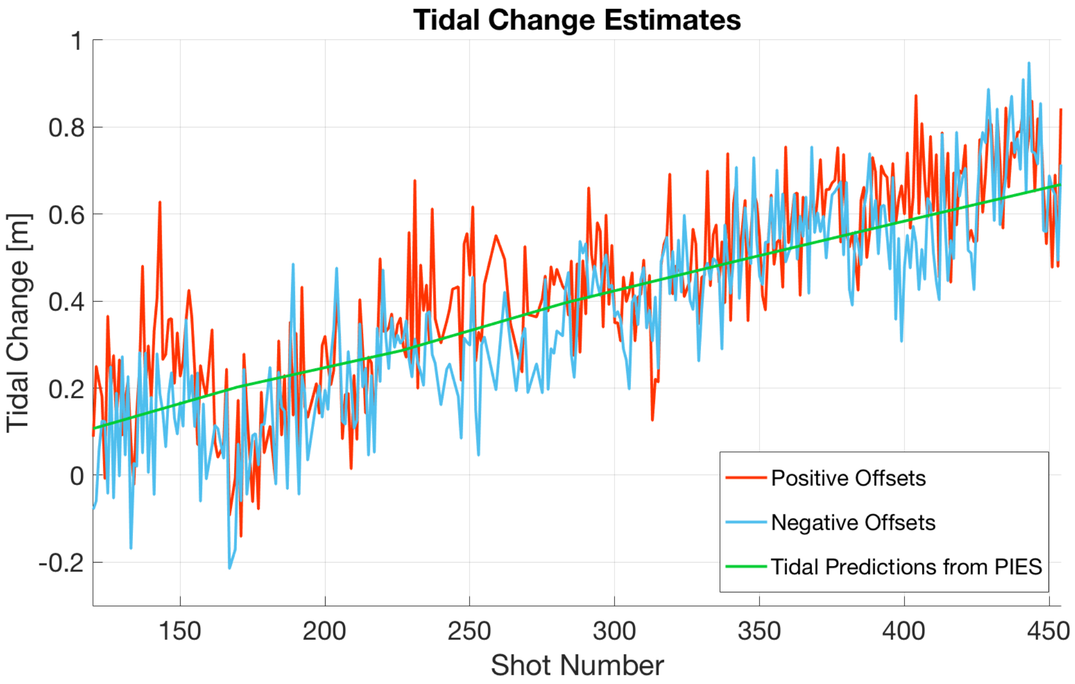

Figure 5.9: Estimated tidal changes between Snorre PRM 4 and 5 with the use of the TSCI method described in Section 4.1. The red curve shows the estimates for positive offsets. The blue curve shows the estimates for negative offsets. The green line is the tidal level difference calculated from the PIES measurements (the same as in Figure 3.7)

The tidal changes estimated with the TSCI method in Figure 5.9 follow the same trend as the tidal measurements from the PIES: the tidal change increases with increased shot number. However, the estimated tidal changes oscillate up and down with a high frequency. As the tidal change is known to vary smoothly in a long periodic trend, the long periodic increase in tidal level change is most likely caused by the actual tidal variations between the surveys. The high-frequent oscillations can have been caused by ocean waves that pull the source up and down during the acquisition of the PRM surveys.

To illustrate the long periodic tidal variations in a better way, the estimated tidal changes were smoothed by a moving average filter of 20 points. The result is shown in Figure 5.10. The increase in tidal change with increased shot number becomes even more evident after the smoothing. The tidal changes estimated for positive and negative offsets follow the same trend, but the estimates for positive offsets are in general a little higher than the estimates for negative offsets. In addition, the positive and negative offsets seem to mirror each other in certain shot number intervals. This is especially prominent in the shot number intervals 225-300 and 375-425.

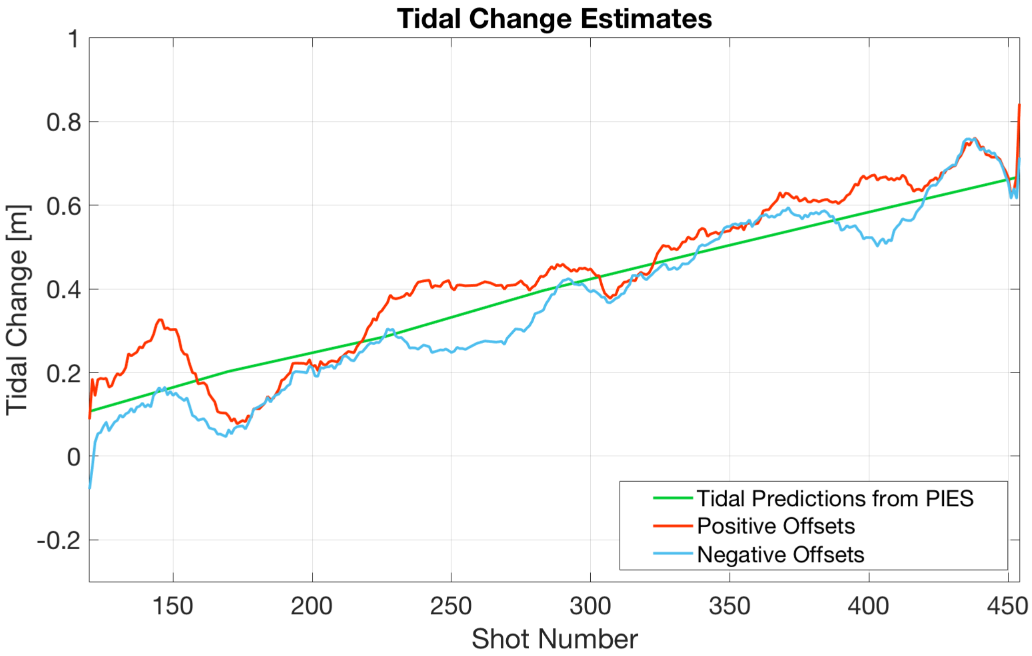

Figure 5.10: Smoothed tidal changes between Snorre PRM 4 and 5. Same as in Figure 5.9, but smoothed with a moving average filter of 20 points. The red curve shows the estimates for positive offsets. The blue curve shows the estimates for negative offsets. The green line is the tidal level difference calculated from the PIES measurements.

To obtain a single estimate of the tidal level change at each shot number, the estimated tidal changes for positive and negative offsets in Figure 5.9 were averaged for each shot number. The result is shown as the blue curve in Figure 5.11. Based on the observations of the tidal levels measured by the PIES in Figure 3.7, along with the pressure corrected tidal predictions in Figure 3.8, the tidal change between Snorre PRM 4 and 5 was expected to increase approximately linearly with shot number. Therefore, a linear fit was performed to the tidal change estimates, shown by the red curve in Figure 5.11. The difference between the linear tidal change curve and the tidal change measurements from the PIES is small. The maximum error between the two curves is below 5 cm. However, the gradient of tidal level change increase with shot number is slightly steeper for the linear fit than for the PIES measurements.

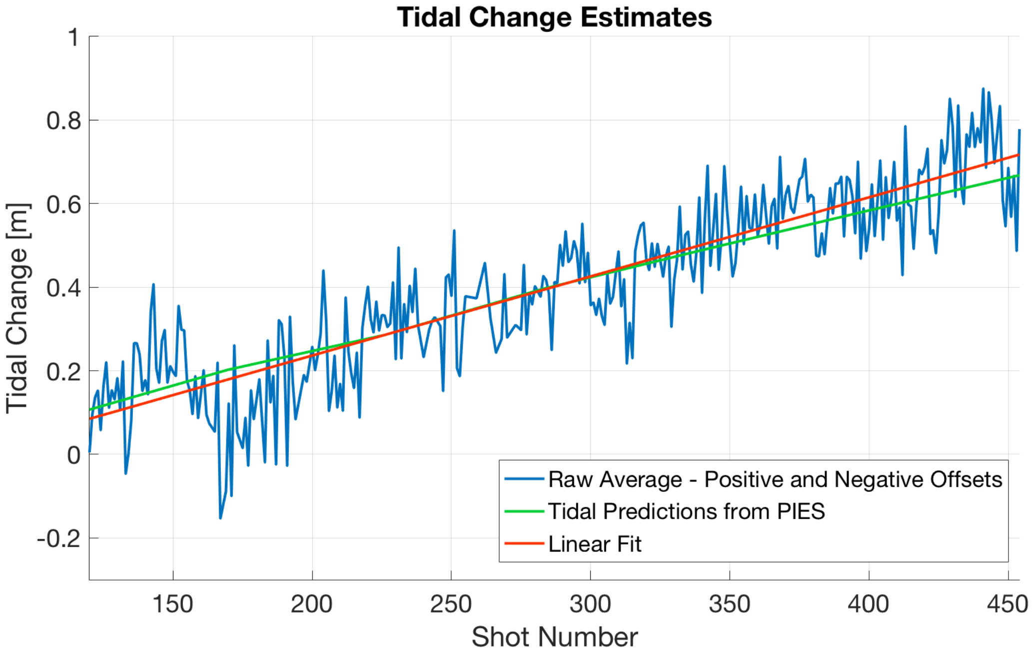

Figure 5.11: Estimated tidal changes between Snorre PRM 4 and 5. The blue curve illustrates the average of the tidal changes estimated for positive and negative offsets in Figure 5.9. The red curve is a linear fit to the tidal change estimates in the blue curve. The green curve is the tidal change measurements from the PIES.

Since the high-frequency oscillations of the tidal change estimates in Figure 5.9 and 5.11 were assumed to be caused by ocean waves, it is the long periodic behavior of the time shift estimates that contains the tidal change information. Because of this, the linear fit in Figure 5.11 was expected to be the most correct estimate for the tidal change between

Snorre PRM 4 and PRM 5.

Water Velocity Change Estimates

Figure 5.12 shows the estimated water velocity changes between Snorre PRM 4 and 5 with the use of the TSCI method. The red curve shows the estimates for positive offsets, while the light blue curve shows the estimates for negative offsets. The magnitude of the velocity change estimated for negative offsets is a little lower than the magnitude of the velocity change estimated for positive offsets. In addition, both the estimates for positive and negative offsets have a slight trend of decreased magnitude of the velocity change with increased shot number.

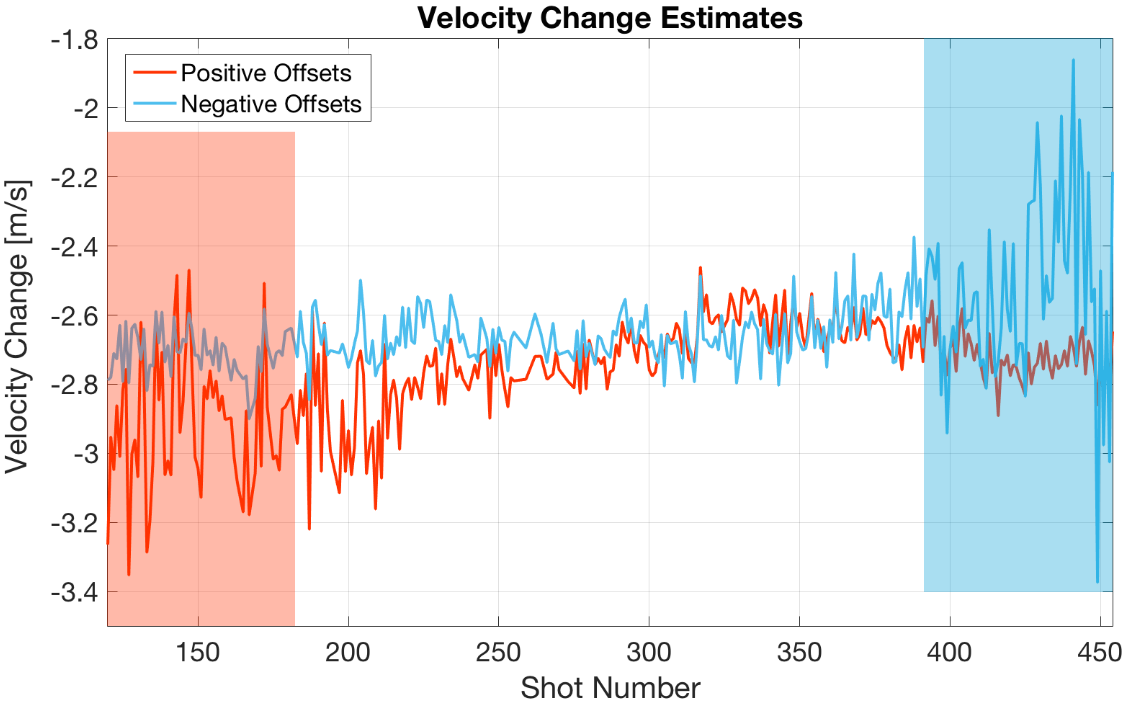

Figure 5.12: Water velocity changes between Snorre PRM 4 and 5, estimated with the TSCI method. The red curve shows the estimates for positive offsets, while the blue curve shows the estimates for negative offsets. Note the large variations for the red curve at low shot numbers and the blue curve at large shot numbers, highlighted by the red and blue squares respectively. The red and blue squares cover 60 shots each, shot number 120-180 and 393-453 respectively.

The estimates for positive offsets have largest variation for low shot numbers, but get more stable for larger shot numbers. The estimates for negative offsets have largest variation for high shot numbers, but are more stable at low shot numbers. The parts of the estimated velocity changes with largest variations are the 60 first shot numbers for positive offsets and the 60 last shots the for negative offsets. These parts are highlighted by the red and the blue squares in Figure 5.12. To increase the stability and the confidence in the estimated velocity changes, the estimates for positive offsets inside the red square and the estimates for negative offsets inside the blue square, were removed.

The frequency distributions of the velocity change estimates after the removal of the parts with largest variation is shown in Figure 5.13. (a) shows frequency distribution for the estimates at positive offsets, while (b) shows frequency distribution for the estimates at negative offsets. The mean for positive offsets is -2.73 m/s and the mean for negative offsets is -2.66 m/s, a difference of 0.07 m/s. The variation in estimated velocity change is larger for positive offsets than for negative offsets. This can be seen by the larger spread in the frequency distribution and higher standard deviation for velocity changes estimated at positive offsets than for negative offsets. However, the standard deviation for both positive and negative offsets was relatively low, ± 0.12 m/s and ± 0.08 m/s respectively.

Figure 5.14 shows the frequency distribution of the estimated water velocity change for both the estimates at positive and negative offsets. The mean is -2.70 m/s, with a low standard deviation of ± 0.10 m/s. The low standard deviation indicates that the estimates are relatively consistent.

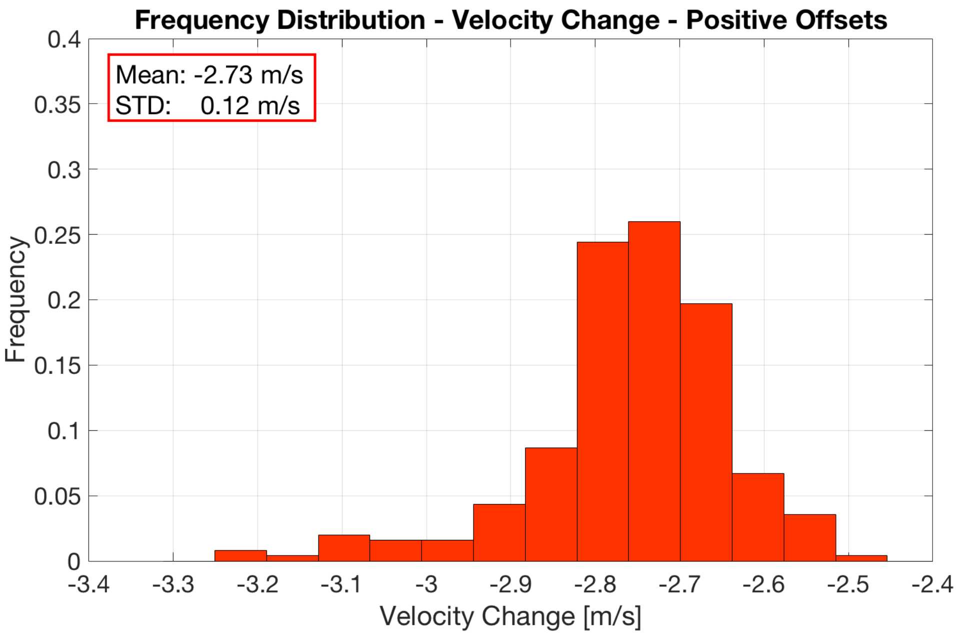

(a)

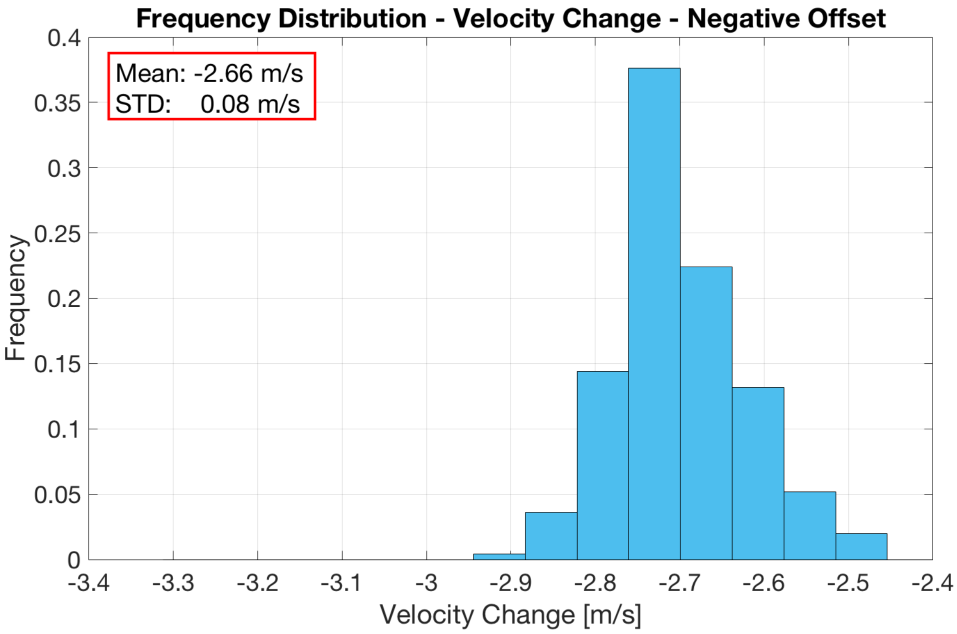

(b)

Figure 5.13: Frequency distribution of the estimated water velocity changes for positive offsets (a), and negative offsets (b). The velocity estimates for the 60 first shots for positive offsets and the 60 last shots for negative offsets were removed. The mean and standard deviation are shown in the red boxes to the upper left. The mean is a little higher for positive offsets than negative offsets. The standard deviation is also larger for positive offsets, which can be seen by the larger spread of the frequency distribution in (a) than in (b).

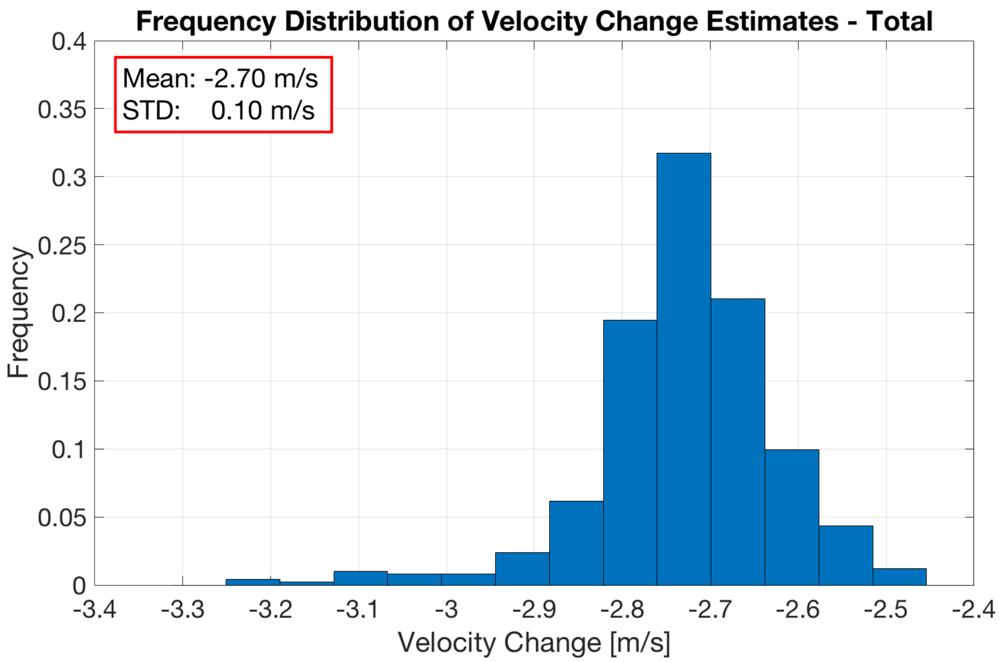

Figure 5.14: Frequency distribution for the estimated water velocity change for both positive and negative offsets after the removal of the velocity change estimates for the first 60 shots for positive offsets and the last 60 shots for negative offsets. The mean is -2.70 m/s, while the standard deviation is ± 0.10 m/s.

Start of Data Delay Difference

The change in start of data delay between Snorre PRM 4 and 5, estimated with the TSCI method, is shown for positive and negative offsets in Figure 5.15. In general, the SOD changes estimated for positive offsets are a little lower than the ones estimated for negative offsets. A positive value of the SOD change indicates that PRM 5 should be shifted towards lower traveltimes with the absolute value of the SOD change to match the traveltimes for PRM 4. A negative value of the SOD change indicates that PRM 5 should be shifted towards larger traveltimes with the absolute value of the SOD change to match PRM 4.

The average of the SOD change for positive and negative offsets is shown in Figure 5.16. The average SOD change varies between -0.6 and 0.25 ms, however, for the majority of the shots the SOD change is negative. The magnitudes of the estimated SOD changes in Figure 5.15 and 5.16 are relatively low, so the start of data delay for PRM 4 and 5 is assumed to have been relatively equal.

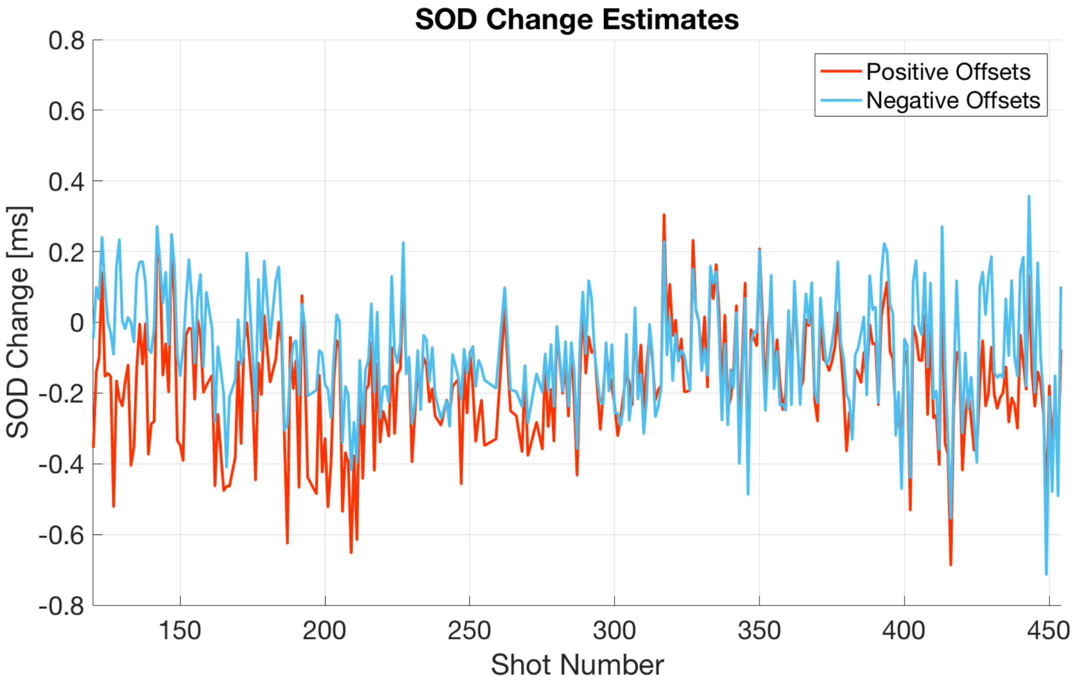

Figure 5.15: The estimated change in start of data delay between Snorre PRM 4 and 5 for positive offsets (red) and negative offsets (light blue). The estimates are found with the TSCI method.

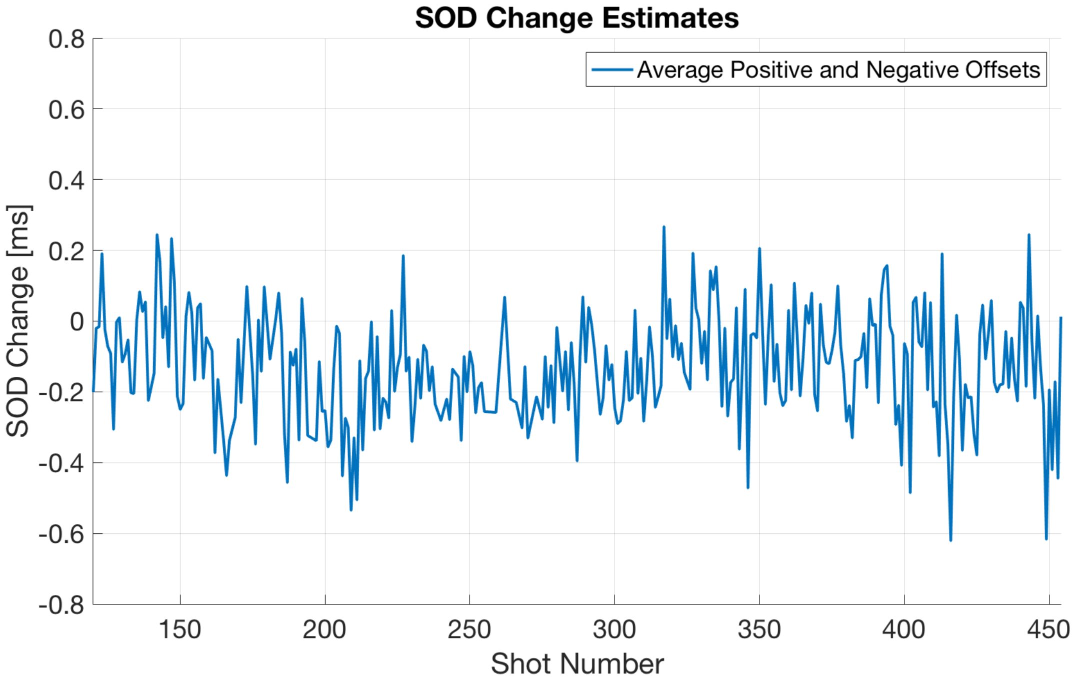

Figure 5.16: The average of the start of data delay change for positive and negative offsets between Snorre PRM 4 and 5.

Chapter 6

Discussion

This chapter contains the discussion of the results in Chapter 5. First, the discussion will be focused on the results from the tests of the TSCI method in Section 5.1 and 5.2. Then the results of water velocity and tidal change estimation of the Snorre data in Section 5.3 will be discussed, before possible improvements and the assumptions of the TSCI method are examined.

6.1 Realistic Subsurface Model and Seismic

The results in Section 5.1 indicate that the TSCI method based on the simple raytrace model works well for estimating both the velocity and tidal changes for a model with a realistic subsurface and for realistic seismic. The wave effects that not are being accounted for by the simple raytracing model do not seem to have a large effect on the results. This was also the case for the phase changes for post-critical angles. The reason why the phase changes not affect the time shifts or estimated water column changes by much, is most likely because the phase rotations and the time shift artifact created by the change in pulse shape will be relatively equal for both synthetic shot gathers. When extracting the time shifts between the shot gathers with the TSCI method, the time shift artifacts will be zeroed out so the original time shift created by the water column changes stays relatively unaffected.

Even though the results in Section 5.1 showed precise estimates, the velocity and tidal changes were not predicted perfectly. The time shift curves in Figure 5.2 and 5.5, along with the traces and cross correlations in Figure 5.3 showed that the quality of the time shift curves largely affects the resulting velocity and tidal change estimates. For the TSCI method to work properly, good quality time shift curves are needed. In order for the cross-correlation to result in good quality time shifts, the amplitude of the events to be cross-correlated need to be larger than the surrounding signal. As the amplitude of the multiples drops below the surrounding and interfering signal, the cross-correlation will result in wrong time shift estimates.

Reduced Precision for High Multiples

Common for the tests in Section 5.1, along with the tests shown in Appendix B.6, is that the precision reduced as the high order multiples were included in the calculations. Figure 6.1 shows the sea bottom reflection coefficient variation with offset for the direct wave for the assumed Snorre model in Figure 4.19 and Table 4.1. The direct wave reaches critical angle for offsets around 1800 meters. Since the high order multiples have more vertical propagation direction than the low order multiples for a given offset, only the direct wave and the 1st multiple will reach critical angle for the offsets below 6000 meters used in the test. The reflection coefficient for the rest of the multiples will stay low. The low reflection coefficients cause the multiples to loose amplitude for each reflection at the sea bottom. As a consequence, the amplitudes of the high order multiples, which are reflected many times at the sea bottom, will drop below the surrounding signal. As this happens, the cross-correlation fails to extract the actual time shift for the water column events and results in poor quality time shift curves and reduced accuracy of the estimated water column changes. As these high multiples are included in the calculations, they will destroy more than they will contribute to the precision of the estimates.

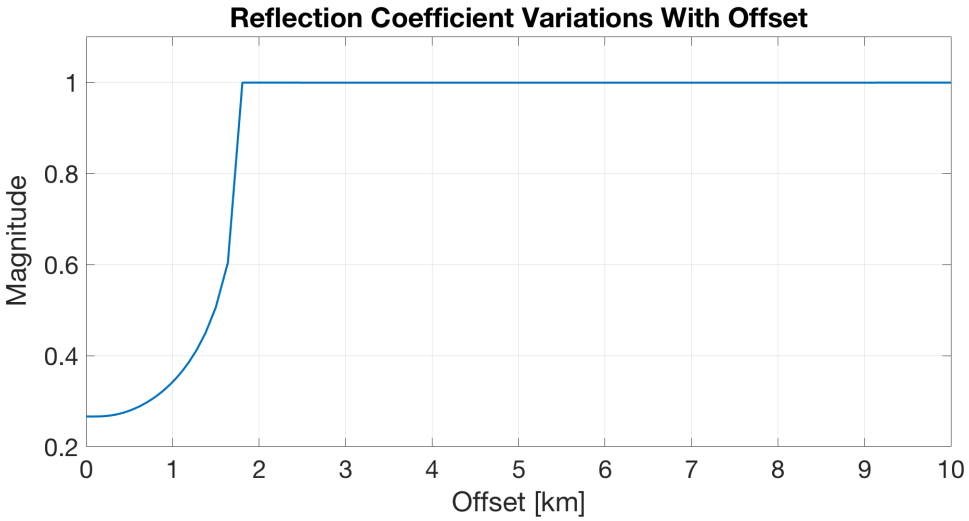

Figure 6.1: Reflection coefficient variation with offset for the direct wave for the assumed subsurface model at Snorre shown in Figure 4.19 and in Table 4.1, calculated with Zoeppritz equations. The y-axis represents the magnitude of the reflection coefficient. Based on the large critical offset seen in this figure, the assumed Snorre subsurface model used in this project might have slightly too low velocities just below the sea bottom compared to the real subsurface at Snorre.

In order to obtain best possible accuracy of the estimates with the TSCI method, the number of high order multiples to be included in the calculation and their corresponding offset intervals, need to be optimized. The test of the TSCI method's robustness to variations in subsurface models in Appendix B.6, shows that the multiple's strength and high-amplitude offset intervals largely depends on the subsurface model. Hence, to obtain accurate estimates of the water column changes, the offset intervals and the number of multiples need to be adjusted for each subsurface model/ area. This can be done by adjusting the minimum and maximum offset parameters, L_n and H_n, in the objective function in Equation 4.10 for the different multiples.

The critical reflections for the real Snorre data seen in Figure 4.16 occurs at shorter offsets than for the assumed Snorre subsurface model with the reflection coefficient variations shown in Figure 6.1. Therefore, the assumed subsurface model at Snorre used in the tests in Section 4.2 and 5.1 might have slightly too low velocities just below the sea bottom compared to the real subsurface at Snorre. However, even though the assumed subsurface model is not completely equal to the real subsurface at Snorre, it worked for testing the performance of the TSCI method for realistic seismic and realistic subsurface models.

Underestimation

As the error increased when the high order multiples were included in the calculations in Figure 5.1 and 5.4, the magnitude of the water column change became underestimated. The underestimation can be explained by interference. As interference occurs between the water layer multiples and the surrounding signal, the wave field becomes complex and it is difficult to separate the water column events from the interfering events. If the amplitude of the interfering event is larger than the amplitude of the water layer event, the maximum of the cross-correlation may correspond to the peaks of the interfering signal instead of the water layer events. Since the water layer events only have travelled in the water column, they have been more exposed to the water layer changes and more time-shifted than the interfering refractions and reflections from deeper boundaries. Hence, if the maximum of the cross-correlation corresponds to the interfering events instead of the water multiples, this will result in a lower time shift estimate. As seen by the expression for the relative time shift in Equation 2.6, the time shift is proportional to the velocity change and tidal change. Therefore, lower magnitude of the time shifts will result in lower estimates of the water velocity and tidal changes, which can explain the underestimation.

6.2 Robustness to Errors in Inversion Background Model

The results in Section 5.2.1 and 5.2.2 shows that the TSCI method is quite robust to errors in both the water depth and the water velocity used in the background model for forward modelling. For "reasonable" background model errors, the water column changes were estimated very precisely.

The synthetic time shift curves made by the forward modelling described in Section 4.1.5, calculates two sets of traveltimes based on the base velocity and water depth. If the base velocity or water depth is wrong, both traveltime sets will contain these errors. The reason why the TSCI method is so robust to errors in background model is that the forward modelled time shifts are found by the difference in the two sets of traveltimes. This difference is created by the velocity, tidal and SOD change, not by the background model errors. The errors in the background model will affect the estimates a little, e.g. a change in water depth will influence the magnitude of the time shifts caused by water velocity changes due to increased/ decreased traveltime. However, this influence is relatively low. The error in the background model, which is equal for both sets of traveltimes, will not be prominent.

This is a large advantage of the TSCI method. It is not necessary to have a background model with exact water depths and exact base velocity in order to obtain good estimates for the water velocity and tidal changes. Simplifications and approximations can be made. Hence, the 1D raytracing model with flat sea bottom should give good results even though the sea bottom at Snorre actually is dipping. This is also the case for the average receiver water depth approximation in the raytracing model, described in Section 4.1.5. An approximate absolute water velocity like the one found with the "Near Offset Method" in Appendix B.3, should also give good results. In the acquisition of 2D/3D seismic, the water velocity may vary across the line/ area due to differences in water depth and ocean streams. However, since the TSCI method is so robust to base velocity errors, good results should be obtained with the use of a single global base velocity in the background model.

Even though the TSCI method is very robust to errors in the background models, the results in Section 5.2 show clear and consistent trends of over and underestimation as the error in the estimates increased. These trends are explained in the following subsections.

Underestimation of Velocity and Tidal Changes for Too Deep Water Bottom

In Figure 5.6, the water velocity change estimates were estimated too low as the error in the background model water depth increased. This can be explained by the expression for time shifts caused by pure velocity changes ($\Delta z = 0$) in Equation 2.7, given again here:

$$\Delta t_{n,x} \approx -t_{n,x}\frac{\Delta v}{v}$$

During the inversion process, the forward modelling produces time shift curves as equal as possible to the time shift curves in the observed data. As the water depth in the background model is too large, the traveltime in the forward model, $t_{n,x}$, will be larger than the traveltime in the observed data. To produce the same time shifts as in the observed data, the velocity change has to reduce, resulting in an underestimated water velocity change. However, if the water depth is assumed too low, the opposite will happen. The traveltime in the background model reduces, and the velocity changes get overestimated.

The reason why the error in Figure 5.6 increases for increased multiple order is that the error in the traveltime also increases for increased multiple order. This because the multiples are affected by the water depth errors several times. As the error in the traveltime increases, the error in the estimated water velocity change also has to increase in order to make the forward modelled time shifts equal to the time shifts in the observed data.

The estimated tidal level changes in Figure 5.7 were also estimated too low as the error in the background model water depth increased. Since the tidal change is a vertical change, it will produce largest time shifts for vertical propagation directions. As the propagation direction gets closer to horizontal, the time shifts will reduce. Appendix B.7 shows that the time shifts created by a given tidal change are larger for a model with large water depth than for a model with shallow water depth. This is due to more vertical propagation direction as the water depth increases. If the background model contains a too large water depth, the magnitude of the tidal change has to reduce in order to produce the same time shift magnitude as in the observed data. This is the reason why the tidal changes in Figure 5.7 are underestimated. If the water depth in the background model had been too low, it would have been the other way around, and the tidal changes would have been overestimated.

The reason why the error in the tidal level estimates in Figure 5.7 reduced as the highest multiple order included in the calculations increased, is because increased multiple order results in a more vertical propagation direction, which reduces the error in the tidal change estimates. This is further explained in Appendix B.7.

Under and Overestimation with Wrong Base Velocity

The reason why the velocity change estimates with wrong base velocity in Figure 5.8, became slightly underestimated for too low base velocities and slightly overestimated for too high base velocities, can also be explained by Equation 2.7. The time shift is inversely proportional to the absolute velocity, while it is directly proportional to the velocity change.

If the absolute velocity, v, increases, the velocity change, Δv, need to be larger in order to keep the time shift fixed and equal the time shift in the observed data. The opposite happens as the absolute velocity decreases.

6.3 Water Velocity and Tidal Change Estimates Between Snorre PRM 4 and 5

The main results of this report, presented in Section 5.3, show consistent estimates of both the tidal level change and the water velocity change between PRM 4 and 5 by using the TSCI method to the Snorre data.

As shown in Figure 5.11, the estimated tidal change increased with shot number, approximately in the same manner as the tidal changes in the PIES measurements. In addition, the linear fit of the tidal change estimates matched the tidal changes from the PIES measurements really well. This is a good quality check that the TSCI method gives reasonable results, and increases the confidence in the estimated tidal changes.

The estimated water velocity change in Figure 5.14 shows a mean of -2.70 m/s and a standard deviation of ± 0.10 m/s. Compared to a water velocity of 1490 m/s, the standard deviation of 0.10 m/s only make up 0.0067%. This indicates that the standard deviation of ± 0.10 m/s is very low. As shown in Section 3.3, the average velocity difference between PRM 4 and 5 measured by the PIES was -3.27 m/s. Hence, the magnitude of the velocity difference estimated with the TSCI method was 0.57 m/s lower. It is hard to say which one is the most correct estimate. But the PIES are based on measurements from 2 locations, every 10th minute. The TSCI method uses measurements from 373 shots each including up to 233 receivers. Hence, the estimates obtained with the TSCI method is based on far more measuring points than the PIES measurements. In addition, the standard deviations for the PIES measurements, 1.738 m/s and 0.686 m/s for PRM 4 and 5 respectively, are way higher than the standard deviation obtained with the TSCI method. Compared to the PIES velocity measurements, the estimates obtained with the TSCI method seem to give more consistent results.

6.3.1 Why Estimates at Positive and Negative Offsets Differs

As seen in Figure 5.9, 5.10 and 5.12, the magnitude of both the tidal change and the water velocity change is estimated to be higher for positive offsets than for negative offsets. 2 different effects were investigated to try to explain the variations in estimates for positive and negative offsets:

- Rest errors in the symmetry correction.
- Different water depth for positive and negative offsets

The 2 effects are discussed in the following.

Rest Errors in the Symmetry Correction

A possible reason for the larger estimates for positive offset than negative offsets lies in the symmetry correction presented in Section 4.1.3. Even though the symmetry of the time shift curves for positive and negative offsets improved significantly after the symmetry correction, the two were not perfectly identical. There might exist some rest error in the symmetry correction that makes the time shifts for positive and negative offsets to differ. The velocity change estimates are very sensitive to the gradient of the time shift curve. If the gradient is a little steeper for positive than for negative offsets, this will result in higher velocity estimates for positive offsets than for negative offsets. The short offsets are most important for consistent tidal estimates. If the time shift curves for positive and negative offsets differ slightly at short offsets, this will result in differences in the tidal change estimates. Hence, rest errors in the symmetry correction is a likely reason for the difference between the estimates for positive and negative offsets. To optimize and improve the symmetry correction, e.g by optimizing the weighting of different offset intervals in Equation 4.4, might result in more consistent and correct estimates for positive and negative offsets.

Different Water Depth for Positive and Negative Offsets

As explained in Chapter 1, the uppermost parts of the water layer have largest velocity variations throughout a year. The velocity in the lowermost parts varies less. Since the sea floor at Snorre has a dip, the time shifts estimated at positive offsets are based on receivers located in more shallow water than the receivers the estimates for negative offsets are based on. This means that the estimates at positive offsets are based on a water column with a larger proportion of large velocity changes than the estimates at negative offsets. This is illustrated in Figure 6.2. The red area highlights the positive offsets where a larger percentage proportion of the water layer is located in the zone with most velocity changes compared to the negative offsets in the blue area. This may explain why the magnitude of the velocity change at positive offsets are larger than the magnitude of the velocity change at negative offsets.

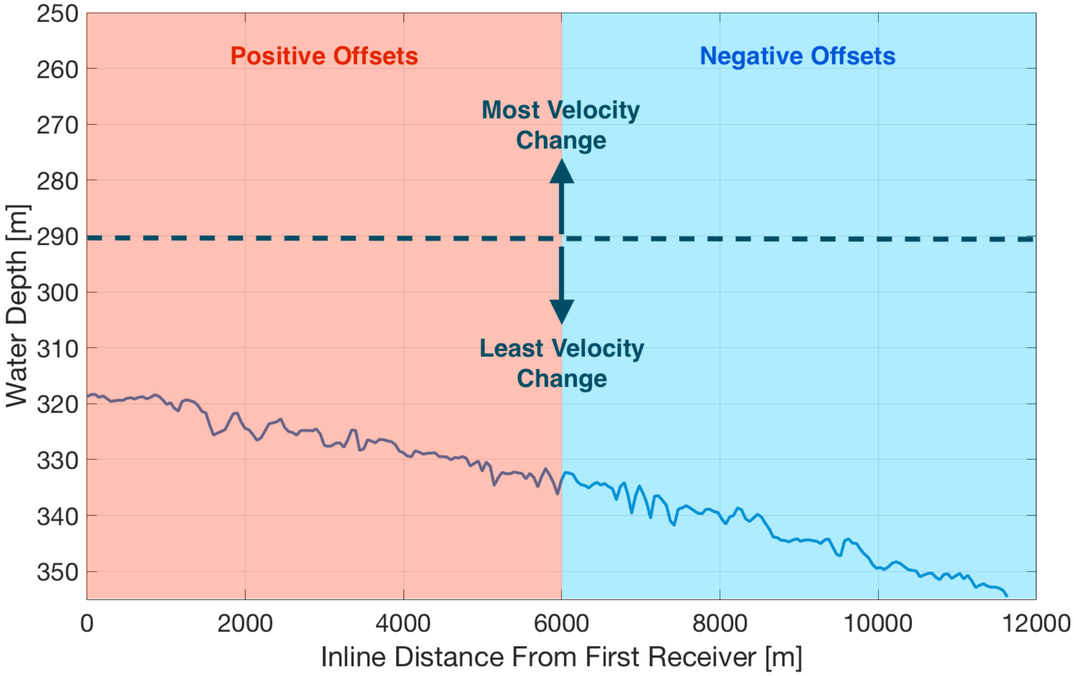

Figure 6.2: Illustration of the difference in water depth for positive and negative offsets. The blue curve shows the water depth measured in the receivers along receiver line 27 at Snorre (same as in Figure 3.5). Throughout a year, most velocity changes happen to the uppermost parts of the water layer, while least changes happen to the lowermost part of the water layer. The estimates at positive offsets are based on a water column with a higher proportion of large velocity variations than the estimates at negative offsets.

The variation in water depth can also explain the trend of slightly decreased magnitude for the estimated velocity change with increased shot number, seen for both positive and negative offsets in Figure 5.12. Low shot numbers are located in the area of shallow water, to the left in Figure 6.2. High shot numbers are located in the area of deeper water, to the right in Figure 6.2. Since only receivers up to 6000 meters offset were used in this project, the estimates for high shot numbers are based on the receivers located in deeper water than the estimates at low shot numbers, resulting in a lower magnitude of the velocity change for high shot numbers than for low shot numbers.

6.3.2 Unstable Estimates at Each End of the Shot Line

Both the estimates for tidal and water velocity change were most unstable and varying for shot numbers located at each end of the shot line. This is especially seen in Figure 5.9 and 5.12, where the estimates for positive offsets varies a lot for low shot numbers, while the estimates for negative offsets varies a lot for large shot numbers. The large variation in the estimates for these shot numbers may be due to a combination of:

- Few traces to base the calculations on
- Poor quality of the 2$^{\text{nd}}$ multiple at short offsets

Few Traces

For low shot numbers, the number of receivers located at positive offsets is low. For high shot numbers, the number of receivers located at negative offsets is low. Hence, the estimates for positive offsets at low shot numbers and negative offsets at high shot numbers are based on fewer traces than the rest of the estimates. As shown in Section 4.1.7 and Figure 4.15, the velocity and tidal change estimates are largely affected by the shape of the time shift curve. Fewer traces make the shape of the time shift curve more uncertain, which give rise to larger variation in the estimates.

Due to the lack of traces, the shots located at each end of the shot line are also especially exposed to errors in the symmetry correction, described in Section 6.3.1. As only traces at short offsets are available, the quality of the symmetry correction reduces.

The velocity change estimates for the shots located at the each end of the shot line in Figure 5.12 varies more than the corresponding tidal change estimates in Figure 5.9. This might be due to that the velocity change estimates are largely affected by the gradient of the time shift curves, especially at large offsets. However, for positive offsets at low shot numbers and negative offsets at high shot numbers, only the near-offset traces are available. The uncertainty of the velocity change estimates for these shots will increase, resulting in large variations in the estimates. The tidal change estimates are most sensitive to the near-offset traces, and will stay more stable.

Poor Quality of 2nd Order Multiple at Short Offsets

As seen in Section 4.1.8 and Figure 4.17, the direct wave and the 1st multiple have good strength factors at short offsets. However, this is not the case for the 2nd multiple, where the strength factor only becomes 1 for offsets above 3200 meters. Since the tidal change is most pronounced at short offsets in the time shift curves, the 2nd multiple was in this project included for offsets as low as 1500 meters in order to obtain good estimates of the tidal change. However, at these short offsets the quality of the time shift curves for the 2nd multiple might be poor. At each end of the shot line where only the short offsets are available, the inclusion of the 2nd multiple might be more destructive than constructive, as no high-quality, large offset time shifts are present to "guide" the inversion. This might have resulted in less precise estimates of the water column changes and more variations.

6.3.3 Dilemma for Precise Tidal Change Estimations

The issue with the quality of the 2nd multiple described above, is a good example of the dilemma that occurs in the effort of optimizing the tidal change estimation. Precise estimates of the tidal changes favour the inclusion of many high order multiples in the calculations. The higher the multiple order, the more times the multiple has propagated through the water layer and been exposed to the tidal changes. Hence, the precision of the tidal change estimates should be improved by including many multiples in the calculations.

Since the magnitude of the time shifts caused by tidal changes reduces with offset, precise estimates of the tidal changes also favour short offsets. However, as shown in Section 4.1.8, the high order multiples have weak amplitudes compared to the surrounding signal at short offsets. This results in reduced quality of the time shift curves at short offsets.

This gives rise to a dilemma. Precise tidal change estimations favour both high multiple orders and short offsets. But, the high order multiples have weak amplitudes at short offsets. This makes the measured time shifts at short offsets uncertain, and the inclusion of the high order multiples at short offsets might be more destructive than constructive in order to obtain accurate tidal change estimates. Therefore, it is important to find an optimal threshold between the number of high order multiples included and how much of the short offset part of the multiples' time shift curve that should be included in the TSCI method.

6.3.4 Source of Errors: Seismic Interference

As shown in Section 3.1 and Figure 3.4 there was some seismic interference during the acquisition of PRM 4. The seismic interference was especially prominent for offsets around 6500 - 7800 meters, highlighted by the red ellipse in Figure 3.4. The time shift curve for the 1st order multiple, representing the same shot as in Figure 3.4, is shown in Figure 6.3. The time shifts in Figure 6.3 increases relatively smooth up to 6500 meters. However, after 6500 meters, lots of spikes occur. The largest spikes seem to disappear after 8000 meters. This is almost exactly the same offset interval as where the seismic interference occurs in Figure 3.4. Therefore, the spikes were interpreted to be caused by the seismic interference. Since the seismic interference was present throughout the PRM 4 dataset, it is likely that the interference can be the source of some of the large anomalies that occurred for time shift curves of other shot gathers as well. The seismic interference might have reduced the precision of the estimated water column changes at Snorre presented in this report.

Figure 6.3: Raw time shift curve for the 1^{st} order multiple from the same shot gather as in Figure 3.4. Note the large spikes for 6500 - 7800 meters offset. This might be caused by seismic interference, with occurs in the same offset interval, highlighted by the red ellipse in Figure 3.4.

6.4 Potential for Improvement

The TSCI method described in this report is not yet perfect. In addition to the symmetry correction described in Section 6.3.1, there are several parts that can be improved and developed further. Some of these are discussed in this section.

6.4.1 Source Depth Correction

In this project, the source depth given in the headers of the Snorre data was assumed to be correct, and potential errors in the source depth were neglected. However, the value of the source depth given in the headers was constant for all shots and did not account for variations caused by waves and ocean streams that pulled the source arrays up and down during the surveys. Because of this, there existed differences between the source depths in the two vintages. Differences in source depth result in the effective distance from the source to the receiver to differ between the vintages, which can create significant errors in the time shifts curves as shown in Section 4.1.3. This increase the uncertainty in the estimates of the water column changes between Snorre PRM 4 and 5 given in this report.

In Figure 5.9 and 5.11, the estimated tidal changes show high-frequency oscillations in addition to the long periodic increase in tidal level with shot number. As discussed in Section 5.3, this may be due to wave action on the sources. To introduce a source depth correction in the TSCI method may remove some of the high-frequent oscillation and make the estimated tidal change curve more smooth.

The effect of a source depth difference between the vintages is exactly equal to a tidal change, as the effective water depth changes in both cases. Hence, it is impossible to distinguish the time shifts created by a source depth difference and a tidal level change by only using the direct wave time shifts. However, by utilizing the time shift curves of the multiples, it should be possible to separate the two effects. The multiples, which have propagated through the water layer n times, have also been exposed to the tidal changes between the vintages n times. And since the source depth difference only will affect the traveltime of the multiples once, it should be possible to separate the two effects by including several multiples in the calculations. By introducing the source depth correction as another variable in the TSCI method, the precision and stability of the estimates are expected to increase as long as several multiples are included in the calculations.

6.4.2 Arrival Time Prediction and Window Length

As discussed in Section 6.2, the TSCI method is relatively insensitive to errors in the background model used for forward modelling during the inversion. However, it is important to have a precise model in order to predict the correct arrival times for the water column events. Since the sea bottom at Snorre is dipping, the reflection angles at the sea bottom will change for each reflection. As a consequence, the traveltime for the multiples, which have been reflected several times at the dipping sea floor, will differ from the traveltimes predicted with the 1D raytracing model used in this project. As seen in Figure 3.5, the dip of the sea bottom at Snorre is very gentle. Since the maximum offset and multiple order included in this project was 6000 meters and 2nd order respectively, the arrival times predicted with the 1D raytracing model became relatively correct for the events included in this project. However, for larger offsets and higher multiple orders, the precision of the traveltimes predicted with the 1D raytracing model was low. If higher multiple orders and larger offsets are to be included in the method, an arrival time prediction model that accounts for the dip and variations along the sea floor, needs to be incorporated. Another option is to pick the traveltimes of the water column events manually from shot gathers.

Since the 1D raytracing model used for the traveltime prediction in this project only gave approximate traveltime predictions, the correlation window length needed to be large enough to allow for some uncertainties in the predicted traveltimes. In this project, a window length of 40 ms was used to make sure the water column events was "captured" before cross-correlation was performed. However, this large window can have created some additional noise and errors in the time shift curves. This is illustrated in Figure 6.4. The large red window captures several events, while the event that is to be cross-correlated is the one inside the light blue window. As several events are present inside the red correlation window, the cross-correlation will become more complex, which might result in the calculation of wrong time shifts. With a more precise prediction of the traveltimes, the window length can be reduced to the light blue window, which only incorporates the water column events that are to be cross-correlated. This will result in a more simple cross-correlation and increase the quality of the calculated time shifts.

To summarize the discussion above, a traveltime prediction model that incorporates the dip along the sea floor would be beneficial in two ways:

- Higher order multiples and larger offsets can be included in the method to give more confident estimates
- The window length for cross-correlation can be reduced so the quality of the time shift curves increases, resulting in more precise estimates

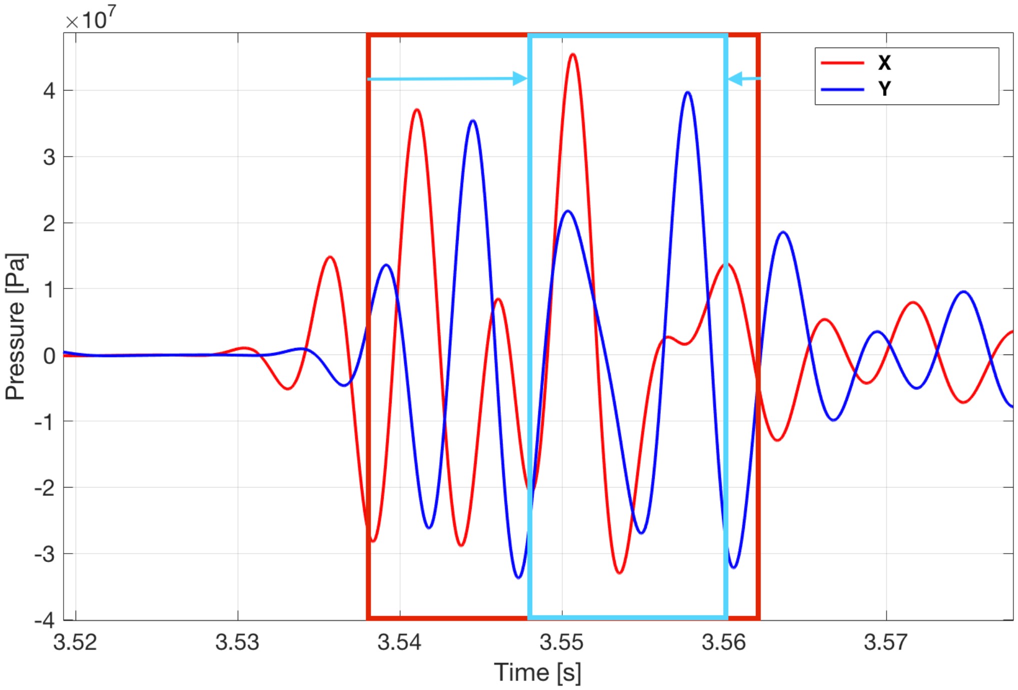

Figure 6.4: Figure illustrates 2 time-shifted traces, X and Y, along with two different correlation windows. Inside the red correlation window, several events are present. If precise arrival times for the desired events are obtained, the window length can be reduced to only incorporate the events that are to be cross-correlated, which is the large red and blue peaks inside the light blue window in this figure. This may increase the precision of the time shift calculations.

6.4.3 Outlier Removal and Smoothing

As described in Section 4.1.7, the estimated velocity and tidal changes are largely affected by the shape of the time shift curves. Hence it is important to remove all outliers that can reduce the quality of the measured time shift curves. The outlier removal and smoothing performed in this project, described in Appendix B.4, did give fairly good results, but the results were not perfect. There are improvement areas in making the outlier removal better. One suggestion is a curve fitting approach, where a curve with the approximate shape of the time shift curves is fitted to the time shift data. This may make the time shift curves more smooth and increase the precision of the estimates.

6.5 Assumptions for the TSCI Method

The TSCI method is based on several assumptions, which need to be valid in order for the method to give good results. Some of these are discussed in this section.

Same Source Signature for All Vintages

For the TSCI method to work, the source needs to emit the same source signature in the different vintages. This is a fairly good assumption as the sources in the 4D seismic vintages are made to replicate each other. However, if one of the air guns in the source array fails, this might result in source signature differences which can create errors in the estimated time shifts between the vintages. No such errors were reported for Snorre PRM 4 or 5.

Same Location of the Receivers for All Vintages

One of the main assumptions of the TSCI method is that the receivers are located at the same place in both vintages. As the receivers have a fixed location on the sea floor, this is a good assumption.

The receiver coordinates given in the seismic header may contain errors. However, with reasonable certainty, the receiver position errors are below ± 10 meters. As discussed in Section 6.2, a background model with ± 10 meters wrong water depth does not affect the resulting water column change estimates noteworthy. The same is true for errors of ± 10 meters in the horizontal direction. Hence, as long as the receivers are located at the same place in both vintages, errors in the exact receiver positions can be neglected and will not affect the resulting estimates of the water velocity and tidal change by much.

No Bending of Rays at Large Offsets

The raytracing method used for the forward modelling and to predict the arrival times in this project assumes that the waves behave like straight rays. However, this is not always the case as the water velocity variations with depth cause the rays to bend. Appendix B.8 shows a raytracing of an approximated velocity profile of the PRM 4 TS Dip measurements, and the traveltime of the bent rays are compared to traveltimes of the corresponding straight rays. At small offsets, the ray bending does not create large traveltime differences from a straight ray. However, for large offsets the traveltime of the bent and the straight rays differ significantly. In Figure 3.10 the TS Dip water velocity profile shows much higher velocities in the uppermost part of the water layer for PRM 4 than for PRM 5. This will lead to differences in the bending of the rays in the two vintages, which may create additional time shifts between PRM 4 and 5 at the largest offsets included in this project. Since the estimation of the water velocity change is sensitive to the large offset time shifts, the ray bending might have slightly affected the velocity change estimates presented in this report. If the TSCI method gets extended to include even larger offsets in the future, the effect of the ray bending will increase significantly and needs to be corrected for.

Chapter 7

Conclusion and The Way Forward

7.1 Conclusion

The goal of this master thesis was to develop a method to estimate the water velocity and tidal changes between 4D seismic vintages, from the seismic data alone. This goal has been fulfilled and the TSCI method was developed. The TSCI method utilizes inversion based on time shift curves and is based on 2 main steps:

- Time shift curves are found by a trace-by-trace cross-correlation of the water column events in two 4D seismic vintages.
- Inversion is performed based on the time shift curves, using a 1D raytracing model for calculating the forward response. The result is estimates of the changes in water velocity, tidal level and start of data delay between the vintages.

Even though the 1D raytracing model used for the forward modelling only accounted for the P-waves in the water layer, the results in Section 5.1 showed that the TSCI method gave good results and proved to work for both realistic seismic and a realistic subsurface models. In addition, the TSCI method is robust to variations in both the subsurface velocities and the subsurface layer thicknesses.

From the test of the TSCI method in Section 5.2, it can be concluded that the TSCI method is robust to errors in the background model used for forward modelling. If the water depth or the base water velocity is assumed wrong, this will lead to some errors in the estimated water column changes. However, for reasonable magnitudes of the background model errors, the errors in the estimates are negligible. The background model does not need to be 100 % correct for the TSCI method to give good results. This is a large advantage of the TSCI method.

The TSCI method was used to estimate the water velocity and tidal changes between Snorre PRM 4 and 5, and the results in Section 5.3 showed consistent estimates. The standard deviation of the estimated velocity changes was low, and the estimated tidal changes had a good match with other tidal predictions.

In order to obtain best possible results with the TSCI method, it is a prerequisite to have good quality of the input seismic data, precise predictions of the arrival times of the water column events and to correct for differences in the source positions:

- **High Qualiy Input Data:** The quality of the input seismic data decides the quality of the time shift curves, which again decides the precision of the estimated water column changes. To ensure good quality data, the amplitude of the water column events included in the calculations need to be larger than the amplitudes of the surrounding signal. This ensures correct cross-correlation and correct time shift estimation. Each water column event will have a specific offset interval of high amplitudes, decided by critical angle and the source ghost interference. High-quality data is ensured by only including the water column events inside their "high amplitude interval". This interval depends on the water depth and the subsurface parameters, and will because of this vary from area to area.

- **Precise Arrival Time Predictions:** If the arrival times are predicted accurately, the window length used for cross-correlation can be reduced to only incorporate the events that are to be cross-correlated. This increases the likelihood of correct time shift calculation during the cross-correlation and results in high quality of the time shift curves.

- **Source Position Difference Corrections:** In order to get consistent and correct results with the TSCI method, it is crucial to correct for differences in source position between the vintages that occur as waves and currents act on the sources during the acquisition of the surveys.

There are several parts of the TSCI method that can be improved. Both the symmetry correction, outlier removal and the arrival time prediction can be developed further. In addition, corrections for the source depth differences might result in even more precise estimates.

Due to the dipping sea bottom at Snorre, the 1D raytracing model used in this project limited the offsets and multiple orders to be included in the TSCI method for the Snorre data. However, the precision of the estimates presented in this report is expected to increase with the inclusion of even higher multiple orders and offsets.

7.2 The Way Forward

The TSCI method can be developed further. First of all, as discussed in Section 6.4.2, a more advanced raytracing model which accounts for the variations along the sea floor will give better predictions of the arrival times of the water column events. As the arrival times are predicted more precisely, the window length used for the cross-correlation can be reduced to only incorporate the events that are to be cross-correlated. This can result in increased quality of the time shift curves and more accurate velocity and tidal change estimates. A raytracing model which accounts for the variations along the sea floor will also allow for higher order multiples to be included in the calculations. This can also result in more accurate results.

If higher multiples are included in the TSCI method, larger offsets are needed as well. This is because the higher order multiples have their "high amplitude interval" at larger offsets, as shown in Section 4.1.8. As discussed in Section 6.5, the effect of ray bending increases for large offsets, which may reduce the precision of the estimated water column changes. If larger offsets are included, a ray bending correction will be needed in order to obtain precise estimates. In this project, only the pressure data was used. However, if larger offsets are included to the TSCI method, the radial particle velocity component can be useful, as most of the energy will be in the radial direction at large offsets. At least for the low order multiples. This might enhance the signal to noise ratio for the multiples, making the cross-correlation and time shift curves more correct.

By using the particle velocity data it will also be possible to separate the up-going wave field from the down-going wave field. The up-going wave field has been reflected at boundaries in the subsurface and contains lots of information about the geology. The down-going wave field contains the water column events along with the water layer multiples of the subsurface reflections. By separating the two wave fields and only use the down-going wave field, lots of "noise" will be removed from the time shift estimation, which may increase the quality of the time shift curves.

The symmetry correction described in Section 4.1.3 is a crucial step for obtaining consistent and precise estimates of the water column changes. As discussed in Section 6.3.1, the symmetry correction may contain some rest errors and can be improved, e.g. by optimizing the weighting of different offset intervals in Equation 4.4. This may result in even more accurate estimates.

As discussed in Section 6.4.1, the source depth differences caused by wave action and ocean streams might have created some errors in the estimates presented in this report. To add a correction for the source depth differences as an extra variable in the TSCI method, may result in more consistent results, especially for the tidal change estimates.

To utilize the estimates from the TSCI method optimally, the way the water velocity and tidal corrections are performed might need to be modified. The velocity and tidal corrections mentioned in Chapter 1 and in Appendix B.1 do only correct for the time shift between the primaries, not the multiples. The multiples have to be removed by an independent methodology, but the multiples are newer completely removed. This results in residual time shifts that increase with traveltime. By using the estimates from the TSCI method together with a model based multiple removal method, might lead to better results. In such a model based approach, the water layer multiples can be estimated from a model of the water layer and then be subtracted from the seismic data. By adjusting the water layer model with the water velocity change and tidal change found with the TSCI method, the model of the water layer can be used to remove multiples from all the 4D vintages. All the multiples will then be treated with the same precision, which may reduce the difference between the vintages. Evaluation of the optimal use of such a model based multiple removal method was beyond the scope of this Master's Thesis. But this is a suggestion for further work in order to utilize the results of the TSCI method optimally.

Bibliography

Åsli, H. (2002). Effects of changes in water velocity on time-lapse seismic data – a method for multiple attenuation? Master's thesis, Norwegian University of Science and Technology.

Bertrand, A. and MacBeth, C. (2003). Seawater velocity variations and real-time reservoir monitoring. *The Leading Edge*, 22(4):351–355.

Bouchon, M. (1981). A simple method to calculate green's functions for elastic layered media. *Bulletin of the Seismological Society of America*, 71(4):959–971.

Bracewell, R. N. (2012). *Fourier Analysis and Imaging*. Springer Science and Business Media.

Červenỳ, V. and Pšenčík, I. (2011). Seismic, ray theory. In *Encyclopedia of Solid Earth Geophysics*, pages 1244–1258. Springer.

Dietrich, M. (1988). Modeling of marine seismic profiles in the tx and τ-p domains. *Geophysics*, 53(4):453–465.

F. Jones (2007). Inversion theory: Model norms, data misfit and non-uniqueness. `https://www.eoas.ubc.ca/ubcgif/iag/tutorials/invn-theoryintro/norms-misfit.htm`. [Online; accessed 20-June-2017].

Fried, J. and MacKay, S. (2001). Dynamic corrections for water velocity variations: A nova scotia case history. *GSEG Recorder, Oct*.

Glover, F. (1998). A template for scatter search and path relinking. *Lecture notes in computer science*, 1363:13–54.

Grebogi, C., Ott, E., Pelikan, S., and Yorke, J. A. (1984). Strange attractors that are not chaotic. *Physica D: Nonlinear Phenomena*, 13(1-2):261–268.

Hadziioannou, C., Larose, E., Coutant, O., Roux, P., and Campillo, M. (2009). Stability of monitoring weak changes in multiply scattering media with ambient noise correlation: Laboratory experiments. *The Journal of the Acoustical Society of America*, 125(6):3688–3695.

Hale, D. et al. (2006). Fast local cross-correlations of images. *76th Annual International Meeting*, pages 3160–3163.

Hatchell, P., Wills, P., and Didraga, C. (2008). Identifying and removing effects of multiples on time-lapse interpretation at vahall. *First Break*, 26(5).

Henry, B., Butt, S., Igoe, M., Jupp, R., and Desrues, K. (2004). Correction of tidal statics using new generation differential gps technology. *Petex: Poster session*.

Kartverket (2016). *Tidevannstabeller for den Norske Kyst med Svalbard samt Dover, England – 2017, 80. årgang*. Kartverket.

Kennett, B. (1974). Reflections, rays, and reverberations. *Bulletin of the Seismological Society of America*, 64(6):1685–1696.

Lacombe, C., Schultzen, J., Butt, S., and Lecerf, D. (2006). Correction for water velocity variations and tidal statics. In *SEG Technical Program Expanded Abstracts 2006*, pages 2881–2885. Society of Exploration Geophysicists.

Landrø, M. (2011). *Seismic Data Acquisition and Imaging*. Norwegian University of Science and Technology.

Landrø, M. and Stammeijer, J. (2004). Quantitative estimation of compaction and velocity changes using 4d impedance and traveltime changes. *Geophysics*, 69(4):949–957.

MacKay, S., Fried, J., and Carvill, C. (2003). The impact of water-velocity variations on deepwater seismic data. *The Leading Edge*, 22(4):344 – 350.

Oldenburg, D. W. and Li, Y. (2005). Inversion for applied geophysics: A tutorial. *Near-surface geophysics: SEG*, pages 89–150.

Oljedirektoratet (2017). Snorre Field. http://factpages.npd.no/FactPages/default.aspx?nav1=field&nav2=PageView$%$7CAll&nav3=43718. [Online; accessed 28-May-2017].

Statoil (2017). Snorre. https://www.statoil.com/en/what-we-do/norwegian-continental-shelf-platforms/snorre.html. [Online; accessed 29-May-2017].

Tarantola, A. (2005). *Inverse problem theory and methods for model parameter estimation*. SIAM.

Teien, O. M. (2016). Analysis of time shifts caused by water column changes.

Ugray, Z., Lasdon, L., Plummer, J., Glover, F., Kelly, J., and Martí, R. (2007). Scatter search and local nlp solvers: A multistart framework for global optimization. *INFORMS Journal on Computing*, 19(3):328–340.

Wang, K., Hatchell, P., Udengaard, C., Craft, K., and Dunn, S. (2012). Direct measurement of water velocity and tidal variations in marine seismic acquisition. In *SEG Technical Program Expanded Abstracts 2012*, pages 1–5. Society of Exploration Geophysicists.

Xu, S. and Pham, D. (2003). Global solution to water column statics: A new approach to an old problem. In *SEG Technical Program Expanded Abstracts 2003*, pages 1885–1888. Society of Exploration Geophysicists.

Zhang, X., Zhang, Z., Xu, T., Bai, Z., and Harris, J. M. (2012). Phase shift approximation for the post-critical seismic wave. *Journal of Geophysics and Engineering*, 9(5):482.

Appendix A

Acronyms and Expressions

A.1 Acronyms

NMO: Normal Move Out

PIES: Pressure Inverted Echo Sounder

PRM: Permanent Reservoir Monitoring

RMS: Root Mean Square

SKB: Synthetic Seismograms with the Kenneth-Bouchon Approach

SOD: Start Of Data Delay

TS Dip: Temperature Salinity Dip

TSCI: Time Shift Curve Inversion

A.2 Explanations of Used Expressions

First Receiver:

The receiver to the far west at receiver line 27 at Snorre

First Shot:

The shot to the far west on the given shot line for Snorre PRM 4

Positive Offsets:

Offsets corresponding to the receivers to the west of the source location

Negative Offsets:

Offsets corresponding to the receivers to the east of the source location

Shot Gather Pair:

2 shot gathers from different 4D vintages, representing approximately the same shot location

Shot Number:

Ranges from 1 to 566, representing the different shot gather pairs in Snorre PRM 4 and 5

Start of Data Delay:

Lag in time between the measured firing time and the actual firing time in the source

Trace Pair:

2 traces from 2 different 4D vintages representing approximately the same source and receiver locations

Water Column Changes:

Water velocity and tidal level changes between 4D seismic vintages

Water Column Events:

The direct wave and the water layer multiples of the direct wave

Appendix B

Additional Information, Methods, Tests and Results

B.1 Corrections for Water Column Changes

For receivers at an offset x, the arrival time for the seabed reflection can be described as

$$t(x) = \sqrt{\frac{(2z)^2 + x^2}{v^2}} = \sqrt{t_0^2 + \frac{x^2}{v^2}} \tag{B.1}$$

where z is the water depth, v is the water velocity and t_0 is the zero offset traveltime.

As the tidal level changes between two surveys, but the water velocity stays the same, only the water depth z (and t_0) in equation B.1 will change. The curvature of the hyperbolas will then stay the same, but the hyperbolas get shifted up/down Lacombe et al. (2006). If the tidal level change is known, corrections for the tidal change can be performed to NMO corrected data by a simple offset independent time shifts Lacombe et al. (2006).

If the water velocity changes between two surveys, but the tidal level stays the same, both the t_0 and the curvature of the hyperbolas will change, causing a time shift that varies with offset. A constant time shift correction is not sufficient to correct for the water velocity changes, and an offset-dependent correction needs to be used Lacombe et al. (2006).

Lacombe et al. (2006) presents a method for correction of the velocity changes. The method is based on shifting all the 4D vintages to a common reference velocity. The method consists of the following steps:

1. The water velocity, V, is measured directly from the RMS velocities in each vintage.
2. The data gets NMO corrected with this measured RMS velocity.
3. Let the water depth be z, the two-way zero offset traveltime can be expressed as $t_{0Init} = \frac{2z}{V}$. By changing V with a reference velocity, V_{ref}, the new two-way zero offset arrival time becomes $t_{0Final} = \frac{2z}{V_{ref}}$. The correction can be expressed as $\Delta t = t_{0Final} - t_{0Init} = t_{0Init}(\frac{V}{V_{ref}} - 1)$. This correction is applied to the NMO corrected data.
4. After the time shift correction, a reverse NMO correction based on the reference velocity is applied to the data.

This process is done for all vintages, which re-aligns the primaries in the 4D vintages to a constant water velocity, and a common datum Lacombe et al. (2006). However, this will only correct for the primary reflections. The multiples, which has propagated through the water layer several times, will not be corrected with this approach. The multiples need to be removed by other methods.

B.2 Pressure Inverted Echo Sounders

PIES is an abbreviation for "Pressure Inverted Echo Sounder". As indicated by the name, the PIES contains a pressure sensor along with an Inverted Echo Sounder. The PIES is deployed on the sea floor Wang et al. (2012). The pressure sensor measures the hydrostatic pressure and converts this to depth with the use of Equation B.2.

$$h = \frac{P}{\rho g} \tag{B.2}$$

P is the measured pressure, g is the gravitational acceleration, h is the water depth and ρ is the water density. To obtain the correct water depth, the sea surface air pressure has to be subtracted from the measured pressures in the PIES. However, this can lead to some errors as the air pressure often are measured some distance away from the actual PIES location Wang et al. (2012).

The inverted echo sounder sends acoustic waves up towards the sea surface, where they become reflected downwards again. The PIES measures the traveltime the acoustic wave uses to go up to the surface and down again. The vertical average velocity in the water column can be calculated from the measured traveltime combined with the water depth measurements performed by the pressure sensor Wang et al. (2012). The principle behind the PIES is illustrated in Figure B.1.

As the PIES measures the water velocity by sending waves upwards, it measures only the average velocity through the water layer. It does not record any velocity variations along the water column. However, the PIES can record lateral variations in the water velocity if multiple PIES are located at different locations on the sea floor. If the sea floor is dipping, it may be possible to invert for a water velocity profile Wang et al. (2012)

Figure B.1: Illustration of the principle behind the PIES. The PIES is deployed on the sea floor and emits acoustic waves. It measures the pressure and two-way traveltime, and calculates from this the water depth and the vertical average water velocity. The figure is acquired from Wang et al. (2012).

Wang et al. (2012) describes a correlation between spikes in the PIES measured water velocities and the wind speed. As the wind speed rises above ≈ 10 m/s, significant spikes occur in the velocity measurements. Their conclusion was that high wind speeds creates ripples and bubbles in the shallowest parts of the water layer, which scatters the acoustic wave field emitted from the PIES, and reflects it back to the sea bottom before the wave reaches the sea surface. Hence, the travel time reduces and the water velocities get shifted towards higher values.

B.3 Near Offset Method - Absolute Water Velocity

The "Near Offset Method" is a method to estimate the absolute water velocity. This section describes the method and the results of using the near offset method on Snorre PRM 4 and 5. The results from PRM 4 was used as the base velocity in the TSCI method in this project. The near offset method described here is slightly modified from the original method developed by Nigel Moyle, Principal Geophysicist at Statoil.

The method is based on traces representing source-receiver pairs with less than 30 meter offset. The method does not take the tides into account and assumes that tidal corrections are correctly performed to the data, so all timing differences between the two surveys are pushed into the water velocity changes or a constant SOD delay.

The method assumes that the water depth and the offset for the traces are known. The method also assumes locally horizontal seabed between the source and the receiver, and that the relationship between the traveltime for the direct wave and the first multiple simply is the ratio of the distances travelled by the two events. This removes the dependency of the water velocity.

The travelled distances for the direct wave and the first multiple can be described with Equation B.3 and B.4 respectively, and is illustrated by the orange (R_D), and red (R_{1M}) rays in Figure B.2. Figure B.2 also shows how the R_{1M} in Equation B.4 is calculated with the use of a triangle with catethi's x and $3z - z_s$.

$$R_D = \sqrt{x^2 + (z - z_s)^2} \tag{B.3}$$

$$R_{1M} = \sqrt{x^2 + (3z - z_s)^2} \tag{B.4}$$

z is the water depth measured at the receiver, x represents the horizontal source-receiver offset, and z_s the source depth.

The theoretical expression for the traveltime of the direct wave is

$$t_D = \frac{R_D}{V} + SOD \tag{B.5}$$

and for the first multiple, it is

$$t_{1M} = \frac{R_{1M}}{V} + SOD \tag{B.6}$$

where the SOD represents the start of data delay and V is the water velocity. By subtracting Equation B.5 from Equation B.6 the SOD's will be cancelled.

$$t_{1M} - t_D = \frac{R_{1M}}{V} + SOD - \frac{R_D}{V} - SOD \tag{B.7}$$

By solving Equation B.7 for the velocity, Equation B.8 is obtained, which is insensitive to the SOD delay.

$$V = \frac{R_{1M} - R_D}{t_{1M} - t_D} \tag{B.8}$$

For each of the traces corresponding to offsets less than 30 meters, the travel times for the direct wave, t_D, and the first multiple, t_{1M}, were picked manually from the seismic. The corresponding travel distances for the two events were calculated with equation B.3 and B.4. The absolute water velocity was then found by Equation B.8.

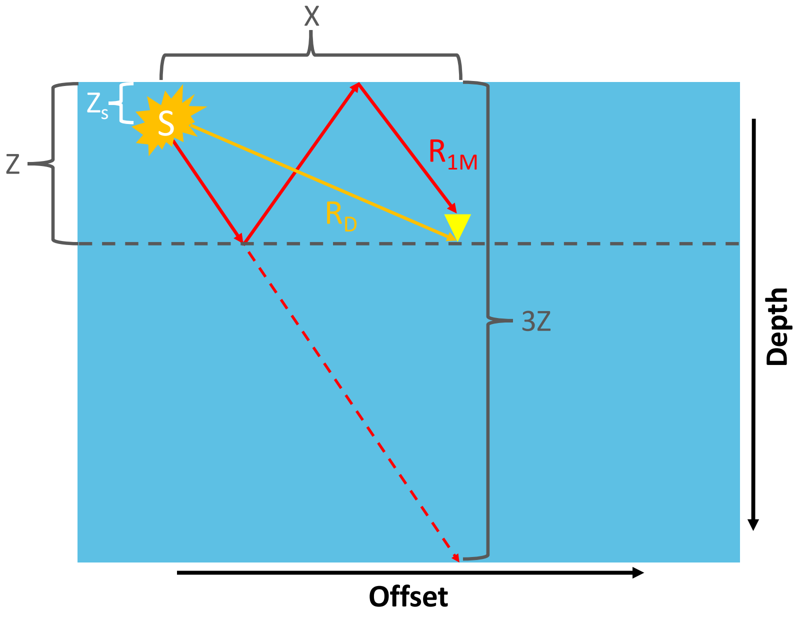

Figure B.2: Illustration of the events used in the near offset method. R_D is the travelled distance for the direct wave, while R_{1M} is the travelled distance for the 1st order multiple. z_s is the source depth, z is the water depth measured at the receiver and x is the horizontal source-receiver offset. The red dotted line illustrates how the R_{1M} in Equation B.4 is calculated with the use of a triangle with catethi's x and $3z - z_s$.

Results

The near offset method was performed for both PRM 4 and PRM 5, and the resulting velocity variations along receiver line 27 are shown in Figure B.3.

The red curve in Figure B.3 (a) and the light blue curve in (b) are the calculated velocities. They contain some spikes, which might be due to errors in the picking of the arrival times of the direct wave and the multiples. To better illustrate the trend in the velocity estimates, smoothing was performed with a moving average filter of 20 points. The smoothed velocity is shown as the dark blue line in Figure B.3 (a) and (b). The smoothed velocity varies between 1492 m/s and 1488 m/s for PRM 4 in (a) and between 1490 m/s and 1485 m/s for PRM 5 in (b). There is a general trend of decreased velocity with larger distance from the first receiver in both vintages. This makes sense as the water depth increases with increased distance from the first receiver. Hence, the proportion of cold, low-velocity water increases with distance from the first receiver, resulting in a lower average velocity.

To better illustrate the mean and the variation of the velocity estimates, frequency distribution plots were made of the velocity estimates, shown in Figure B.4 for PRM 4 (a) and PRM 5 (b). The mean velocity for PRM 4 was estimated to be 1490.19 m/s while the mean velocity for PRM 5 was estimated to be 1487.14 m/s. Hence, the two vintages differ with 3.05 m/s. The standard deviation of the velocity estimates in PRM 4 is 2.71 m/s, while it is pretty similar for PRM 5, 2.63 m/s.

The mean velocity for PRM 4, 1490.19 m/s, was used as a guide for the base velocity used in the TSCI method in this project.

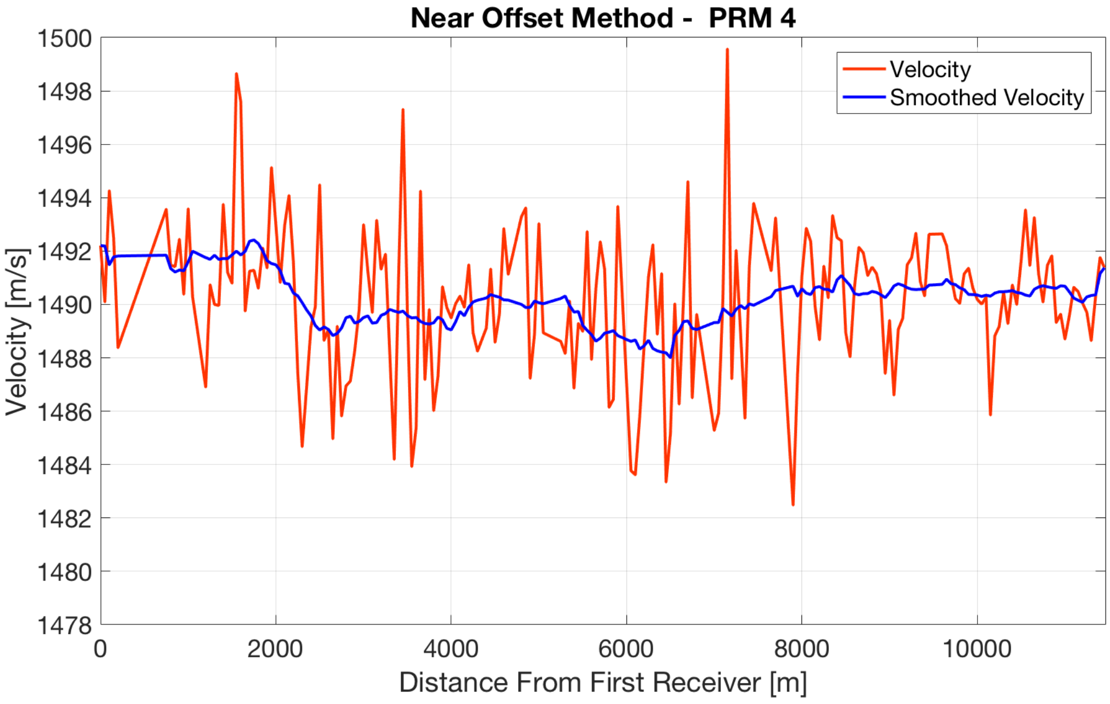

(a)

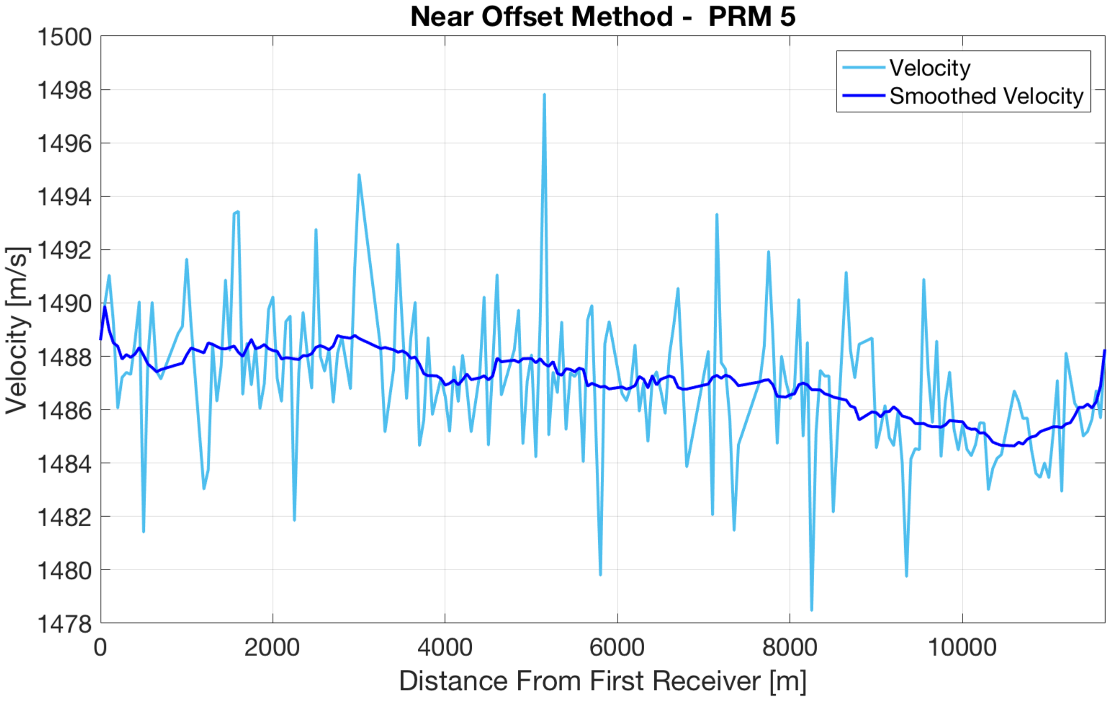

(b)

Figure B.3: Results from the near offset method. (a) shows the water velocities for PRM 4, while (b) shows the water velocities for PRM 5. Both figures show the estimated velocity variation with distance from the first receiver. The red curve in (a) and light blue curve in (b) are the raw estimated velocities, while the dark blue curve is a smoothed version, smoothed with a moving average filter of 20 points.

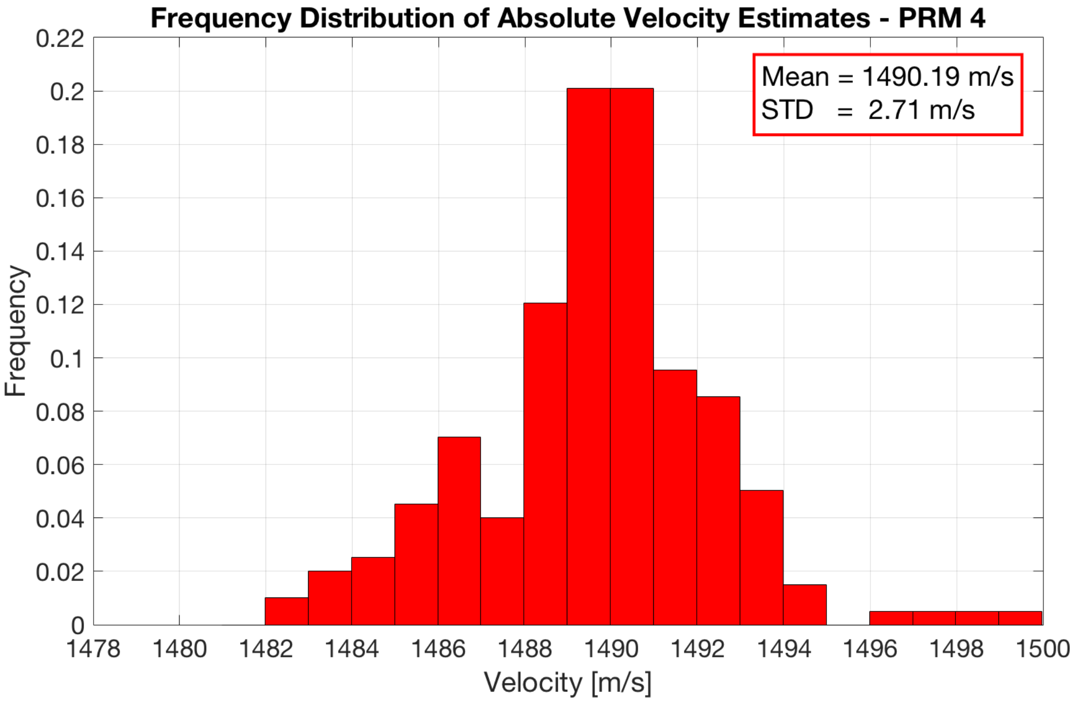

(a)

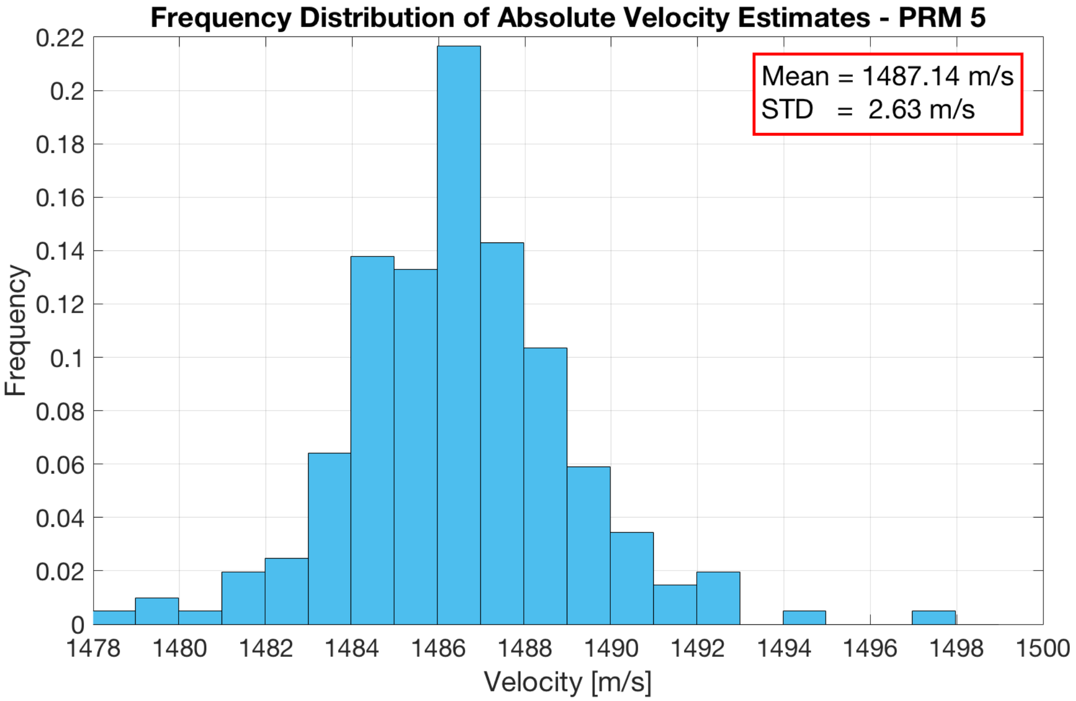

(b)

Figure B.4: Frequency distribution of the velocities estimated with the near offset method. (a) shows the estimates for PRM 4 while (b) shows the estimates for PRM 5. The mean and standard deviations are shown in the red box to the upper right in (a) and (b).

B.4 Outlier Removal and Smoothing

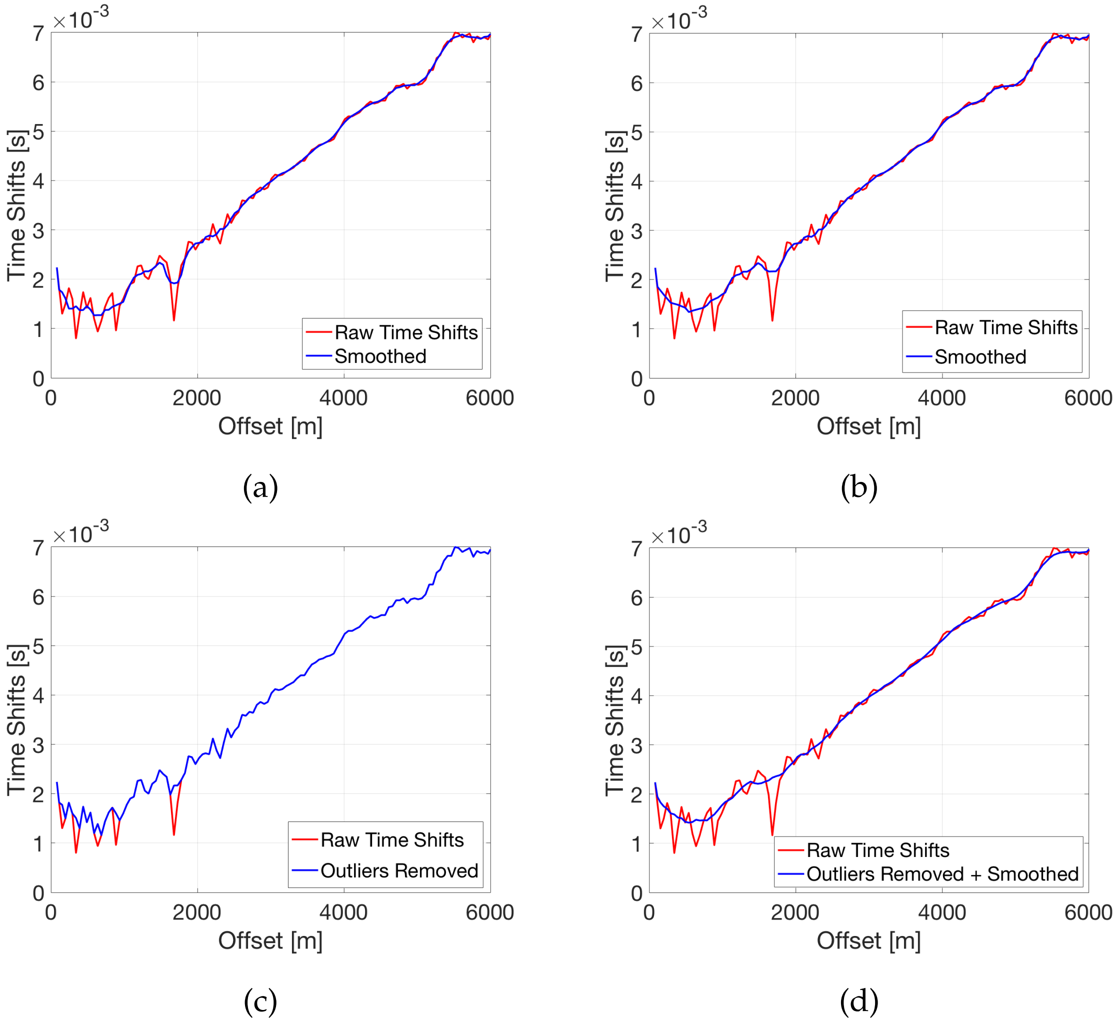

(a) (b) (c) (d)

Figure B.5: Illustration of the smoothing and outlier removal procedure. The red curve in (a)-(d) shows the raw time shifts. The blue curve represents: (a) the smoothed curve of the raw time shifts in, (b) smoothed curve of time shifts with removed outliers, (c) time shift curve were the outliers are replaced by the value of the smoothed curve in (b), (d) smoothed version of the blue time shift curve in (c).

The outlier removal and smoothing of the time shift curves are illustrated in Figure B.5. In (a) - (d) the red curve is the same and illustrates the raw time shifts. The raw time shift curve was first smoothed by a moving average filter of 10 points seen as the blue curve in (a). The largest outliers, i.e. the time shifts that differed the most from the smoothed time shift curve, were removed. The time shift curve with the removed outliers was smoothed, seen in (b), and the locations of the removed outliers in the raw time shift curve were filled in by the value of the new smoothed time shift curve in (b). The resulting time shift curve where the largest outliers are removed can be seen as the blue curve in (c). This curve was smoothed by a moving average filter of 10 points, seen as the blue curve in (d).

By comparing the blue curve in (d) with the blue curve in (a), it is clear that the impact of the outliers on the smoothed time shift curve has reduced significantly.

B.5 Shallow Subsurface Model at Snorre

In order to perform certain tests of the TSCI method, it was necessary to have a realistic model of the shallow subsurface at the Snorre field. This section describes how this shallow subsurface model was found with the use of VSP data and a method of following the first breaks on shot gathers.

B.5.1 Vertical Seismic Profiles Data

The VSP (Vertical Seismic Profiles) data was acquired from well 34/7-1, located 2831 meter south of receiver line 27. The location of the well is shown by the yellow dot in Figure B.6. The VSP data for this well was acquired with a fixed source at an offset from the well. The receiver was placed in the well, starting at the bottom of the well and gradually moved upwards. The VSP in well 34/7-1 was acquired all the way up to 47 meters below the sea bottom. This VSP data was used to give an indication of the velocities in the shallow subsurface at the Snorre field.

From the traveltimes in the VSP survey, interval velocities were calculated. These interval velocities are shown in Figure B.7. For depths larger than the sea bottom at 320 meters, the velocity increases gradually up to 2450 m/s around 1000 meters below the sea surface.

Since the source in the VSP survey was located at an offset from the well, cosine corrections were made in order to re-calculate the traveltimes into vertical traveltimes. The cosine correction assumes totally straight ray paths. This is a good assumption for deep areas, but for the shallow parts, this correction can create some errors. This is because the ray paths in reality not are straight, but will bend as the wave goes from the slow water medium to the faster sediments and rocks below the sea floor. Thus, the simple cosine correction, which assumes straight ray paths, becomes less valid and some errors in the calculated velocities might occur for the shallow parts. The VSP interval velocities in Figure B.7 should because of this not be trusted blindly. However, they give an indication of the velocity trend in the shallow subsurface at Snorre.

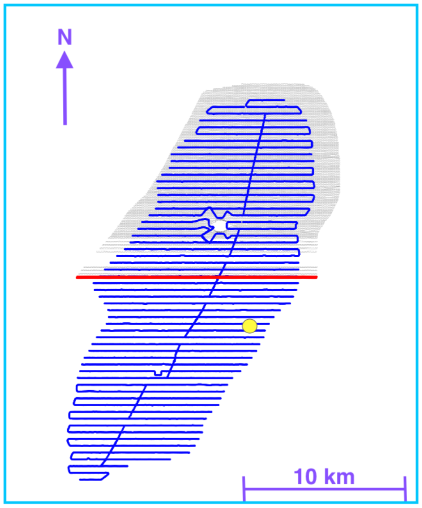

Figure B.6: The figure shows the distribution of the permanent receivers at Snorre. Receiver line 27 is located below the red line, which illustrates the shot line used in this project. The yellow dot highlights the approximate location of well 34/7-1 where the VSP data was acquired, 2831 meters south of receiver line 27.

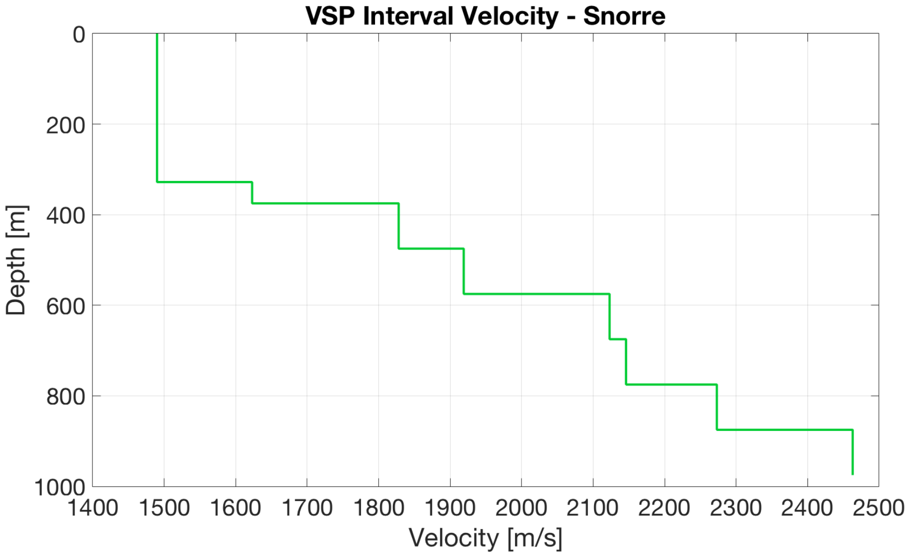

Figure B.7: Interval velocities calculated from VSP data for the first 970 meters below the sea surface. The y-axis is given in depth below the sea surface.

B.5.2 Picking First Breaks

Due to the uncertainties tied to the shallow VSP velocities, another method was included to establish the model parameters of the shallow subsurface at Snorre. This method was based on picking the first breaks for offsets between 0 to 3000 meters. The direct wave was tracked from zero offset until the arrival of the first refracted wave. Then the first arriving refracted wave was tracked until 3000 meters. The tracking of the first breaks is shown as the red curve in the receiver gather in Figure B.8. The reason for tracking the first breaks is that the first arriving refracted waves have travelled horizontally in the shallow part of the subsurface. Therefore, the traveltimes and gradients of these refracted events contain lots of information about the shallow subsurface velocities.

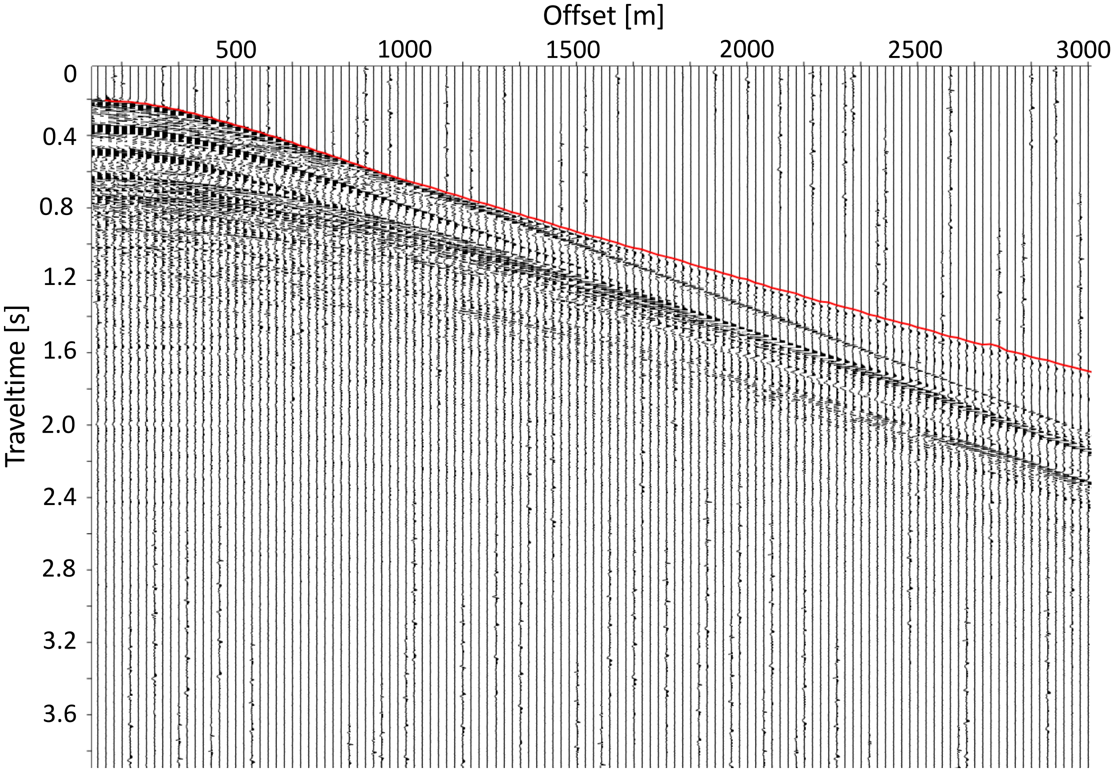

Figure B.8: The first breaks (red curve) were picked on a shot gather from Snorre PRM 5. The direct wave was tracked from zero offset until the first refracted wave broke out. Then the tracking jumped over to the first arriving refracted wave. Note how the red curve separates from the direct wave as the first refraction arrives for offsets around 1000 meters.

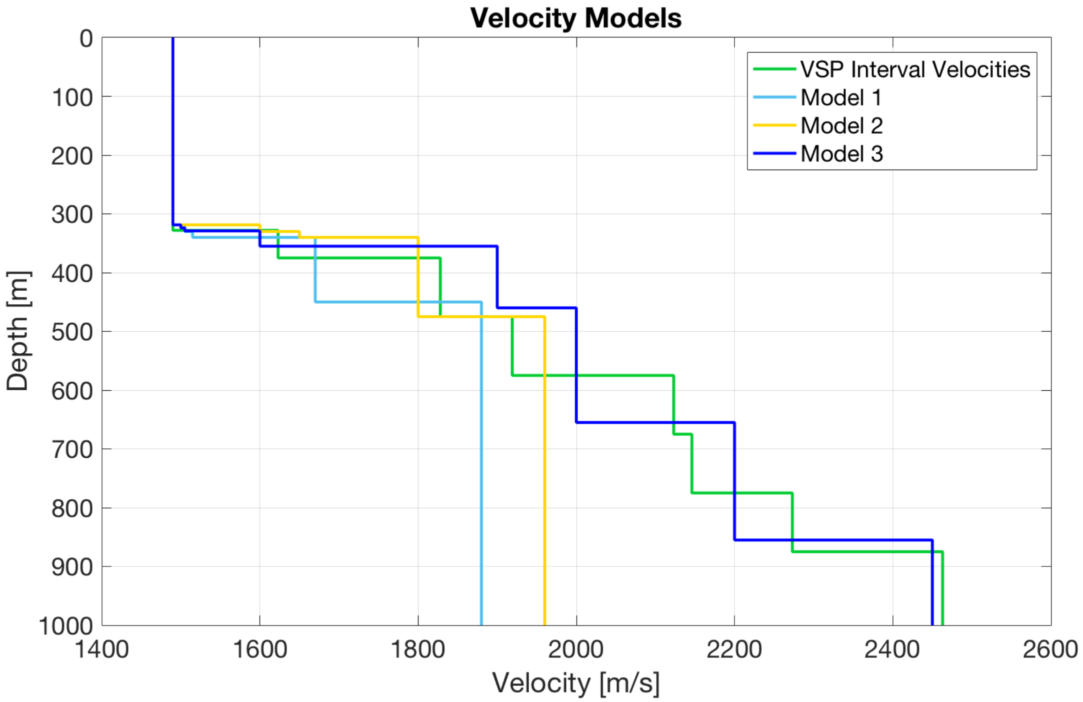

Figure B.9: Different velocity models tested with the first-break method. The green curve is the interval velocity extracted from the VSP data, while light blue, yellow and dark blue curve represents different velocity models for the shallow subsurface.

Based on the interval velocities extracted from the VSP data, different velocity models were made for the shallow subsurface down to 1000 meters below the sea surface. Figure B.9 shows 3 such velocity models, along with the interval velocities from the VSP data.

For each of the velocity models, the SKB modelling software described in Section 2.8, was run to make synthetic seismograms. The first breaks of these synthetic seismograms were picked for the first 3000 meters, and compared with the first breaks of the measured data, as shown in Figure B.10. The first breaks from the measured data are shown as red circles, while the dark blue, yellow and light blue curves are the first breaks based on the velocity models with the corresponding colours in Figure B.9. As seen in Figure B.10, the dark blue curve matches the red circles almost perfectly. Therefore, the corresponding velocity model of the dark blue curve in Figure B.9 was assumed to be quite close to the real subsurface at Snorre. As seen in Figure B.9, the dark blue curve is pretty close to the green VSP curve, which increased the confidence that the dark blue velocity model is close to the true velocity model of the shallow subsurface at Snorre.

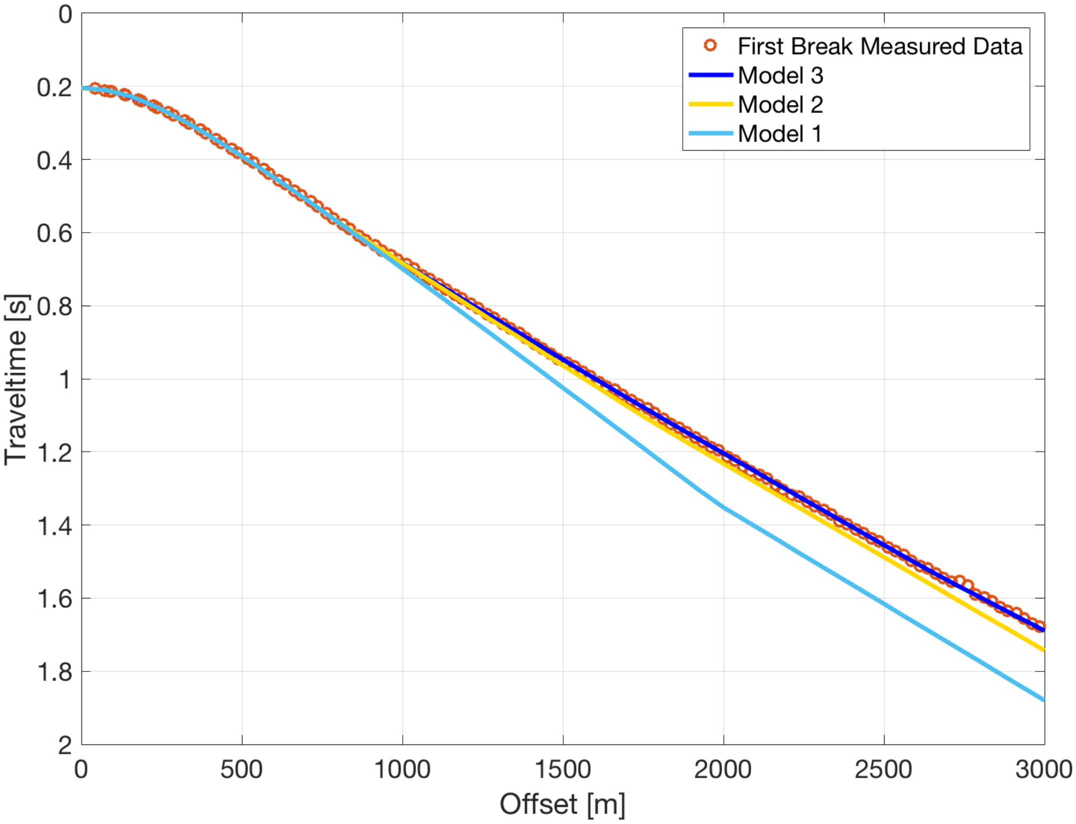

Figure B.10: The velocity models in Figure B.9 were inserted into the SKB modelling software and the modelled first breaks were compared to the measured first breaks. The red circles represent the first breaks picked from the Snorre data. The yellow, light blue and dark blue curves correspond to modelled first breaks based on the velocity models with the corresponding colors in Figure B.9. Note the dark blue curve, follows the red circles almost perfectly. The velocity model for the dark blue curve was assumed to be the most correct one for Snorre.

B.6 Test of Robustness to Complex Subsurface

The subsurface is in general not a simple layered model. It can be complex and changes occur both laterally and vertically. To investigate how well the TSCI method worked for a subsurface that was complex and varying, two tests were performed.

B.6.1 Robustness to Variations in Subsurface Velocities

The first test aimed to investigate the TSCI method's robustness to changes in the subsurface velocities. Two different models were made with different subsurface velocities. Both models were equal to the model shown in Figure 4.21, with the same model parameters as in Table 4.1, except of the P-wave velocities. Figure B.11 shows the P-wave velocity profile for the two models together with the assumed velocity profile at Snorre (obtained in Appendix B.5). The red curve represents a velocity model with 20 % higher velocities than the assumed Snorre model, while the yellow curve represents a velocity model with 20 % lower velocities than the assumed Snorre model.

For each velocity model, the SKB modelling described in Section 2.8, was used to make a synthetic shot gather pair, consisting of 2 shot gathers only differing by a known water velocity of 3 m/s. The TSCI method, described in Section 4.1, was used to estimate the known velocity change for the shot gather pairs. The offset intervals included in the inversion was equal for all water column events: 0 to 6000 meters. The objective function used was the same as in Equation 4.11, where $M1_{n,x}$ was the time shifts from the synthetic shot gather pairs. To investigate how the accuracy of the estimates varied with the number of multiples included in the calculations, 6 separate inversions were performed with increasing number of included multiples. N in Equation 4.11 increased from 1 (inclusion of only the direct wave) to 6 (inclusion of all the multiples up to 5th order).

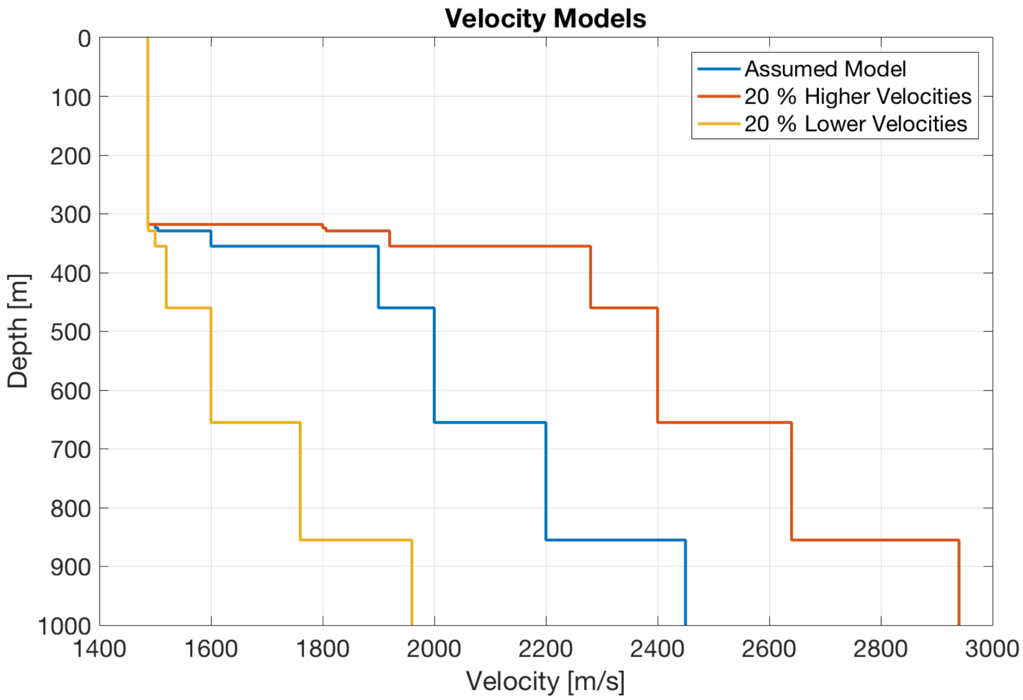

Figure B.11: Velocity models used to test the TSCI method's robustness to subsurface velocity variations. The blue profile represents the assumed velocity model for Snorre (same as in Figure 4.19). The red profile has 20 % higher velocities than the assumed Snorre model, while the yellow profile has 20 % lower velocities than the assumed Snorre model. No velocities for the low-velocity model were lower than the water velocity, so the uppermost subsurface layers did not have 20 % lower velocities than the assumed Snorre model.

Results

The estimated velocity changes for the 3 different velocity models in Figure B.11 are shown in Figure B.12. The estimates for the high-velocity model are very precise for the inclusion of all multiples, even more precise than the estimates for the assumed velocity model at Snorre. The estimates for the low-velocity model are good up to the inclusion of the 3rd multiple. As the 4th and 5th multiple were included, the error increased significantly.

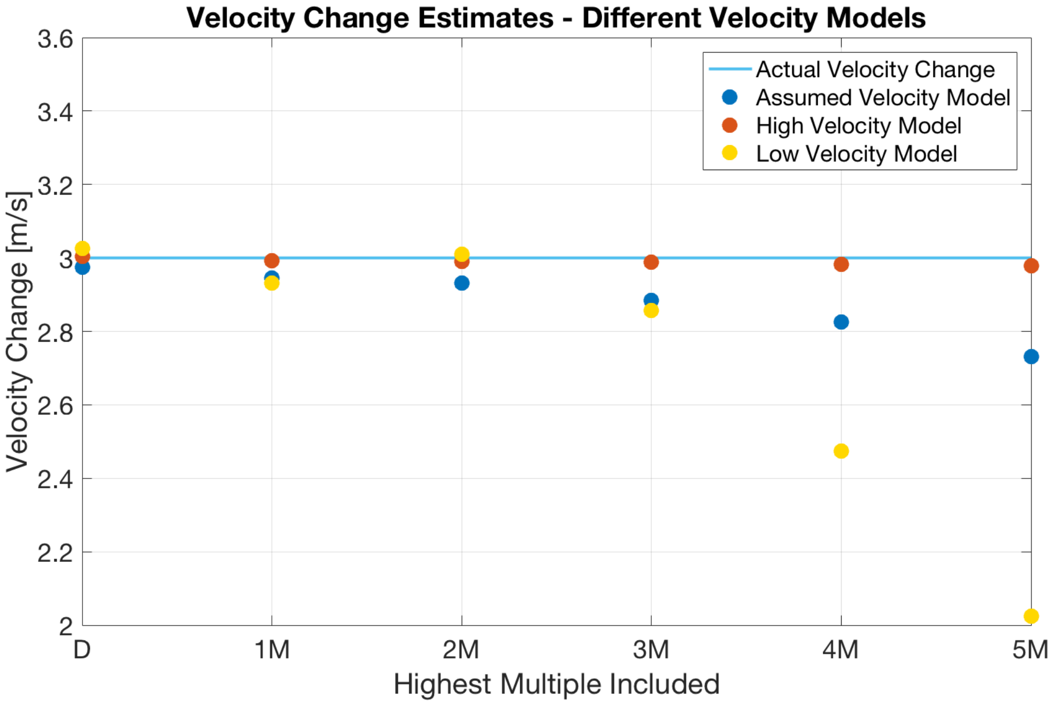

Figure B.12: Velocity change estimates for 3 synthetic shot gather pairs based on the 3 velocity models shown in Figure B.11. The x-axis indicates the highest order multiple included in the calculations. The blue dots correspond to the estimates for the assumed Snorre model and is the same as the estimates shown in Figure 5.1. The red and yellow dots represent the models with 20% higher and lower velocities than the assumed Snorre model respectively. Note the precise velocity change estimates for all multiple orders for the high-velocity model.

Figure B.13 shows the time shift curves for the direct wave, 2nd and 4th multiple. The high-velocity model represents the time shift curves to the left, which all are relatively smooth and easy to follow. This is not the case for the time shift curves for the low-velocity model, which are shown to the right. These curves are of lower quality and it is only possible to infer the main trend in the time shift curves for the direct wave and 2nd multiple. The 4th multiple contains way too much spikes. These time shift curves explain the results in Figure B.12 as the low-quality time shifts for the low-velocity model resulted in inaccurate velocity change estimates for the inclusion of the high order multiples. The high-quality time shift curves for the high-velocity model resulted in precise velocity change estimates for the inclusion of all multiples.

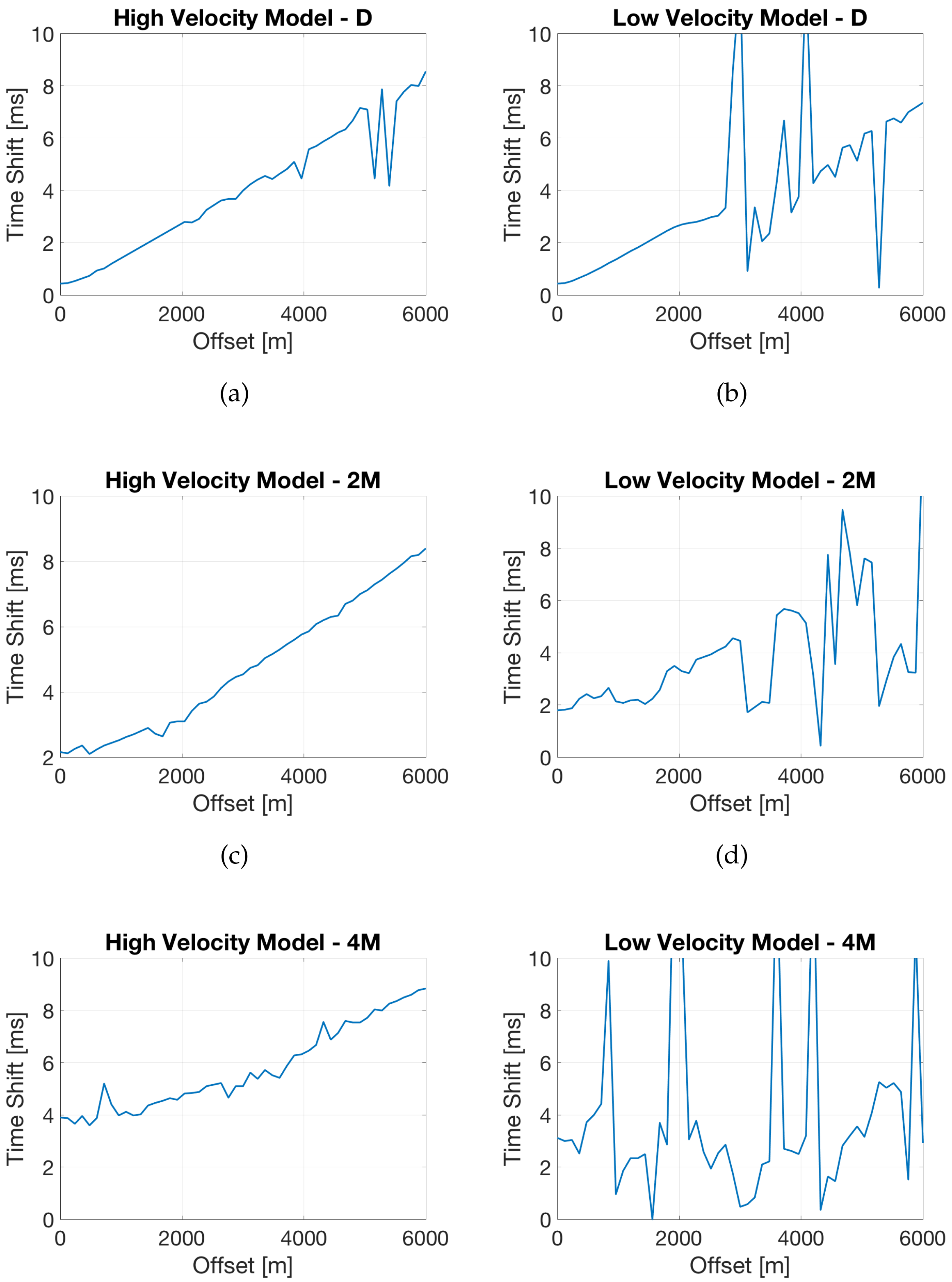

(a) (b) (c) (d) (e) (f)

Figure B.13: (a), (c) and (e) represents time shift curves for the model with 20% higher subsurface velocities than the assumed model at Snorre. (b), (d) and (f) represents time shift curves for the model with 20% lower subsurface velocities than the assumed model at Snorre. (a) and (b) shows time shift curves for the direct wave, (c) and (d) for the 2nd multiple and (e) and (f) for the 4th multiple. Note the difference in smoothness and quality of the time shift curves for the two models.

To understand the reason for the variation in quality of the time shift curves in Figure B.13, the sea bottom reflection coefficient variation with offset of the direct wave in the different velocity models are shown in Figure B.14. The direct wave in the high-velocity model reaches critical offset fast as the reflection coefficient becomes 1 for offsets below 500 meters. The direct wave in the assumed Snorre velocity model follows quite quickly around 1800 meters, while the direct wave in the low-velocity model does not reach critical offset before 9000 meter offset. As the offsets included in the tests only were the first 6000 meters, no one of the water layer events reached critical angle for the low-velocity model. As explained in Section 4.1.8, high reflection coefficients result in large amplitudes of the water column events compared to the surrounding signal and high-quality time shift curves. Low reflection coefficients result in low amplitudes of the water column events and poor quality time shift curves for the high order multiples. This explains the high-quality time shift curves for the high-velocity model and the low-quality time shift curves for the high order multiples in the low-velocity model.

Both the high and the low-velocity model was quite unrealistic, and extreme scenarios. Even though the low-velocity subsurface model resulted in poor estimates as the high order multiples were included, the water velocity change was estimated pretty accurately up to the inclusion of the 2nd multiple. Thus, the TSCI method is expected to work well in areas with various subsurface velocities, as long as the number of multiples and their corresponding offset intervals are adjusted and optimized for each individual subsurface model.

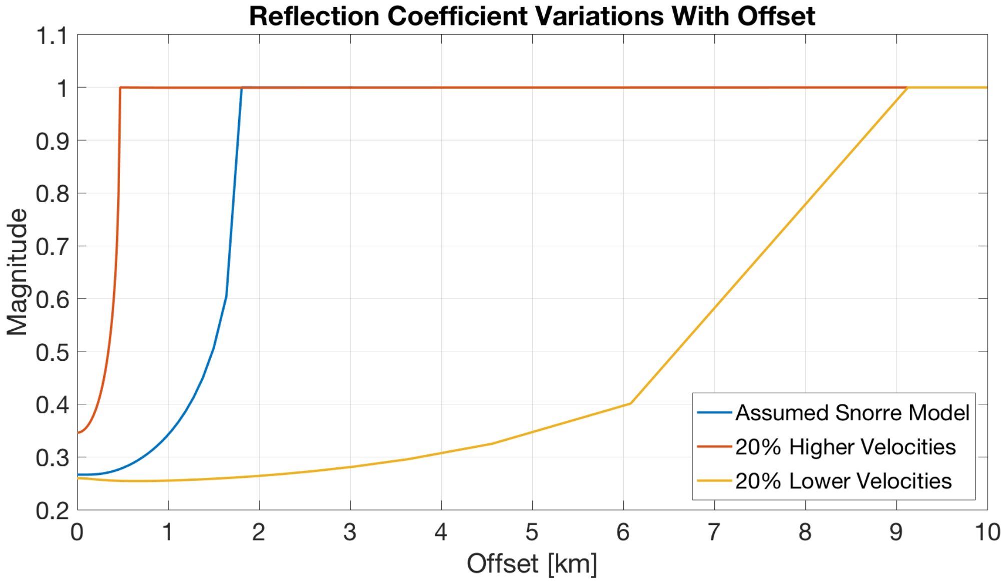

Figure B.14: Reflection coefficient variation with offset for the direct wave in the 3 models shown in Figure B.11, calculated with the Zoeppritz equations. Note the fast increase in reflection coefficient for the red and the blue model compared to the yellow model.

B.6.2 Robustness to Variations in Subsurface Layer Thickness

The second test aimed to investigate the TSCI method's robustness to changes in the subsurface layer thicknesses. As subsurface layers thicken and thin laterally, reflections and refractions occur at different points in the subsurface and create differences in the wave field. The TSCI method's robustness to such variations was investigated.

2 different subsurface models were made, shown in Figure B.15. The two models consisted of 3 layers each: a water layer, a low-velocity layer with a p-wave velocity of 1600 m/s just below the water layer, and a high-velocity layer with a p-wave velocity of 2000 m/s at the bottom. The only difference between the two models was the thickness of the low-velocity layer just below the sea bottom. The model in Figure B.15 (a) had a 10 meter thick low velocity layer, while the model in Figure B.15 (b) had a 50 meter thick low velocity layer. For each model in Figure B.15, the SKB modelling software was used to make a synthetic shot gather pair, consisting of 2 shot gathers only differing by a known water velocity of 3 m/s. The TSCI method, described in Section 4.1, was used to estimate the known velocity change for both shot gather pairs. The objective function and the way the TSCI method was applied, was the same as described for the test in Appendix B.6.1.

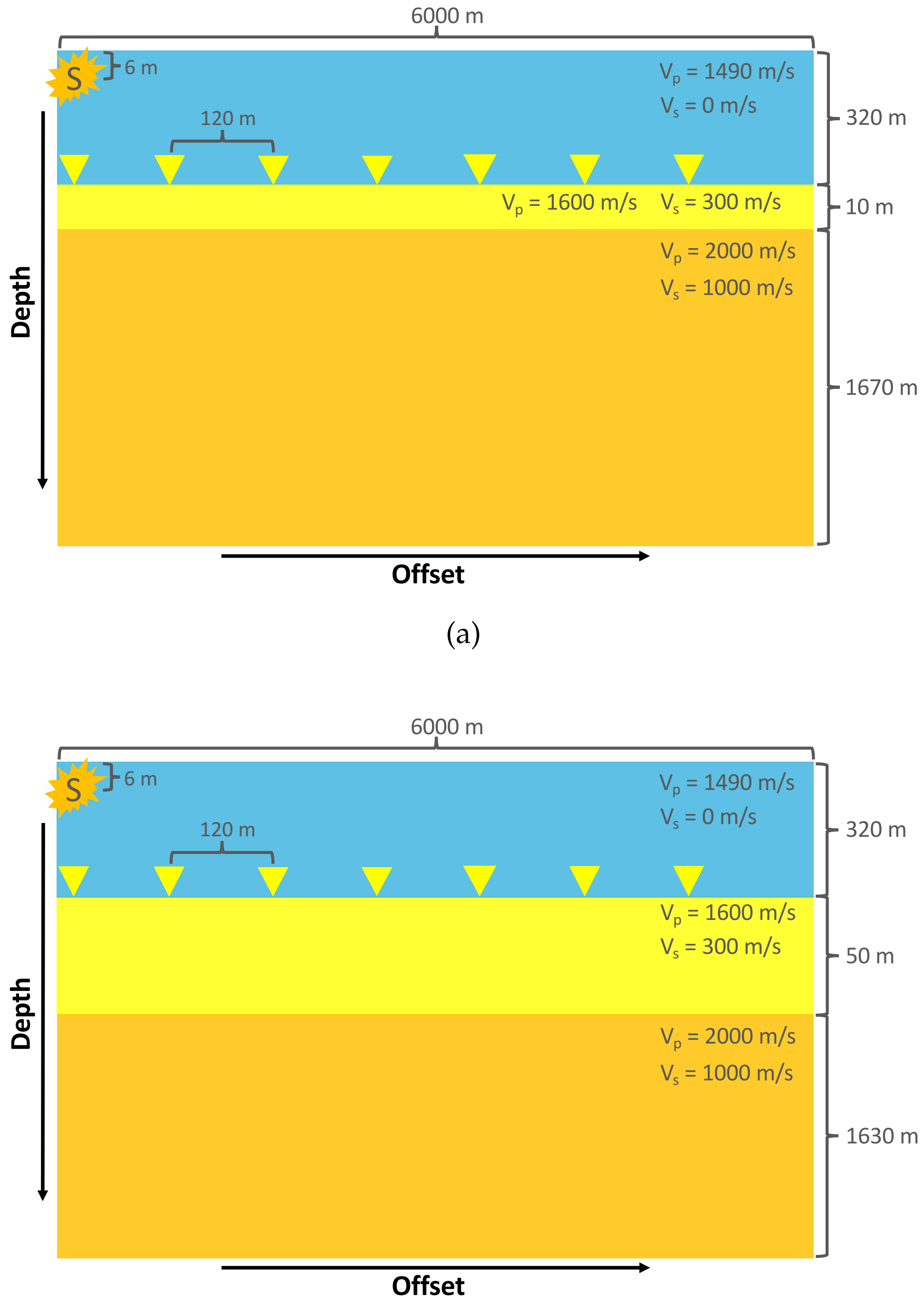

(a)

(b)

Figure B.15: Figure shows the models used for test the robustness to subsurface layer thickness variations. The models consisted of 3 layers: a water layer, a low-velocity layer just below the water layer, and a high-velocity layer at the bottom. The only difference between the two models was the thickness of the low-velocity layer just below the sea bottom: (a) had a 10 meter thick low-velocity layer, (b) had a 50 meter thick low-velocity layer. The P and S-wave velocities are shown in the figure. The densities was equal for both models: 1 g/cm^3 for the water layer, 1.5 g/cm^3 for the 1st layer below the water layer and 2 g/cm^3 for the 2nd layer below the water layer. 51 receivers were included with a receiver spacing of 120 meters, corresponding to offsets up to 6000 meters. The source was located to the far left in the model, above the first receiver, with a source depth of 6 meters. The thickness of the model layers are listed in the figure.

Results

The results are shown in Figure B.16 and show the velocity change estimates for the two different models in Figure B.15. The velocity changes are precisely estimated for both models. There is a small difference between the two models, as the velocity change estimates for the model with the thick low-velocity layer is slightly lower than for the model with thin low velocity layer. However, the difference is negligible up to the inclusion of the 4th multiple. As the 5th multiple is included, the error for the model with thick low-velocity layer increases. However, the maximum error of 0.16 m/s, is not a large error.

Figure B.17 shows the time shift curves for the direct wave, 2nd and 4th multiple for the two models. The time shift curves for the model with thin low-velocity layer are much smoother and of higher quality than the time shift curves for the model with thick low-velocity layer. This is especially prominent by comparing the time shift curves for the 4th multiple in (e) and (f).

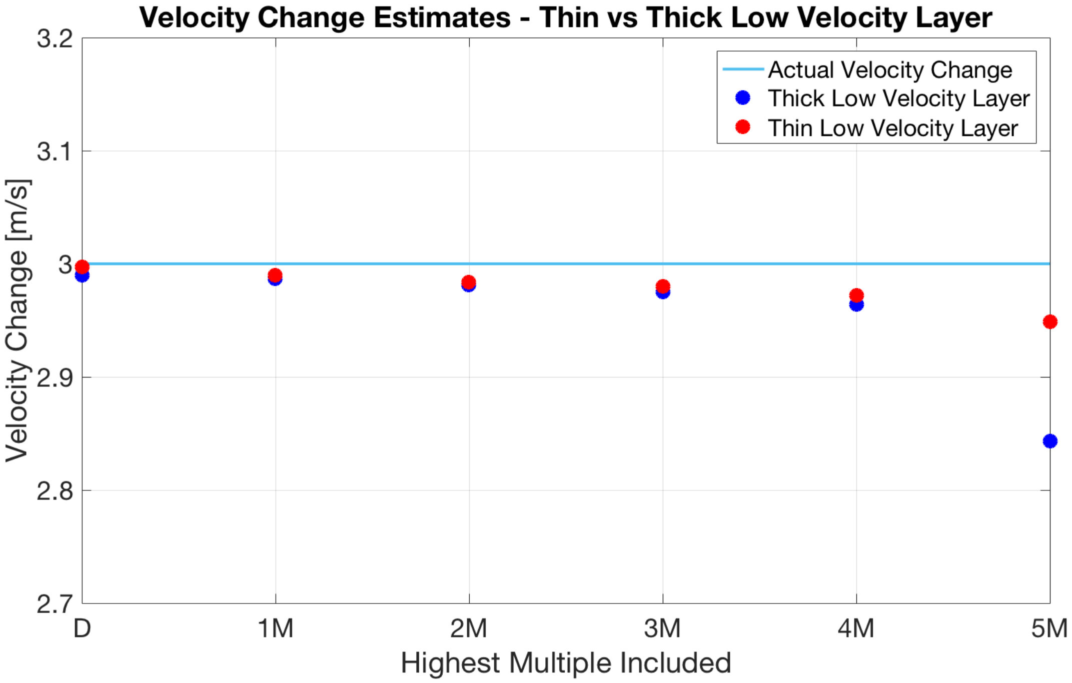

Figure B.16: Velocity change estimates for the 2 synthetic shot gather pairs based on the 2 models shown in Figure B.15. The light blue line represents the actual velocity change of 3 m/s. The red dots correspond to the estimated velocity changes for the model with thin low-velocity layer (10 meters). The blue dots correspond to the estimated velocity changes for the model with thick low-velocity layer (50 meters).

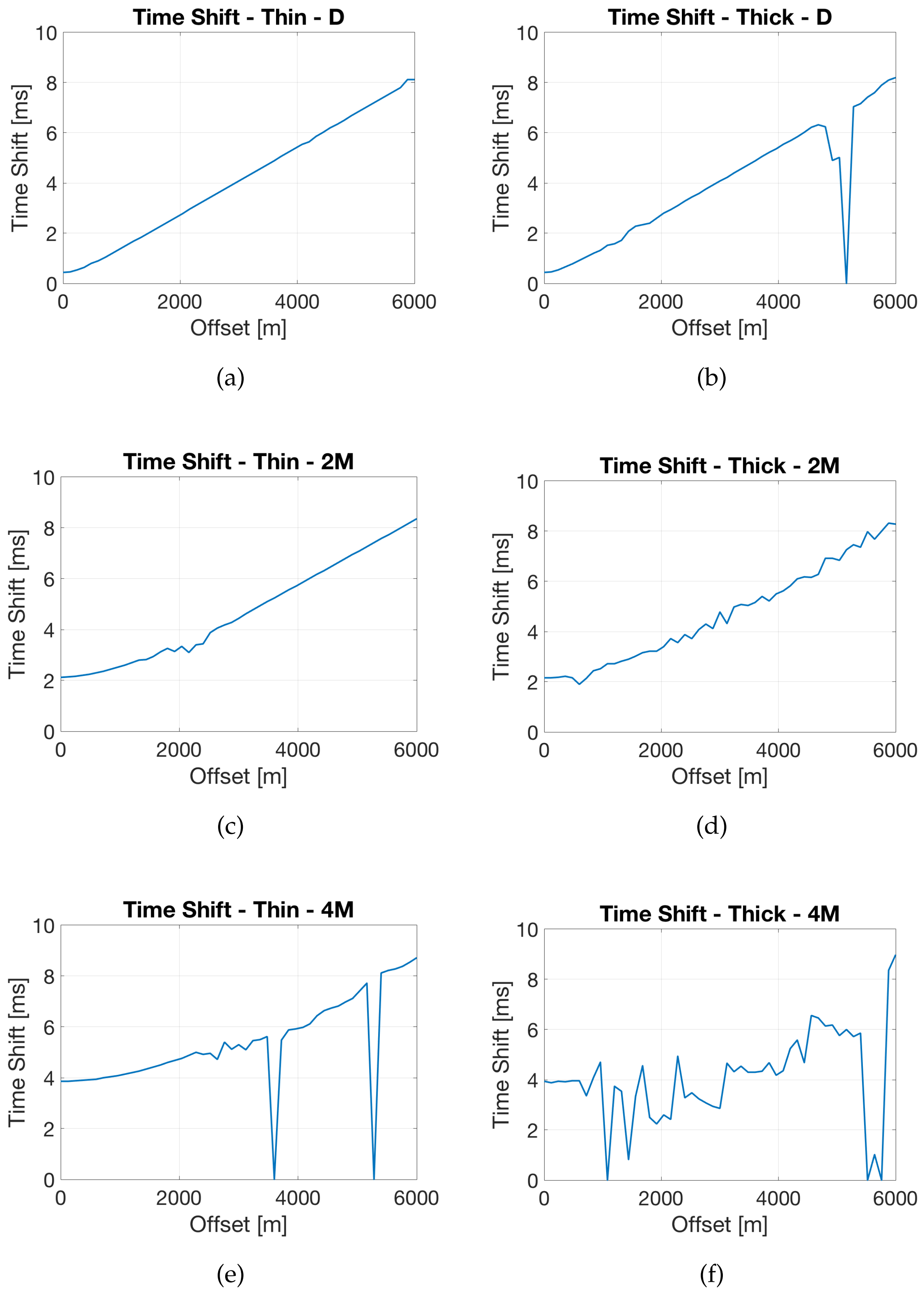
Time Shift - Thin - D

Time Shift - Thick - D

Time Shift - Thin - 2M

Time Shift - Thick - 2M

Time Shift - Thin - 4M

Time Shift - Thick - 4M

(a) (b)

(c) (d)

(e) (f)

Figure B.17: Time shift curves for the 2 synthetic shot gather pairs based on the 2 models shown in Figure B.15, for the direct wave in (a) and (b), the 2nd multiple in (c) and (d), and the 4th multiple in (e) and (f). (a), (c) and (e) correspond to the model with thin low-velocity layer. (b), (d) and (f) correspond to the model with thick low-velocity layer. Note the difference in smoothness and quality for the time shift curves to the left and right.

Since the thickness of the low-velocity layer in the thin layer model is only 10 meters, the direct wave and the reflection from the first boundary below the sea bottom arrives almost simultaneously. The two events do not separate, and the direct wave pulse just gets a little extended as shown in Figure B.18 (a). In the model with thick low-velocity layer, the reflection from the first boundary below the sea bottom is clearly separating from the seabed reflection, as seen in Figure B.18 (b). Hence, the number of separate events which can interfere with the water layer events becomes much higher in the model with thick low-velocity layer than for the model with thin low-velocity layer. These interfering events create "zones" where the wave field becomes complex and it is difficult to separate the water column events from the interfering events. This may have affected the quality of the time shift curves, resulting in less precise estimates of the velocity change for the model with thick low-velocity layer. However, the error in the estimates in Figure B.18 was relatively small, indicating that the TSCI method is relatively robust to the changes that occur in the wave field as the subsurface layer thickness varies.

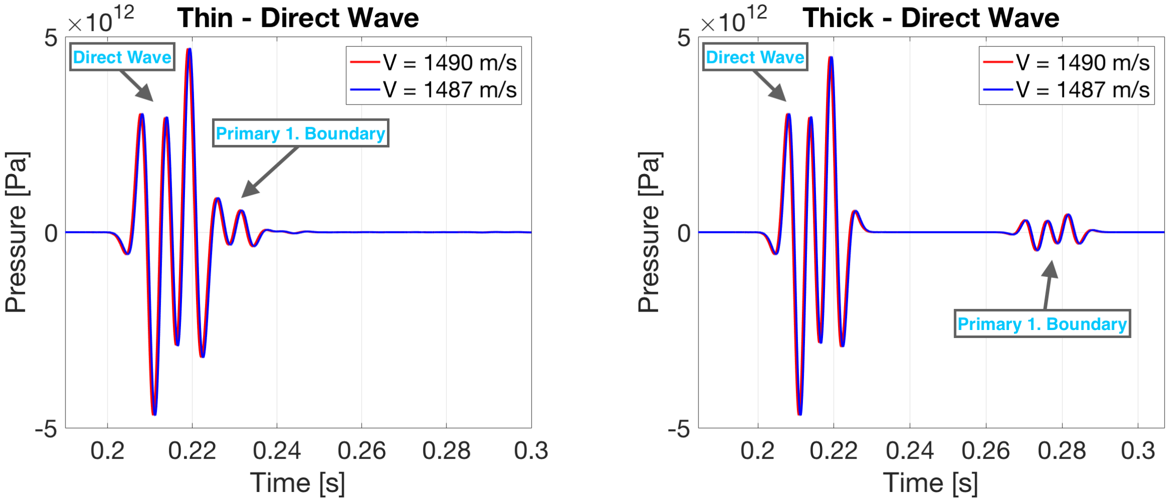

(a) (b)

Figure B.18: Traces show the zero offset direct wave and the reflection from the first boundary below the sea bottom for the model with thin low-velocity layer (a) and the model with the thick low-velocity layer (b). Note that the two events merge to become 1 event in (a), while there is larger separation between the events in (b).

B.7 Relative Tidal Level Induced Time Shifts Between Two Models With Different Water Depth

Equation 2.8 shows the expression for the time shifts caused by pure tidal changes ($\Delta v = 0$), and is given again here:

$$\Delta t_{n,x} \approx \frac{(2n-1)^2 T_0^2}{t_{n,x}} \frac{\Delta z}{z}$$

See Equation 2.8 for explanations and symbols. Consider two models with different water depths of $z1$ and $z2$. The relative tidal change induced time shifts between the two models becomes

$$\frac{\Delta t_{2,n,x}}{\Delta t_{1,n,x}} \approx \frac{\frac{(2n-1)^2 T_{0_2}^2}{t_{2,n,x}} \frac{\Delta z}{z_2}}{\frac{(2n-1)^2 T_{0_1}^2}{t_{1,n,x}} \frac{\Delta z}{z_1}} \tag{B.9}$$

$T_{0_1} = \frac{z_1}{v}$ and $T_{0_2} = \frac{z_2}{v}$ (sea bottom receivers), so Equation B.9 can expressed as

$$\frac{\Delta t_{2,n,x}}{\Delta t_{1,n,x}} \approx \frac{\frac{z_2^2}{v^2 t_{2,n,x}} \frac{\Delta z}{z_2}}{\frac{z_1^2}{v^2 t_{1,n,x}} \frac{\Delta z}{z_1}} \tag{B.10}$$

Since the velocity is the same in both models, the v's will be cancelled. Hence, the relative tidal change induced time shift between two models with different water depth can be expressed as

$$\frac{\Delta t_{2,n,x}}{\Delta t_{1,n,x}} \approx \frac{z_2 t_{1,n,x}}{z_1 t_{2,n,x}} \tag{B.11}$$

The relative time shift expression in Equation B.11 is plotted against offset in Figure B.19, with z_1 equal 320 meters, z_2 equal 350 meters. It is clear that the time shifts produced by the model with larger water depth, z_2, is larger than the time shift produced by the model with lower water depth, z_1. This is because the tidal change is a vertical change. Since the larger water depth z_2 induces a more vertical propagation direction than the lower water depth z_1 for a given offset, the model with larger water depth will be affected more by the vertical tidal change than the model with shallower water depth. The relative time shift for zero offset in Figure B.19 is 1. This is because the propagation direction in both models is vertical for zero offset, and the two models will be time shifted equally.

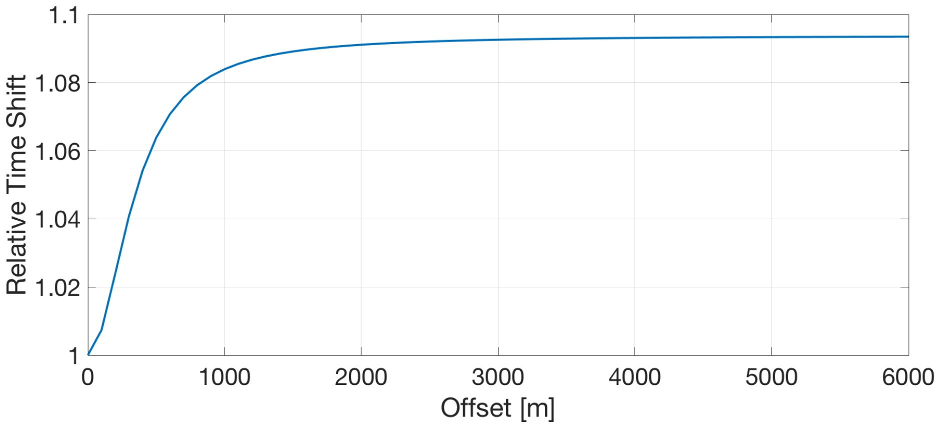

Figure B.19: Figure illustrates Equation B.11 for the direct wave ($n = 1$), and shows the relative time shift between two models with different water layer thickness. z_1 is 320 meters and z_2 is 350 meters. The velocity used in the calculation of the traveltimes was $v = 1490$ m/s.

Equation B.11 is plotted for a fixed offset for the direct wave and the 9 first multiples in Figure B.20. Note how the relative time shift and the differences between the two models reduce with multiple order. This is because higher multiple orders induce more vertical propagation for both the model with large water depth and the model with shallow water depth. This reduces the difference between the time shifts of the two models.

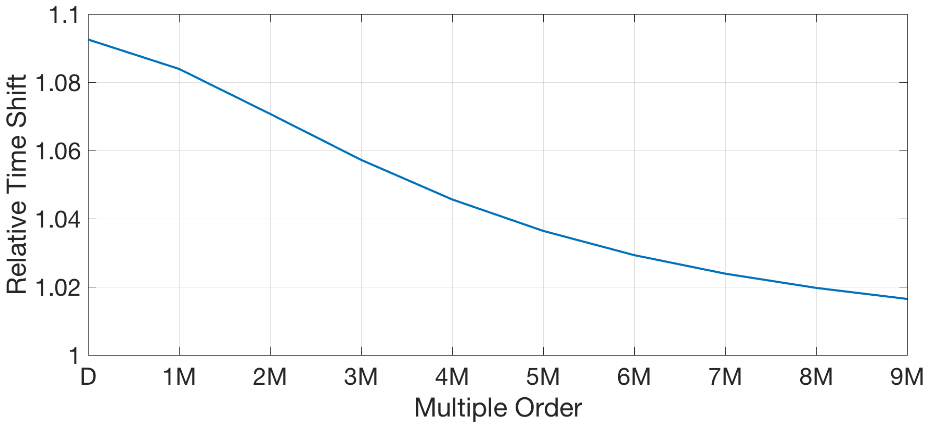

Figure B.20: Figure illustrates the relative time shift between two models with different water layer thickness in Equation B.11. z_1 is 320 meters and z_2 is 350 meters. The offset is fixed to 3000 meters, while the multiple order varies. The velocity used in the calculation of the traveltimes was $v = 1490$ m/s.

B.8 Bending of Rays at Large Offsets

Figure B.21 shows the TS Dip velocities from PRM 4 (red) together with an approximate velocity profile of the TS Dip velocities (blue). Figure B.22 shows a raytracing performed for the direct wave through the blue velocity profile in Figure B.21. At offsets up to 3000 meters, the rays are relatively straight. However, the rays measured at large offsets have a visible change of angle around 60 meters depth.

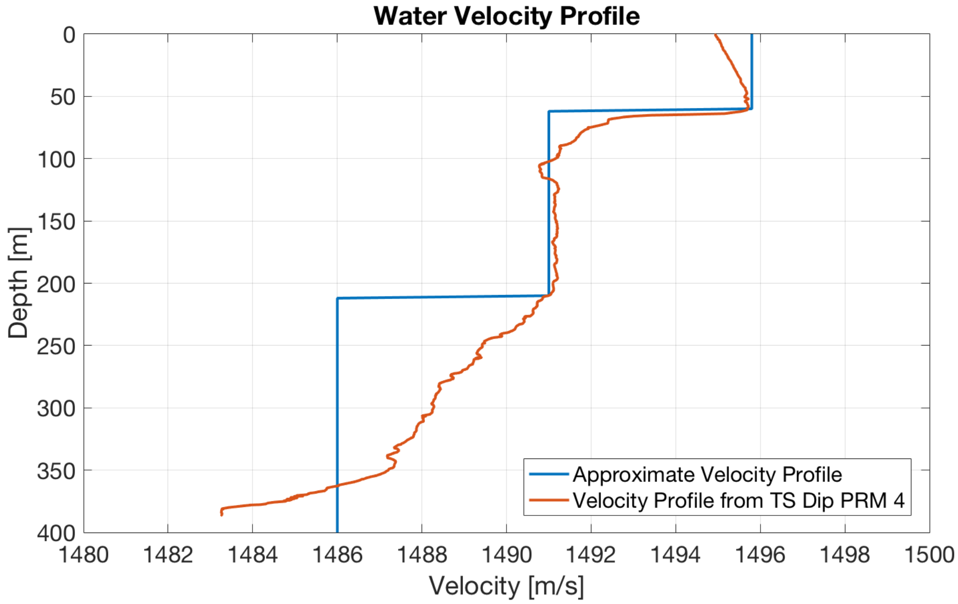

Figure B.21: Water velocity profiles. The red curve shows the TS Dip water velocity profile for PRM 4 (the same as shown in Figure 3.10), while the blue curve shows an approximation to the red water velocity profile.

Figure B.23 shows the difference in travelled distance between the bent rays in Figure B.22 and the corresponding straight rays with the same start and stop points. The travel distance difference increases with offset, but not by much. At 6000 meters, the bent ray has only travelled 4.8 meters longer than the straight ray. However, since a greater proportion of the bent rays' travel path is in the uppermost high-velocity parts of the water layer, the traveltime of the bent rays are actually lower than the traveltime of the corresponding straight rays at large offsets. This can be seen in Figure B.24, which shows the effective traveltime difference between the straight rays and the bent rays. So even though the bent rays travel a longer distance, their traveltime is lowered compared to straight rays. The maximum traveltime difference is ≈ 3.3 ms for 6000 meter offset.

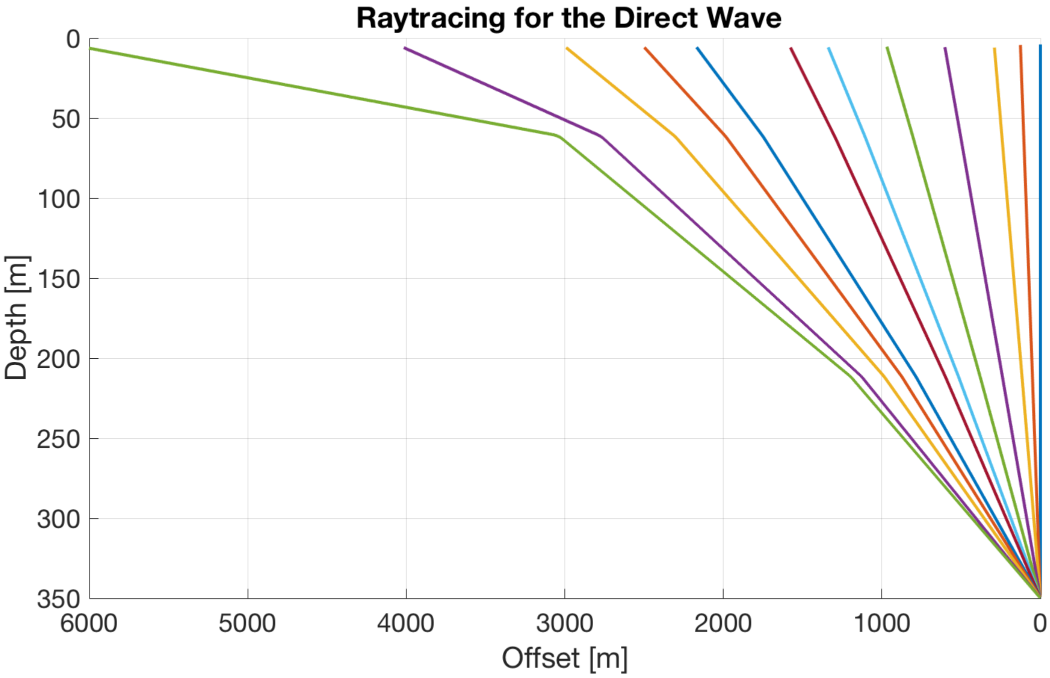

Figure B.22: Raytracing for the direct wave through the blue water velocity profile in Figure B.21. The water depth is 350 meters. Note the increased bending of the rays for increased offset. The y-axis is largely exaggerated compared to the x-axis to enhance the visibility of the ray bending.

As seen in Figure B.22, the ray bending increases as the proportion of horizontal propagation direction increases. Hence, the effect of ray bending is largest for the direct wave. As the multiple order increases, the angle of incidence becomes closer vertical, and the ray bending effect reduces. For the maximum offset included for the direct wave in this project, 4000 meters, the bent ray has a reduced traveltime with ≈ 0.8 ms compared to a straight ray. This is not a large value, but the ray bending will affect the shape of the time shift curves slightly at the large offsets in this project.

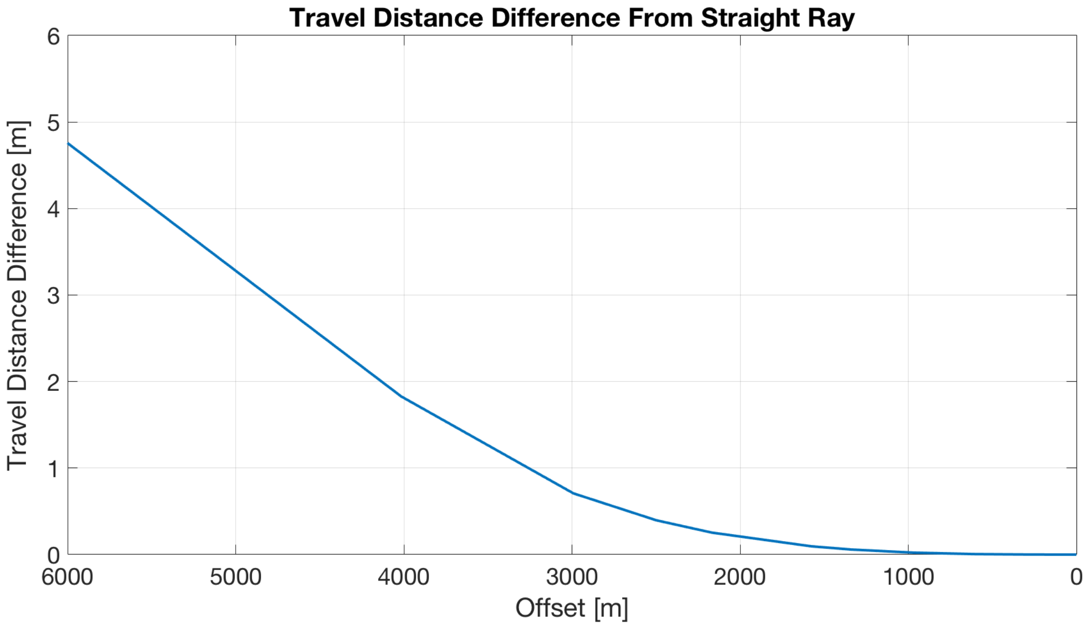

Figure B.23: Differences in travelled distance between the bent rays in Figure B.22 and the corresponding straight rays with the same start and stop points. The differences are calculated by: (Travelled Distance Bent Rays) - (Travelled Distance Straight Rays). Note the increase in difference with offset as the rays get more and more bent.

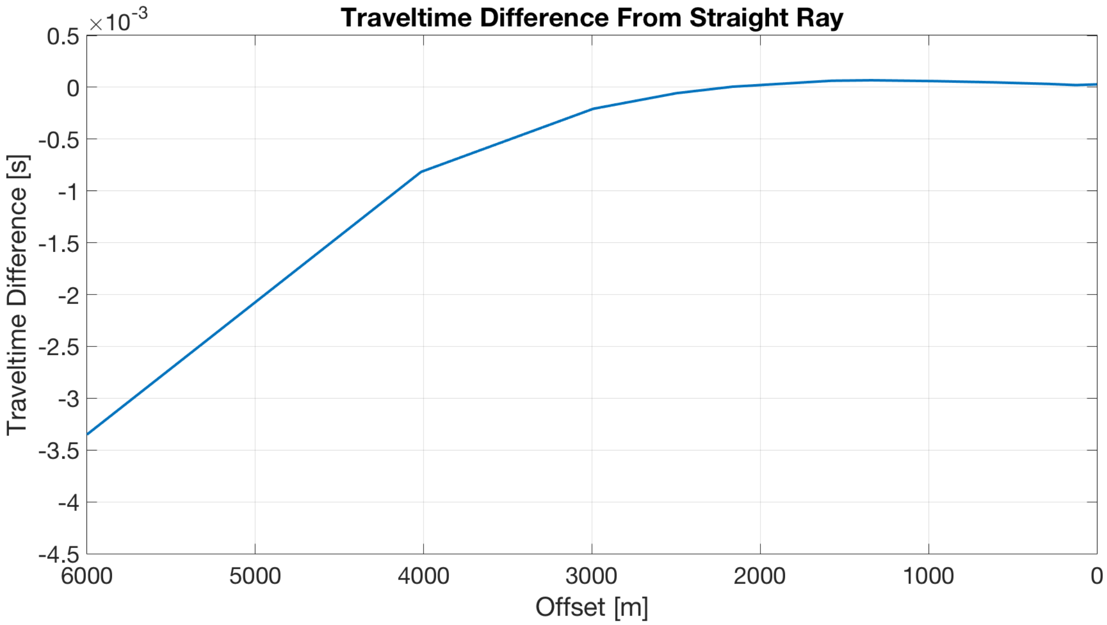

Figure B.24: Traveltime differences between the bent rays in Figure B.22 and the corresponding straight rays with the same start and stop points. The differences are calculated by: (Traveltime Bent Rays) - (Traveltime Straight Rays). Note the increase in difference with offset as the rays get more and more bent.